ADVANCES IN HEAT TRANSFER, VOLUME 30

Multiphase Flow and Heat Transfer in Porous Media

C. Y. WANG

Department of Mechanical Engineering, Pennsylvania State University, University Park, Pennsylvania

P. CHENG

Department of Mechanical Engineering, The Hong Kong University of Science and Technology, Clear Water Bay, Kowloon, Hong Kong

I. Introduction

Problems involving multiphase flow, heat transfer, and multicomponent mass transport in porous media arise in a number of scientific and engineering disciplines. Important technological applications include thermally enhanced oil recovery [1], subsurface contamination and remediation [2], capillary-assisted thermal technologies [3], drying process [4], thermal insulation materials [4a], multiphase trickle bed reactors [5], nuclear reactor safety analysis [6], high-level radioactive waste repositories [7], and geothermal energy exploitation [8].

A number of complex, interacting transport phenomena may take place in a nonisothermal, multiphase system. In general, multiphase flows in porous media are driven by gravitational, capillary, and viscous forces. Gravity causes phase migration in the direction of the gravitational field. A common example is gravity override of steam as commonly encountered in steam injection for enhanced oil recovery and subsurface remediation, where the injected steam tends to rise to the top of a formation thus leading to a premature breakthrough of steam into production wells. The detrimental outcome of steam override is a large reduction in the recovery of oil or contaminant and a significant waste of latent-heat thermal energy.

Another example of the influence of gravity is thermosolutal convection in each fluid phase as a result of density variations due to combined temperature and concentration gradients. Thermosolutal convection directly controls distillation of light components in oil recovery processes, evaporation rates in drying processes, and the gas phase transport of contaminants in the subsurface environment and in remediation processes (e.g., during soil vapor extraction).

Capillary forces play fundamental roles in controlling the phase distribution and hence multiphase flow and transport in heterogeneous porous media. In the context of groundwater contamination, the capillary forces due to interfacial tension are largely responsible for the extent of lateral spreading of a contaminant as it encounters a low-permeability layer. Viscous forces influence relative phase motion: Fluids with lower viscosity tend to migrate more rapidly due to their reduced resistance to flow. When a denser, less viscous fluid displaces another fluid of lower density and higher viscosity, the process is inherently unstable, leading to fingering of phase interfaces [9].

Due to the complicated transport phenomena involved, the multiphase flow and transport in porous media remains poorly understood and analytically intractable. This chapter summarizes the most recent theoretical and experimental work in this field in order to identify current capabilities and thus provide a basis for further developments. Nonisothermal flows with heat transfer are the focus, whereas isothermal multiphase flows in porous media have been extensively discussed in several excellent reviews by Morel-Seytoux [10], Wooding and Morel-Seytoux [9], Adler and Brenner [11], and De Santos *et al.* [12]. Previous major articles and chapters addressing various aspects of multiphase heat transfer in porous media include those by Whitaker [4], Tien and Vafai [13], Vakai and Sözen [13a], Kaviany [14], Dhir [6], and Catton and Chung [15]. The purpose of this chapter is to compile and summarize the many ongoing studies of the fundamental phenomena and new analytical and experimental techniques for *simultaneous* multiphase flows. These are a class of the most difficult problems to deal with, and include, as limiting cases, the situation where one or more phases are immobile. Both pure and multicomponent systems are addressed. Ample references to the original literature are included in this chapter, but no attempt has been made to be complete.

The review is divided into sections devoted to fundamental systems rather than specific applications. Part II outlines several theoretical models currently prevailing in the literature for multiphase flow and heat transfer in porous media. In particular, a multiphase mixture model that we recently developed [16] is elaborated on and compared with the traditional multiphase flow model [17] and unsaturated flow theory [10].

Part III reviews both theoretical and experimental work for single-component two-phase systems with major applications to thermal engineering, while Part IV is devoted to general multiphase, multicomponent systems in connection with a wide variety of engineering applications, such as drying of porous materials, groundwater contamination, and remediation. The last part summarizes the conclusions and indicates areas for future research.

II. Theoretical Considerations

This section surveys and assesses the mathematical models available in the literature to describe multiphase transport phenomena in porous media. The summary includes only the most generic models that can be applied to various situations. The earliest modeling efforts involving multiphase flow in porous media began in the petroleum industry [18]. These models then provided the basis for many of the current multiphase flow and transport models in hydrology [17], chemical engineering [19], and thermal-fluid engineering [14]. The starting points for development of any multiphase model are the principles of mass, momentum, species, and energy conservation. Because multiphase flow in porous media is generally a special subset of multiphase systems, many of the recent advances in multiphase theories have influenced the porous media research. For example, the technique of volume averaging was widely utilized to rigorously derive macroscopic transport equations [20, 21]. Microscopic modeling efforts were made to accurately incorporate microscopic interfacial phenomena [14, 22]. Multiscale modeling approaches were attempted in order to transmit information over various length scales, ranging from microscale, mesoscale, macroscale, and finally to the field scale [23–26].

A. Basic Concepts

To establish a fundamental theoretical framework, basic concepts associated with multiphase transport in porous media are first discussed.

1. *Phase Saturation*

Saturation of a fluid is defined as the volume fraction of the total pore space occupied by that fluid. Saturations vary from zero to unity and the saturations of all phases add up to unity. The saturation geometrically quantifies the phase distribution in a porous medium and thus influences the resistance to the flow of each phase. It is an important parameter on

which many other properties (e.g., capillary pressure and relative permeability) depend.

Direct measurement of phase saturations within a porous medium would normally disturb the sample. Indirect determination of phase saturations is usually made by measuring the change in the sample mass, by measuring the change in attenuation of gamma ray energy [27], and through three-dimensional (3D) imaging technology such as X-ray tomography [28] or magnetic resonance imaging [29]. Because of resolution limitations inherent to these techniques, their utility is restricted to providing saturation information over relatively large areas. Most recently, a photoluminescent volumetric imaging (PVI) technique was developed by Montemagno and Gray [30] to overcome this drawback. With a measurement resolution better than 1 μm, the PVI technique provides a powerful tool to quantify the microscopic distribution of the fluid phases as well as their interfaces within a porous medium. Another recent experimental technique to measure phase saturations is called transmitted light imaging [31]. The technique relies on a uniform, controlled, diffuse light source passing through a translucent sample, and uses a digital imaging system to capture the saturation field. The technique allows for whole-field saturation measurements with high spatial and temporal resolutions. Despite the fact that its utility has been limited to thin slab samples (~ 1 cm) under isothermal flow conditions, this technique appears to hold great promise for adaptation to heat transfer studies under both steady and transient conditions.

2. *Interfacial Tension*

Interfacial tension is referred to as the free surface energy at the interface formed between two immiscible or nearly immiscible fluids. It results from the difference between the mutual attraction of like molecules within each fluid and the attraction of dissimilar molecules across the fluid interface. Interfacial tension is directly responsible for capillary effects. For nonisothermal multicomponent systems, interfacial tension depends strongly on temperature and species concentration.

3. *Capillary Pressure*

If two immiscible fluids are in contact, a curved surface tends to develop at the phase interface. By measuring the pore pressure near the interface in each phase, we find that the pressures are not the same. The difference is the capillary pressure, which is defined as

$$p_{cjk} = p_j - p_k . \tag{1}$$

Capillary pressure is directly proportional to the interfacial tension and inversely proportional to the radius of curvature. The radius curvature, in turn, is dependent on the pore size and the amount of each fluid present, that is, phase saturations. Hence, the capillary pressure can be expressed as a function of the interfacial tensions and phase saturations for multiphase systems. This function is generally multivalued, and exhibits hysteretic behaviors. Figure 1 shows typical capillary pressure curves in a liquid–gas two-phase system, where the liquid is the wetting phase and the gas is the nonwetting fluid. Changes in capillary pressure with saturation depend on whether the medium is undergoing wetting (imbibition) or draining of the wetting fluid. In the drainage process, the capillary pressure increases as the liquid saturation decreases. Eventually, no more liquid phase will be displaced by the gas phase, even with further increases in capillary pressure. This saturation value is known as the residual or irreducible liquid saturation s_{lr}. Conversely, when the imbibition curve reaches zero capillary pressure, some of the gas phase remains in the

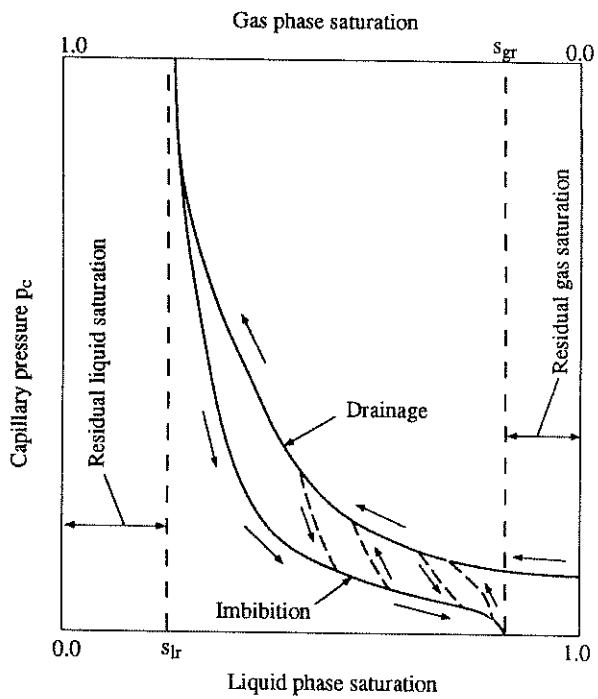

FIG. 1. Capillary pressure curves for liquid–gas two-phase systems. s_{gr}, the residual or irreducible gas saturation; s_{lr}, the residual or irreducible liquid saturation.

porous medium. This saturation is known as the residual or irreducible gas saturation s_{gr}.

An example of the capillary pressure function for an air–water system is given by Udell [32]. Lenhard and Parker [33] evaluated a scaling procedure to derive capillary pressure relations of air–water, air–NAPL and NAPL–water porous media systems (where NAPL stands for nonaqueous phase liquids). Using this procedure, three-phase capillary pressures can also be predicted from two-phase relationships [34].

4. *Relative Permeability*

During simultaneous multiphase flow, the available pore space is shared by multiple fluids. The cross-sectional area of the pore space available for each fluid phase is thus less than the total pore space. This leads to the concept of relative permeability. The relative permeability k_r, is defined as the ratio of the intrinsic permeability for a phase at a given saturation to the total intrinsic permeability of the porous medium. Figure 2(a) schematically shows two-phase relative permeability curves for both wetting and nonwetting fluids, where the irreducible phase saturation denotes the threshold value at which the phase no longer flows. Figure 2(b) is a ternary relative permeability diagram for the NAPL in an air–water–NAPL system [35]. In general, relative permeabilities are assumed to be known functions of the phase saturations, which are determined empirically.

B. Multiphase Flow Model (MFM)

Traditionally, macroscopic problems of multiphase flow and transport in porous media are modeled by a multiphase approach [17, 36], in which various phases are regarded as distinct fluids with individual thermodynamic and transport properties and with different flow velocities. The transport phenomena are mathematically described separately by the basic principles of conservation for each phase and by appropriate interfacial conditions between various phases. The generalized Darcy law is employed to represent momentum conservation in each phase, with the relative permeabilities of each phase introduced to account for a decrease in the effective flow cross section due to the presence of other phases. An important assumption usually made in this model is interfacial thermal and chemical equilibrium between the fluid phases. A brief summary of the multiphase flow formulation for multiphase, multicomponent transport in a porous medium is given below. Note that the following set of macroscopic equations can be derived either heuristically or by the method of volume averaging [20, 21].

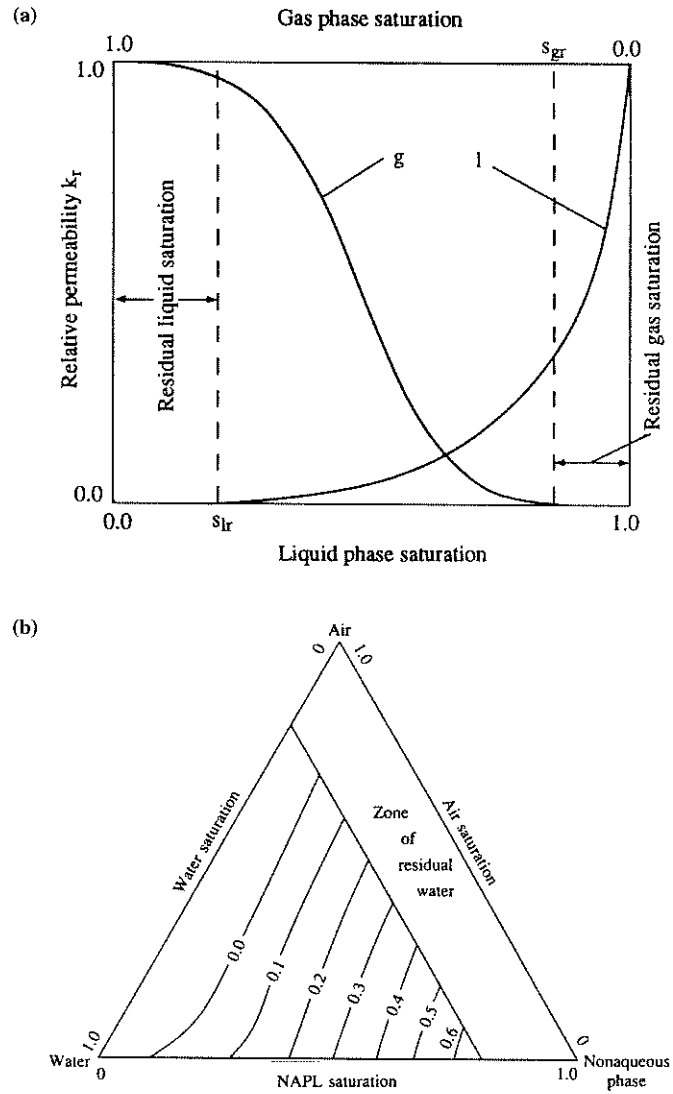

FIG. 2. Two-phase and three-phase relative permeability curves. (a) NAPL, nonaqueous phase liquids. (b) Reprinted with permission by Faust [35]. s_{gr}, the residual or irreducible gas saturation; s_{lr}, the residual or irreducible liquid saturation.

1. *Mass conservation in phase k:*

$$\varepsilon \frac{\partial(\rho_k s_k)}{\partial t} + \nabla \cdot (\rho_k \mathbf{u}_k) = \bar{m}_k, \tag{2}$$

where ε is the porosity of the porous medium, s_k is the phase saturation denoting the volumetric fraction of the void space occupied by phase k, and $\mathbf{u}_k$ is the superficial (or Darcian) velocity vector based on the total cross-sectional area of multiple fluids and porous medium. The term $\bar{m}_k$ represents an interfacial mass transfer rate from all other phases to phase k. In the absence of any external mass source or sink, it follows that

$$\sum_k \bar{m}_k = 0. \tag{3}$$

Equations (2) and (3) assume that the porous medium is not deformable.

2. *Momentum conservation in phase k:*

$$\mathbf{u}_k = -K \frac{k_{rk}}{\mu_k} (\nabla p_k - \rho_k \mathbf{g}), \tag{4}$$

where the presence of the gravitational force has been taken into account. The difference between the pressures for two adjacent phases k and j is described by the capillary pressure defined in Eq. (1). This generalized Darcy's equation is valid if inertia as well as (macroscopic) viscous effects can be neglected.

3. *Mass conservation of species α in phase k:*

$$\frac{\partial}{\partial t}(\varepsilon \rho_k s_k C_k^\alpha) + \nabla \cdot (\rho_k \mathbf{u}_k C_k^\alpha) = -\nabla \cdot \mathbf{j}_k^\alpha + \bar{J}_k^\alpha, \tag{5}$$

where C_k^α is the mass concentration of species α in phase k, and $\mathbf{j}_k^\alpha$ is a diffusive flux of species α in phase k due to molecular diffusion, hydrodynamic dispersion, or both. The latter is usually expressed in Fickian form:

$$\mathbf{j}_k^\alpha = -\varepsilon \rho s_k D_k^\alpha \nabla C_k^\alpha, \tag{6}$$

where D_k^α is a macroscopic second-order tensor and depends on the molecular diffusion coefficient and fluid velocity. Presently, much effort is being expended to model the hydrodynamic dispersion phenomenon (see, e.g., Brenner and Edwards [22]).

The last term in Eq. (5), $\bar{J}_k^\alpha$, denotes the interphase species transfer rate caused by chemical reaction, phase change, or both at the interfaces between phase k and all other phases. Recognizing that the production of species α in phase k must be accompanied by destructions of species α in other phases, it follows that

$$\sum_k \bar{J}_k^\alpha = 0, \tag{7}$$

provided there is no extrinsic species generation due to chemical or biological reactions.

4. *Energy conservation in phase k:*

$$\frac{\partial}{\partial t}(\varepsilon \rho_k s_k h_k) + \nabla \cdot (\rho_k \mathbf{u}_k h_k) = \nabla \cdot (s_k k_k \nabla T) + \bar{q}_k, \tag{8}$$

where local thermal equilibrium among phases has been assumed ($T_k = T$), and k_k and $\bar{q}_k$ represent the effective thermal conductivity of phase k and the interphase heat transfer rate associated with phase k, respectively. Hence,

$$\sum_k \bar{q}_k = \dot{q}, \tag{9}$$

where $\dot{q}$ stands for an external volumetric heat source or sink. The phase enthalpy h_k is related to the common temperature T via

$$h_k = \int_0^T c_k \, dT + h_k^0, \tag{10}$$

where c_k and h_k^0 represent the effective specific heat and the reference enthalpy of phase k, respectively.

The previous basic conservation laws provide a full system of governing equations for the unknown vector velocities $\mathbf{u}_k$, scalar pressures p_k, scalar liquid saturations s_k, mass concentrations C_k^α, and the common temperature T. Due to this large number of primary variables and their highly nonlinear equations, exact solutions to multiphase flow and transport problems are limited to a very small class of problems in one dimension and with many simplifying assumptions [37]. Solving practical problems, which usually involve multidimensional effects, gravity, capillarity, and phase change, requires sophisticated numerical procedures and represents a challenging task [38].

Another fundamental difficulty of MFM in simulating multiphase flow and transport in porous media lies in the presence of moving and irregular phase interfaces separating the single-phase and multiphase subregions that co-exist in a physical system. The locations of these interfaces are not known *a priori* but must be determined by the coupled flows in adjacent regions. A numerical procedure for such a multiregion problem based on MFM needs to explicitly track the moving interfaces, thus calling for complex coordinate mapping or numerical remeshing [39]. Alternatively, in

the water resources literature [40] the procedure of switching the primary variables and governing equations in various regions is usually adopted, which may severely affect numerical stability and convergence speed.

C. Unsaturated Flow Theory (UFT)

In order to alleviate the analytical difficulties associated with the multiphase flow model, an approximate model called the unsaturated flow theory was developed and popularly used by hydrologists [10, 41]. Applications of UFT to condensation heat transfer problems in porous media were also demonstrated [42, 43]. In the following, we briefly derive the well-known Richards equation in UFT to gain insight into the important assumptions made in the theory and thus identify its limitations in certain situations.

Substitution of Eq. (4) into Eq. (2) for a liquid phase (e.g., water in hydrology) yields

$$\varepsilon \frac{\partial(\rho_l s_l)}{\partial t} + \nabla \cdot \left(-K \frac{k_{rl}}{\nu_l} \nabla p_l + K \frac{k_{rl}}{\nu_l} \rho_l \mathbf{g} \right) = \overline{m}_l . \tag{11}$$

This provides a single equation for two unknowns, s_l and p_l. To close the mathematical system, it is traditionally assumed that the gas phase (e.g., air in hydrology) essentially remains at a constant pressure, equal to atmospheric pressure, so that ∇p_l is simple given by

$$\nabla p_l = \nabla p_g - \nabla p_c = \nabla(\rho_g \mathbf{g}) - \frac{dp_c}{ds_l} \nabla s_l . \tag{12}$$

With this identity, Eq. (11) can be rearranged as

$$\varepsilon \frac{\partial(\rho_l s_l)}{\partial t} + \nabla \cdot \left(K \frac{k_{rl}}{\nu_l} \frac{dp_c}{ds_l} \nabla s_l \right) + \nabla \cdot \left[K \frac{k_{rl}}{\nu_l} (\rho_l - \rho_g) \mathbf{g} \right] = \overline{m}_l . \tag{13}$$

Furthermore, a diffusivity is defined as

$$D(s_l) = -K \frac{k_{rl}}{\nu_l} \frac{dp_c}{ds_l} . \tag{14}$$

By its definition, $D(s_l)$ is always positive. Equation (13) then takes the final form of

$$\varepsilon \frac{\partial(\rho_l s_l)}{\partial t} - \nabla \cdot (D \nabla s_l) + \nabla \cdot \left[K \frac{k_{rl}}{\nu_l} (\rho_l - \rho_g) \mathbf{g} \right] = \overline{m}_l . \tag{15}$$

This equation, with the interphase mass transfer $\overline{m}_l$ and the gas phase density neglected, is usually known as the *Richards equation* and can be solved similarly to a diffusion equation.

D. Multiphase Mixture Model (MMM)

Most recently, an alternative approach was developed to the modeling of multiphase flow and multicomponent transport in porous media [16]. In this so-called multiphase mixture model, the multiphase system is viewed as being a chemical mixture. Multiphase flow is then described in terms of a mass-averaged mixture velocity and a diffusive flux, representing the difference between the mixture velocity and an individual phase velocity. Without making any assumptions, a new set of transport equations for the multiphase mixture was derived from the classic multiphase flow model. Moreover, explicit relations describing the relative motions between the multiphase mixture and an individual phase are found that can be used to determine the intrinsic characteristics of the phase dynamics (e.g., the phase velocity fields). An overview of the multiphase mixture model is presented subsequently.

1. *Basic Definitions*

As in a classic multicomponent mixture, all physical properties of the multiphase mixture are consequences of the properties of its constituents; however, their functional forms are not assumed *a priori*, but are derived strictly from the multiphase flow model. The mixture density, velocity, species concentration, enthalpy, and pressure are defined, respectively, as

$$\rho = \sum_k \rho_k s_k , \tag{16}$$

$$\rho \mathbf{u} = \sum_k \rho_k \mathbf{u}_k , \tag{17}$$

$$\rho C^\alpha = \sum_k \rho_k s_k C_k^\alpha , \tag{18}$$

$$\rho h = \sum_k \rho_k s_k h_k , \tag{19}$$

$$p = p_k + \sum_i \int_0^{s_i} Ca_{ik}\, ds_i + \sum_\alpha \int_0^{C^\alpha} Cs_{\alpha k}\, dC^\alpha + \int_0^T Ct_k\, dT , \tag{20}$$

where a quantity without a subscript is reserved for the multiphase mixture, and the subscript k denotes phase k. The symbols are defined in the section on Nomenclature. The superficial velocity of phase k, $\mathbf{u}_k$, is related to its intrinsic velocity by the phase volume fraction, and thus Eq. (17) implies that the mixture velocity is a mass-weighted average of the intrinsic phase velocities.

The definition of the mixture pressure in Eq. (20) is somewhat nonconventional; however, inspection in several limiting cases reveals that the definition is indeed consistent with a mixture theory [16]. As we shall see, the definition given in Eq. (20) greatly simplifies the momentum conservation equation for a bulk mixture. The terms Ca_{ik}, $Cs_{\alpha k}$, and Ct_k in Eq. (20) are called the capillary, solutal-capillary, and thermocapillary factors, respectively, and can be expressed as functions of capillary pressure gradients with respect to saturation, species concentration, and temperature.

In addition, the mixture kinematic viscosity and the mobility of each phase in the multiphase mixture are introduced, respectively, as follows:

$$\nu = \left(\sum_k \frac{k_{rk}}{\nu_k} \right)^{-1}, \tag{21}$$

$$\lambda_k = \frac{k_{rk}}{\nu_k} \nu, \qquad \sum_k \lambda_k = 1. \tag{22}$$

2. *Model Equations*

The multiphase mixture model consists of the governing equations written only in terms of the mixture variables defined previously, which can be summarized as follows [16].

1. *Mass conservation of the multiphase mixture:*

$$\varepsilon \frac{\partial \rho}{\partial t} + \nabla \cdot (\rho \mathbf{u}) = 0. \tag{23}$$

It is clear that this continuity equation is just a duplicate of the corresponding equation for a single-phase mixture flow. Since the mixture density ρ is strongly variable, the multiphase mixture flow should be categorized as highly compressible.

2. *Momentum conservation of the multiphase mixture:*

$$\rho \mathbf{u} = -\frac{K}{\nu}(\nabla p - \gamma_\rho \rho \mathbf{g}), \tag{24}$$

where γ_ρ is called the density correlation factor and is defined as

$$\gamma_\rho = \frac{\sum_k \rho_k \lambda_k}{\sum_k \rho_k s_k}. \tag{25}$$

It should be noted that this correction factor is a sole function of phase saturations, and thus can be regarded as a property of the multiphase mixture. The physical reason that a correction factor appears in the body force for a multiphase mixture is the relative motion between phases, so that the effective mixture density for the gravitational force contains certain dynamic properties of phases (i.e., λ_k and hence ν_k). Only when $\gamma_\rho = 1$, can the body force for the multiphase mixture be represented by the mixture density defined in Eq. (16). This is the case of single-phase multicomponent mixtures.

3. *Diffusive flux.*

As in a traditional mixture theory, we can define a diffusive mass flux of phase k relative to the whole multiphase mixture, such that

$$\mathbf{j}_k = \rho_k \mathbf{u}_k - \lambda_k \rho \mathbf{u}, \qquad \sum_k \mathbf{j}_k = 0, \tag{26}$$

or alternatively,

$$\rho_k \mathbf{u}_k = \mathbf{j}_k + \lambda_k \rho \mathbf{u}. \tag{27}$$

Wang and Cheng [16] found that the diffusive flux can be expressed as

$$\mathbf{j}_k = \sum_i \left[-\rho_k D_{cik} \nabla s_i + \frac{\lambda_k \lambda_i K(\rho_k - \rho_i)}{\nu} \mathbf{g} \right] + \sum_\alpha \left[-\rho_k D_{s\alpha k} \nabla C^\alpha \right] + (-\rho_k D_{tk}) \nabla T, \tag{28}$$

where the capillary diffusion coefficient D_{cik}, the solutal-capillary diffusion coefficient $D_{s\alpha k}$, and the thermocapillary diffusion coefficient D_{tk}, are given by

$$D_{cik} = \frac{K}{\rho_k \nu} \lambda_k \sum_j \lambda_j \left[-\frac{\partial p_{cjk}}{\partial s_i} \right], \tag{29}$$

$$D_{s\alpha k} = \frac{K}{\rho_k \nu} \lambda_k \sum_j \lambda_j \left[-\frac{\partial p_{cjk}}{\partial \sigma_{jk}} \frac{\partial \sigma_{jk}}{\partial C^\alpha} \right], \tag{30}$$

$$D_{tk} = \frac{K}{\rho_k \nu} \lambda_k \sum_j \lambda_j \left[-\frac{\partial p_{cjk}}{\partial \sigma_{jk}} \frac{\partial \sigma_{jk}}{\partial T} \right]. \tag{31}$$

Physically, Eq. (28) implies that the diffusive flux of phase k within the multiphase mixture results from the capillary forces due to saturation gradients, as well as concentration and temperature gradients through their effects on the interfacial tensions. In addition, the second term on the right-hand side of Eq. (28) reflects the gravitational separation due to the difference between phase densities. Note also that the diffusion coefficients defined by Eqs.

(29) to (31) depend only on phase saturations and, hence, are properties of the multiphase mixture.

4. *Conservation of species α in the multiphase mixture:*

$$\varepsilon \frac{\partial}{\partial t}(\rho C^\alpha) + \nabla \cdot (\gamma_\alpha \rho \mathbf{u} C^\alpha) = \nabla \cdot [\varepsilon \rho D \nabla C^\alpha] + \nabla \cdot \left\{ \varepsilon \sum_k [\rho_k s_k D_k^\alpha (\nabla C_k^\alpha - \nabla C^\alpha)] \right\} - \nabla \cdot \left(\sum_k C_k^\alpha \mathbf{j}_k \right), \quad (32)$$

where the correction factor for species advection γ_α, is defined as

$$\gamma_\alpha = \frac{\rho \sum_k \lambda_k C_k^\alpha}{\sum_k \rho_k s_k C_k^\alpha}, \quad (33)$$

and the effective diffusion coefficient for the multiphase mixture is defined as

$$\rho D = \sum_k \rho_k s_k D_k^\alpha. \quad (34)$$

The second term on the left-hand side of Eq. (32) indicates that species α is advected, on the mixture level, by a modified velocity field $\gamma_\alpha \mathbf{u}$ rather than by the original mixture velocity field. This peculiar feature resembles that related to the gravitational term in the momentum equation, Eq. (24). The first two terms on the right-hand side of Eq. (32) combine to represent the net Fickian diffusion fluxes within various phases, whereas the last term on the right-hand side represents the diffusive flux across phases. Also, note that the second term on the right-hand side of Eq. (32) vanishes in single-phase regions or when the phase compositions C_k^α are identical in all phases.

It is worth mentioning that the mixture concentration C^α in a multiphase region essentially corresponds to the phase saturation s_k through Eq. (18) because the phase compositions C_k^α are given by the corresponding phase diagram under the assumption of local chemical equilibrium. Therefore, solving C^α from Eq. (32) determines all the phase saturations that, in turn, are used to calculate the mixture properties.

5. *Energy conservation for the multiphase mixture:*

$$\frac{\partial}{\partial t}[(1-\varepsilon)\rho_s h_s + \varepsilon \rho h] + \nabla \cdot (\gamma_h \rho \mathbf{u} h) = \nabla \cdot (k_{\text{eff}} \nabla T) + \nabla \cdot \left[\sum_k (h_k \mathbf{j}_k) \right] + \dot{q}, \quad (35)$$

where local thermal equilibrium among contiguous phases is invoked, and the correction factor for energy advection γ_h, is defined as

$$\gamma_h = \frac{\rho \sum_k \gamma_k h_k}{\sum_k \rho_k s_k h_k}. \quad (36)$$

The second term on the right-hand side of Eq. (35) describes the energy flux due to relative phase motions, including both sensible and latent heat transport.

3. *Model Summary*

Equations (23), (24), (32), and (35) represent a full system of governing equations for four mixture variables, that is, mixture velocity $\mathbf{u}$, mixture pressure p, mixture concentration C^α, and the mixture temperature T. As can be seen, striking similarities exist between the MMM equations and those in the single-phase transport theory; the two sets differ only in that property coefficients are variable and additional source terms appear (in the mixture species and energy equations) in MMM. The similarities are physically conceivable because on the mixture level, a multiphase system is not much different from a single-phase fluid. The variable properties contained in the model equations precisely reflect the physics that multiphase flow problems are inherently nonlinear. The source terms arise from the interfacial mass and heat transfer processes occurring internally within the multiphase mixture. For single-phase flows, these source terms vanish and the variable properties reduce identically to those corresponding to the single-phase transport theory.

Recognizing the similar structure of MMM to the single-phase transport theory, it is clear that the new model equations for multiphase flows are amenable to well-established single-phase computational fluid dynamics (CFD) algorithms. The solution sequence may be as follows:

1. From the transport equations for the multiphase mixture, the mixture pressure, velocity, concentration, and temperature fields are determined.

2. From the mixture pressure, concentration and temperature at a nodal point, the thermodynamic state of this cell is identified (see Wang and Cheng [16] for details).
3. Phase concentrations are then calculated from equilibrium phase diagrams, and the phase saturations are determined from the mixture concentration solved from the species transport equation.
4. Effective thermophysical properties of the multiphase mixture are then evaluated with the knowledge of phase saturations, and finally these properties are substituted back into the transport equations for updating.

The entire procedure is repeated iteratively until convergence is achieved. Successful calculations for several practical problems have been made [44–48].

In closing, it should be mentioned that the mixture pressure, Eq. (20), introduced to facilitate the development of MMM is similar to the "global pressure" previously proposed by Chavent [49] and Yortsos [50] in an attempt to obtain a simplified mathematical system describing immiscible displacement in porous media. The slight difference lies only in the fact that the present definition is generally applicable to multiphase flows with and without phase change, whereas the previous concept is limited to immiscible flow without phase change and interphase mass transfer. Nonetheless, the fundamental novelty of the present formulation is Eqs. (26) to (28), which allow the calculation of individual phase velocities, thus maintaining the mathematical equivalence between MFM and MMM. The key equation, Eq. (28), was first derived by Wang and Beckermann [51] for two-phase systems and was extended by Wang and Cheng [16] for general multiphase systems.

E. Comparisons of Various Models

Compared with the traditional MFM, MMM offers the following advantages:

1. It strongly resembles the single-phase transport theory, thus facilitating both theoretical and numerical analyses.
2. It requires much fewer nonlinear and coupled differential equations to be solved. For example, for a three-phase isothermal flow, the MFM requires a total of 12 primary variables: 2 phase saturations, 9 velocity components for 3 phases in 3 dimensions and any one phase pressure. In contrast, MMM contains only 6 primary variables: 2 mixture concentrations (or equivalently 2 phase saturations), 3 mixture velocity components, and the mixture pressure. This unique feature renders MMM particularly suitable for numerical simulations with even moderate computer resources.
3. It is a mixture formulation, thus eliminating the need to handle phase appearance or disappearance and to track interfaces separating single-phase from multiphase regions. The mixture variables are always present.
4. Most importantly, MMM provides the same predictive capabilities as does the conventional MFM. With the aid of Eqs. (27) and (28), the flow characteristics of individual phases can be obtained readily after the flow problem of the bulk mixture has been solved. Thus the detailed flow aspects of each phase are not smeared out in MMM. Similarly, the phase pressures p_k can be obtained from Eq. (20) after the mixture pressure, temperature, concentration, and phase saturation fields are determined. Moreover, these types of calculations, if needed, can be done in a postprocessing manner. This is why the model is called the *multiphase mixture model*, rather than simply a mixture model, implying that, in the latter, the intrinsic multiphase characteristics usually are lost.

In essence, MMM is a mathematically equivalent but reformulated version of MFM (i.e., without making any additional approximations). The model reduction was achieved by replacing some differential equations contained in MFM by the corresponding algebraic equations in MMM.

To compare MMM with UFT, it is instructive to substitute Eq. (27) for the liquid mass flux $\rho_l \mathbf{u}_l$ into the mass conservation equation for the liquid phase, Eq. (2). This results in

$$\varepsilon \frac{\partial(\rho_l s_l)}{\partial t} + \nabla \cdot (\rho \mathbf{u} \lambda_l) = -\nabla \cdot \mathbf{j}_l + \overline{m}_l, \tag{37}$$

where the diffusive mass flux $\mathbf{j}_l$ can be simplified, in the case of isothermal two-phase flow, to

$$\mathbf{j}_l = -\rho_l D_c \nabla s_l + \frac{\lambda_l \lambda_g K(\rho_l - \rho_g)}{\nu} \mathbf{g}. \tag{38}$$

Substitution of Eq. (38) into Eq. (37) yields

$$\varepsilon \frac{\partial(\rho_l s_l)}{\partial t} + \nabla \cdot (\rho \mathbf{u} \lambda_l) = \nabla \cdot (\rho_l D_c \nabla s_l) - \nabla \cdot \left(\frac{\lambda_l \lambda_g K(\rho_l - \rho_g)}{\nu} \mathbf{g} \right) + \overline{m}_l. \tag{39}$$

This equation can be referred to as the generalized Richards equation because it identically reduces to the Richards equation in the limit of the

constant gas phase pressure or, equivalently, zero gas viscosity. In this case, it can be easily shown from Eqs. (21), (22), and (29) that

$$\lambda_l \to 0, \quad \lambda_g \to 1, \quad \frac{\lambda_l}{\nu} \to \frac{k_{rl}}{\nu_l}, \quad \rho_l D_c \to D(s_l). \tag{40}$$

Substitution of these asymptotes into Eq. (39) recovers the Richards equation of UFT. Thus it is clear that the Richards approximation elegantly eliminates the advective term in Eq. (39), thereby resulting in a single equation having a diffusion nature for the liquid saturation. Whereas this yields great simplifications, the applicability of UFT to general multiphase flow problems is severely limited because the gas phase motion cannot be determined.

The Richards equation can also be derived from Eq. (39) using the limit $\nu_1 \to \infty$. Collectively, it can be concluded that UFT holds true in the limit of the viscosity ratio ν_l/ν_g approaching infinity. A numerical experiment for a boundary layer–type two-phase flow indicated that this condition corresponds to such a high threshold value that practically no fluid pair could possibly match it (see Part III, Section D.4 for further discussion).

In the absence of the Richards approximation, Eq. (39) contains both diffusion and advective terms, where the mixture velocity field must be determined from the continuity and momentum equations given by Eqs. (23) and (24). In view of the fact that UFT introduces approximations that are difficult to justify and ascertain in general situations, the exact nature of Eq. (39) may open new prospects for a more accurate understanding of multiphase flow through porous media.

F. Nonequilibrium Effects

In all the foregoing mathematical models, interfacial thermal and chemical equilibrium is assumed implicitly. In most circumstances, the assumption is adequate; however, in other practical applications, interfacial heat and mass transfer may become rate-limited.

Interfacial thermal equilibrium has been under investigation for many years. Whitaker [52] attempted to define the domain of validity of local thermal equilibrium by an order of magnitude estimate. Using the method of volume averaging, Kaviany [14] extensively examined local thermal nonequilibrium effects and developed a two-equation model for the averaged temperatures in each phase. The form of the two-equation model in the case of pure diffusion was further explored by Quintard and Whitaker [53].

Interfacial chemical nonequilibrium recently received intensive attention in the field of groundwater contamination and remediation. Results of a series of laboratory-scale experiments [54] demonstrated several potential limitations of the local chemical equilibrium assumption. In particular, the dissolution of contaminants into the aqueous phase was found to be rate-limited by interfacial mass transfer under low NAPL saturation or high aqueous phase flow conditions typically encountered during pump-and-treat remediation [55–57]. In relation to the popular soil vapor extraction technique for subsurface remediation, the interfacial mass transfer between NAPL and air has been determined experimentally [58]. Most recently, Quintard and Whitaker [59] derived a macroscopic multiphase flow model that rigorously accounts for interfacial mass transfer between phases.

Whereas the multiphase flow model can easily be extended to include interfacial nonequilibrium effects, it is of interest to explore the potential of MMM in describing nonequilibrium processes. It should be noted that MMM is not inherently an equilibrium model; in fact, the model has accounted for dynamic nonequilibrium because it allows for different phase velocities, as discussed in the preceding section. Similarly, the assumptions of interfacial thermal and chemical equilibrium can be relaxed. Under such circumstances, the model differential equations summarized previously remain valid, whereas only the supplementary relationships for determining phase saturations, phase temperatures, and compositions need to be modified. In the absence of thermal and chemical equilibrium, the bulk phase temperature and concentration depart from their interfacial values (as determined from equilibrium phase diagrams), with the magnitudes of departures measured by the local heat and mass transfer coefficients.

G. Non-Darcian Effects

Non-Darcian effects, such as inertial, boundary, and dispersion effects, have been widely investigated for single-phase flows [14, 60]. Forchheimer and Brinkman's extensions of Darcy's law have been well established, and species and thermal dispersion coefficients have been determined by, for example, Koch and Brady [61] and Hsu and Cheng [62]. This situation clearly is different for multiphase flows. While the non-Darcian effects may be equally important in certain multiphase problems (i.e., the boundary effect in two-phase condensing flow and the inertia effect in trickle beds), it remains largely unknown how to incorporate these effects into a multiphase flow model. This point of view is particularly evident in the recent monograph by Kaviany [14]. Much more fundamental research on

multiphase flows in porous media is needed before these non-Darcian effects can be rigorously incorporated. Preliminary attempts at modeling the inertia effect in the literature are reviewed subsequently to show how little is known in this area.

Based on visual observations of co-current and countercurrent flow of air and water in beds composed of large-diameter particles ($d_p \geq 3$ mm), Tung and Dhir [63] derived a hydrodynamic model that includes the generalized Darcy term, quadratic inertia term, and an interfacial drag. The expressions for relative permeability and interfacial drag were also developed. The model prediction for one-dimensional (1D) co-current and countercurrent two-phase flows was found to be in good agreement with the experimental measurements.

Using the volume averaging theory, Grosser *et al.* [64] and Dankworth *et al.* [65] derived a set of macroscopic equations for gas–liquid flow in trickled beds, which is in a form similar to that of two-phase flow without porous media. The momentum equation for each phase contains an interfacial drag accounting for the total forces exerted on that phase by the other fluid phases as well as by the stationary solid matrix. A constitutive relationship for the interfacial drag was developed, which resembles the single-phase Ergun correlation.

A semiheuristic approach to incorporate the effect of inertia was proposed by Kaviany [14]. The two-phase momentum equations were obtained simply by multiplying the relative permeability to the Darcy term and another "microscopic inertia coefficient" to the inertia term of the single-phase Forchheimer equation. Both coefficients are assumed to depend only on the saturation and must be determined empirically. Although the previous models possess appropriate asymptotic behaviors in the limits of zero and unity liquid saturation, they apparently lack in taking into account fundamental pore-level fluid mechanics. The models with and without interfacial drag are inconsistent. The modeling burden is simply shifted to the calibration of the empirical coefficients introduced. It is expected that the general framework established in MMM may provide a novel approach (from the perspective of the multiphase mixture) to the fundamental modeling of non-Darcian effects in multiphase flows.

III. Two-Phase, Single-Component Systems

Two-phase flow and heat transfer in porous media saturated with pure fluids has historically received intensive attention due to its enormous technological importance and academic interest. Three distinct regions

may appear in a two-phase, single-component system with heat transfer:

1. A single-phase vapor region where the voids are filled with superheated vapor
2. A nearly isothermal two-phase zone in which vapor and liquid co-exist at equilibrium
3. A single-phase liquid region with the pore spaces occupied by the subcooled liquid.

Such a thermodynamic state is conveniently sketched in Fig. 3 with a 1D geometry. Evaporation occurs at the lower boundary of the two-phase zone with bottom heating or volumetrically with internal heating, while vapor condensation takes place at the upper boundary of the two-phase zone in the case of top cooling. The countercurrent liquid–vapor percolation provides a net upward heat flow.

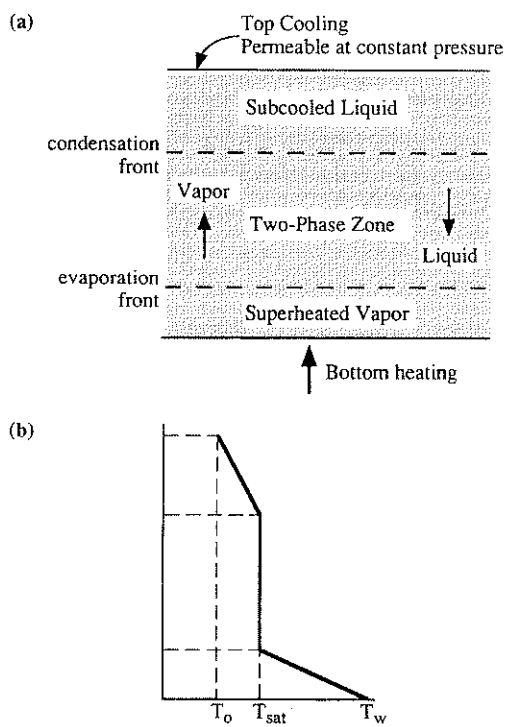

FIG. 3. Schematic illustration of (a) boiling in a one-dimensional porous medium, and (b) the temperature profile.

Using Kelvin and Clapeyron equations, Udell [32] determined the saturated temperature in the two-phase zone as follows:

$$T = \frac{T_0\left[1 + \dfrac{p_c}{h_{fg}\rho_l}\right]}{1 - \dfrac{RT_0}{h_{fg}} \ln \dfrac{p_v}{p_0}}, \tag{41}$$

where T_0 and p_0 are the reference temperature and its saturation pressure at which the capillary pressure is zero and hence the vapor pressure p_v becomes equal to the reference p_0. The subscripts l and v in Eq. (41) and throughout this section denote liquid and vapor phases, respectively. The temperature in the two-phase zone is practically constant under most conditions except for geothermal situations, where the relevant length scale is on the order of kilometers and hence the pressure variation is substantial. Satik *et al.* [66] found that the importance of heat conduction due to the temperature difference in the two-phase zone is quantified by a single dimensionless group

$$\frac{Kh_{fg}^2 M_w p_0 \rho_v}{\mu_v k_{\text{eff}} RT_0^2},$$

where M_w is the molecular weight of the fluid component and R is the universal gas constant. Typically, this dimensionless parameter is large and heat conduction is negligible.

A. One-Dimensional Situations

One-dimensional two-phase flow in porous media is of theoretical interest for understanding the transport processes occurring in a variety of engineering systems such as heat pipes, geothermal reservoirs, and nuclear debris beds. This is also the only class of two-phase flow problems that admit exact solutions. Extensive research has been carried out in both steady-state and transient cases.

In a 1D situation, the continuity and liquid mass conservation equations given by Eqs. (23) and (39) are simplified, respectively, to

$$\varepsilon \frac{\partial \rho}{\partial t} + \frac{\partial(\rho u)}{\partial x} = 0, \tag{42}$$

$$\varepsilon \frac{\partial(\rho_l s_l)}{\partial t} + \frac{\partial(\rho u \lambda_l)}{\partial x} = \frac{\partial}{\partial x}\left(\rho_l D_c \frac{\partial s_l}{\partial x}\right) - \frac{\partial}{\partial x}\left(\frac{\lambda_l \lambda_v K(\rho_l - \rho_v) g_x}{\nu}\right) + \overline{m}_l, \tag{43}$$

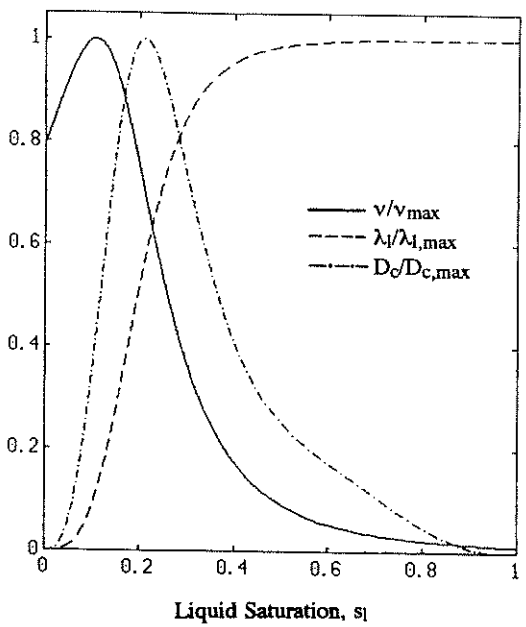

FIG. 4. Variations of two-phase mixture properties with respect to the liquid saturation.

where g_x denotes the x-component of the gravity vector. It is evident that the mixture velocity u and liquid saturation s_l represent the only primary variables for 1D problems, while other variables such as phase velocities and pressures can be algebraically determined, from the various relations given in Part II, Section D, after Eqs. (42) and (43) are solved. Hence, Eqs. (42) and (43) form a theoretical basis for 1D two-phase flow in porous media with and without phase change. Furthermore, the familiar form of this equation set can shed considerable light on finding possible analytical solutions, as will be discussed later. Note that the two-phase property coefficients in Eqs. (42) and (43) are strongly dependent on the liquid saturation s_l. Figure 4 displays typical variations of these coefficients, which include the mixture viscosity ν, relative mobility λ_l (and $\lambda_v = 1 - \lambda_l$), and capillary diffusion coefficient D_c.

1. *Steady Two-Phase Flows*

Various analytical solutions exist for steady, 1D two-phase flow problems, as summarized by Lipinski [67] with application to the nuclear reactor safety analysis. These flows are induced by bottom heating, volumetric heating, or both. Under the steady-state conditions, the continuity

equation, Eq. (42), requires that

$$\rho u = \dot{m}_w, \tag{44}$$

where $\dot{m}_w$ denotes a constant mass flux across the two-phase zone. If the two-phase zone is bounded by an impermeable wall, that is, $\dot{m}_w = 0$, Eq. (44) leads to a uniformly zero mixture velocity within the two-phase zone. Assuming an isothermal two-phase zone, the interphase mass transfer rate $\overline{m}_l$ is equal to $-\dot{q}/h_{fg}$. Integration of Eq. (43) subject to appropriate boundary conditions yields

$$\rho_l D_c(s) \frac{\partial s_l}{\partial x} - \frac{\lambda_l \lambda_v K(\rho_l - \rho_v) g_x}{\nu} = \frac{1}{h_{fg}} \left(q_w + \int \dot{q}\, dx \right) + \dot{m}_w (\lambda_l - \lambda_{l,w}). \tag{45}$$

This equation is a key theoretical tool for studying steady 1D two-phase flows in porous media with phase change. Physically Eq. (45) implies that the two-phase flow may be driven by capillary forces, gravitational forces, or both. The last term on the right-hand side would vanish if either boundary of the two-phase zone were impermeable. As will be shown subsequently, exploration of various limiting cases of Eq. (45) allows for an overview of previous theoretical studies on steady 1D two-phase flow and heat transfer in porous media.

In the absence of capillary forces (i.e., in the gravity-driven case), Eq. (45) reduces to an algebraic equation, implying that a two-phase zone of constant liquid saturation results. Moreover, there are two solutions for a given heat flow rate, one corresponding to low liquid saturation (vapor dominated, VD) and the other corresponding to high liquid saturation (liquid dominated, LD). The multiple solutions arise from the fact that the product of the two relative mobilities varies nonmonotonically with the liquid saturation, as clearly shown in Fig. 4. Figure 5 illustrates the multiple possible solutions to a two-phase problem with bottom heating for a special choice of relative permeabilities given by Bau and Torrance [68]: $k_{rl} = s_l$ and $k_{rv} = (1 - s_l)$. The selection of a particular solution in reality depends on the past history of the system. For instance, in the case of boiling (bottom heating), it is the LD branch that is followed, while in condensation of a superheated vapor (top cooling), it is the VD branch that is selected [66]. Using a singular perturbation method, McGuinness [69] rigorously analyzed Eq. (45), and proposed a concept called *capillary boundary layer* to explain the selection process of either LD or VD solution.

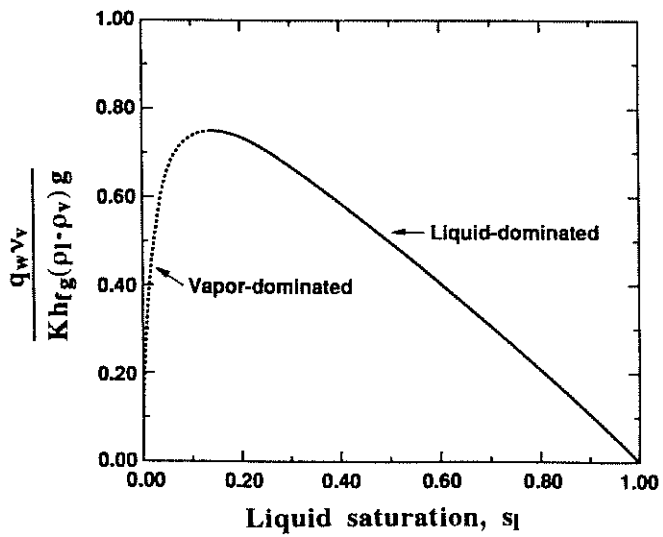

FIG. 5. Multiple solutions for the two-phase zone with negligible capillarity [68].

Figure 5 also showed that there exists a maximum heat flux at a particular value of the liquid saturation. The limit represents the peak heat flux that can be transported through a two-phase zone by the counter-current percolation mechanism. When the applied heat flux exceeds this maximum, the two-phase zone must disappear and be replaced by a superheated vapor layer. Thus the limit is also called the dryout heat flux, which can be predicted from Eq. (45) with the capillary term neglected; that is,

$$\frac{q_{\text{dry}} \nu_v}{Kh_{fg}(\rho_l - \rho_v)(-g_x)} = \max_{s_l} \left\{ \frac{\lambda_l \lambda_v \nu_v}{\nu} \right\} = \max_{s_l} \left\{ \frac{k_{rl} k_{rv}}{k_{rl} + (\nu_l / \nu_v) k_{rv}} \right\}. \tag{46}$$

Apparently the dryout limit is dependent on the particular form of relative permeabilities. Including the capillary effect, Udell [32] solved Eq. (45) numerically to obtain the dryout heat flux for the cases of bottom and top heating, and compared them with his experiments for a steam–water system.

The effects of medium heterogeneity on two-phase flow and resultant dryout with bottom heating were explored by Chuah and Carey [70], Wang *et al.* [71], and Stubos *et al.* [72], among others. Chuah and Carey studied two-phase flow in a continuously variable porosity layer, but did not

consider the associated dryout limit. Wang *et al.* [71] numerically investigated two-phase flow and dryout in a composite porous layer heated from below. The porous bed consisted of two homogeneous sublayers of different particle diameter. A saturation jump was found to exist at the interface between the two sublayers due to the capillary force resulting from medium heterogeneity. The jump may have a positive or negative effect on the dryout heat flux, depending on whether a high-permeability sublayer overlies one of low permeability, or vice versa. In the enhanced case, the optimal thickness of the high-permeability sublayer was determined to be around 60% of the total bed height for the maximum dryout heat flux. Stubos *et al.* [72] further explored the effects of medium heterogeneity on vapor–liquid counterflow in porous heat pipes, and showed that the capillary heterogeneity is analogous to an external body force, aiding or opposing the gravity roles in the operation of heat pipes.

Dryout limits in volumetrically heated beds were compiled by Lipinski [67] for various particle diameters using water and Freon as the working fluids, as shown in Fig. 6. In Fig. 6 the available experimental data are also compared with the theoretical predictions based on a generalized version of Eq. (45) with the inertia effect included. Reasonable agreement is found, indicating that a hydrodynamic model is adequate to describe the dryout phenomenon of boiling in a wide variety of porous beds. Dhir [6] summarized experimental data on the effects of system variables on the dryout heat flux, such as vapor channeling, liquid subcooling, and forced flow through porous beds. The effect of liquid throughflow is readily seen from Eq. (45) where $\lambda_{l,w}$ is equal to unity due to liquid feeding from the bottom. It then can be deduced that the dryout heat flux increases with the liquid throughflow rate $\dot{m}_w$. Furthermore, Eq. (45) reveals that the lower bound of the dryout heat flux with the feeding of liquid from below should be given by $\dot{m}_w h_{fg}$, which is exactly the amount of energy needed to convert all of the incoming liquid into vapor. The dryout heat flux data obtained by Tsai and Catton [73] for the case of forced flow, as displayed in Fig. 7, indeed shows such an asymptotic behavior. The difference between the measured data and their lower bound represents the contribution of the countercurrent two-phase flow driven by gravity. As the throughflow rate increases, the gravity-induced contribution diminishes and a co-current flow pattern begins to prevail in most of the porous bed.

In geothermal systems the capillary term is often negligible because of the system's large length scales, and typically there is neither a surface nor volumetric heat source to sustain the two-phase zone in the shallow subsurface. Instead, the decrease in pressure, which occurs on approaching the ground surface, acts as a volumetric heat source to generate the vapor. For a given pressure variation with depth, an equivalent heat generation

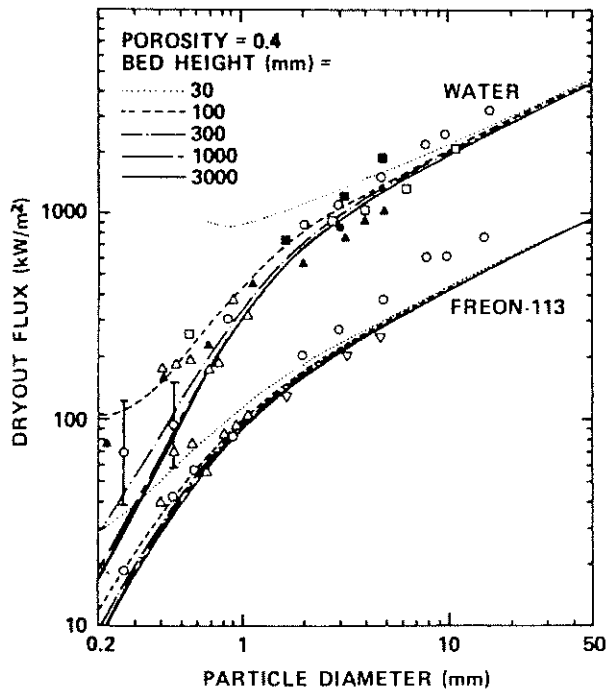

FIG. 6. Experimental (symbols) and theoretical (lines) dryout heat fluxes in a variety of packed beds saturated with water and Freon-113 [67].

rate can be calculated from the energy equation, requiring the temperature to follow on the Clapeyron curve for saturated temperature and pressure. Sheu *et al.* [74] investigated a system with steady flow through the two-phase zone (i.e., $\dot{m}_w \neq 0$) in order to model geothermal reservoirs above cooling igneous intrusions. Pressure release boiling results in a two-phase zone of variable saturation as the heat generation rate varies with location. Within this zone, steam percolates upward relative to water and condenses at the upper boundary due to conductive heat loss to the cold ground surface. Numerical results were compared with temperature and pressure logs from drill holes in the thermal systems of Steamboat Springs, Nevada, and Yellowstone National Park, Wyoming. Schubert and Straus [75] analytically explored the case without vertical throughflow (i.e., $\dot{m}_w = 0$).

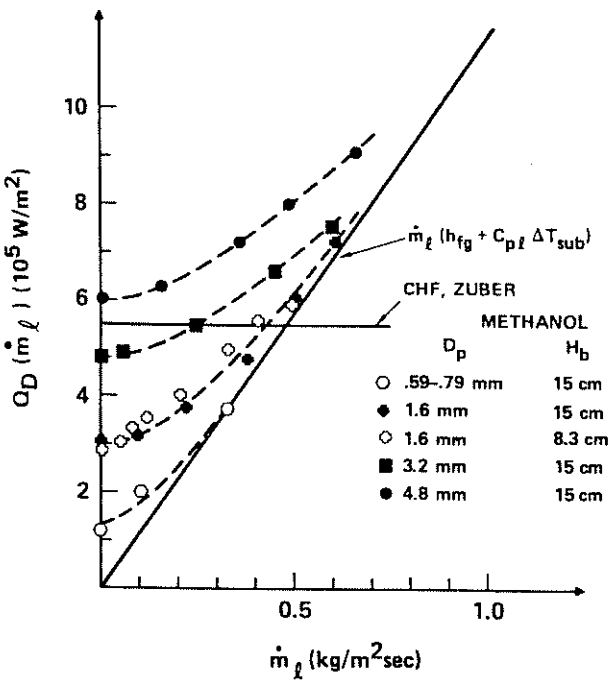

FIG. 7. Dryout heat flux data for a methanol-saturated bed with liquid feeding from below. The solid line denotes an asymptotic limit. CHF, the critical heat flux of pool boiling [73].

2. *Transient Two-Phase Flows*

Exact similarity solutions can be obtained for transient two-phase flows in porous media under certain types of initial and boundary conditions [37, 77]. To show this, we neglect the interphase mass transfer rate and the gravity effect in Eq. (43). The governing equations then become

$$\varepsilon \frac{\partial \rho}{\partial t} + \frac{\partial (\rho u)}{\partial x} = 0,$$
$$\varepsilon \frac{\partial (\rho_l s_l)}{\partial t} + \frac{(\rho u \lambda_l)}{\partial x} = \frac{\partial}{\partial x}\left(\rho_l D_c \frac{\partial s_l}{\partial x}\right). \tag{47}$$

If the boundary condition for the velocity u varies inversely proportional to the square root of time, a similarity variable, $\eta = x/\sqrt{t}$, reduces Eq. (47) to a set of ordinary differential equations. This change of variables, known as the Boltzmann transformation in heat conduction, is the tool employed by Morrison [76], Doughty and Pruess [77], and McWhorster and Sunada [37] to arrive at an exact solution for various two-phase flows with and without phase change.

Morrison [76] numerically analyzed a transient condensing two-phase flow by applying the foregoing similarity transformation, and showed that a discontinuity in saturation occurs at the condensation front. This shocklike behavior is attributed to the neglect of capillary effects from Eq. (47). Similarity solutions were also obtained by Nilson and Romero [78] for the propagation of a condensation front into an initially dry porous matrix that received an inflow of saturated vapor. Once again, the capillarity was ignored, thus leading to the hyperbolic equations, as can be seen from Eq. (47). Later, their analysis was extended to various types of initial and boundary conditions [79]. In addition, an experimental study [80] was performed to validate the theoretical prediction of temperature and pressure profiles. Recently, Tsurata *et al.* [81] experimentally and analytically investigated condensing flow through an initially subcooled porous medium. It is worth mentioning that all these studies on phase change flows failed to recognize that the same similarity transformation exists even with the inclusion of capillarity. Therefore, it is of interest for future research to explore the effects of capillarity in altering the shocklike behavior of transient two-phase flows in porous media.

Doughty and Pruess [77] studied the thermal and geological behavior resulting from the emplacement of a heat source, such as a high-level nuclear waste package, into a geological medium. The above-mentioned similarity transformation was applied to obtain a coupled set of ordinary differential equation that were solved numerically in the cylindrical coordinates.

McWhorster and Sunada [37] considered two-phase flow in porous media without phase change for hydrological applications. Using the foregoing similarity transformation, they developed the first "exact" solution in the presence of capillarity. A limit of their solution in the absence of capillarity is the well-known Buckley-Leverett case. McWhorster and Sunada's solutions is now widely used as a benchmark for validation and testing of complex 2D and 3D numerical codes for multiphase flow and transport in porous media [82].

Transient two-phase flow inside a heat pipe wick was investigated experimentally and analytically by Ambrose *et al.* [83], who reported the transient liquid saturation profiles along a heat pipe as a function of heat input to the evaporator section. Measurements of the liquid saturation distribution was made by X-ray radiography. The theoretical equation derived to predict the liquid distribution inside the porous wick strongly resembled the UFT version of Eq. (43). The predicted and measured liquid saturation distributions were compared favorably.

B. Internal Boiling and Natural Convection

The two-phase Bérnard-like problem in a horizontal porous layer with bottom or internal heating has been the subject of recent research. Both experimental [68, 84] and theoretical [39, 44, 45, 86, 87] investigations were performed. An important finding from the latest numerical study by Wang *et al.* [45] is that various transient effects may well exist in this inherently nonlinear two-phase system. Separate discussion for each heating mode follows.

1. *Bottom Heating*

Single-phase natural convection inside a horizontal liquid-saturated porous layer heated from below has been a classic topic and has received extensive research attention for many years [60]. When the bottom heat flux exceeds a critical value, boiling or evaporation starts adjacent to the heated surface, and the thermodynamic state of the system then consists of a two-phase zone underneath a subcooled liquid region, as schematically shown in Fig. 8. Convection in the upper liquid region affects the boiling behavior in the underlying two-phase zone, and the two-phase flow, in turn, influences natural convection in the overlying liquid region. It is this interactive nature that rendered this fundamentally interesting problem unsolved until the 1990s.

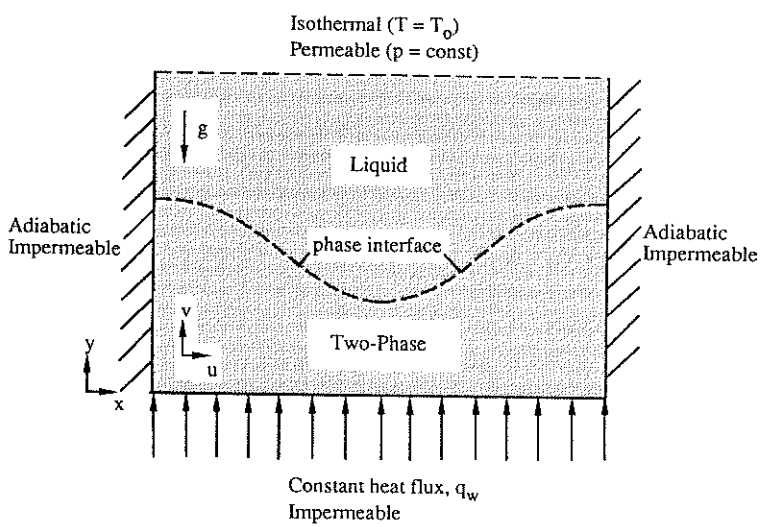

FIG. 8. Schematic illustration of boiling and two-phase flow in a horizontal porous cavity heated from below.

a. Linear Stability Analysis When the liquid region overlies the two-phase zone, there are two instability mechanisms: buoyancy and gravitational instabilities. The gravitational instability of vapor–liquid counterflow, referred to as the heavier full-liquid region overlying the lighter two-phase zone, differs from the classic Rayleigh-Taylor instability of superposed fluids in that the phase interface is permeable and thus allows both mass and heat transfer across it. Schubert and Straus [88] performed a linear stability analysis and found that such systems are stable, provided the permeability is sufficiently small. The stability is maintained because when liquid penetrates the phase interface, that interface is distorted along the Clapeyron curve, thereby creating a pressure gradient that acts to restore the system to equilibrium.

The onset of 2D polyhedral-shaped convection in the configuration of Fig. 8 was studied by Ramesh and Torrance [86] using a linear stability analysis. Their analysis revealed that the governing parameters include the Rayleigh numbers Ra and $\mathrm{Ra}_{2\phi}$ for the liquid and two-phase regions as well as the dimensionless bottom heat flux Q_w. These parameters are defined, respectively, as

$$\mathrm{Ra} = \frac{\beta_l (T_{\mathrm{sat}} - T_0) K L_h g}{\nu_l \alpha_l}, \qquad \mathrm{Ra}_{2\phi} = \frac{(1 - \rho_v/\rho_l) K L_h g}{\nu_l \alpha_l},$$

$$Q_w = \frac{q_w L_h}{k_{\mathrm{eff}} (T_{\mathrm{sat}} - T_0)}. \tag{48}$$

The two Rayleigh numbers are related through a density ratio; that is,

$$\frac{\mathrm{Ra}}{\mathrm{Ra}_{2\phi}} = \frac{\beta_l (T_{\mathrm{sat}} - T_0)}{1 - \rho_v/\rho_l} = \frac{\rho_l \beta_l (T_{\mathrm{sat}} - T_0)}{\rho_l - \rho_v}, \tag{49}$$

where the numerator is simply the maximum density variation in the liquid region and the denominator is the density difference between the phases in the two-phase zone. If the boundary temperature T_0 is fixed, the two Rayleigh numbers are not independent.

For liquid-dominated systems, Ramesh and Torrance [86] obtained a comprehensive map of conductive and convective solutions in the Ra–Q_w parameter space, as shown in Fig. 9. Four distinct regions can be identified from this stability map:

1. Conductive liquid layer
2. Convective liquid layer
3. Conductive liquid layer above a two-phase zone
4. Convective liquid layer above a two-phase zone.

The onset of boiling is indicated by curve ABE in Fig. 9. For Q_w values above this curve, boiling occurs with a liquid layer overlying a two-phase

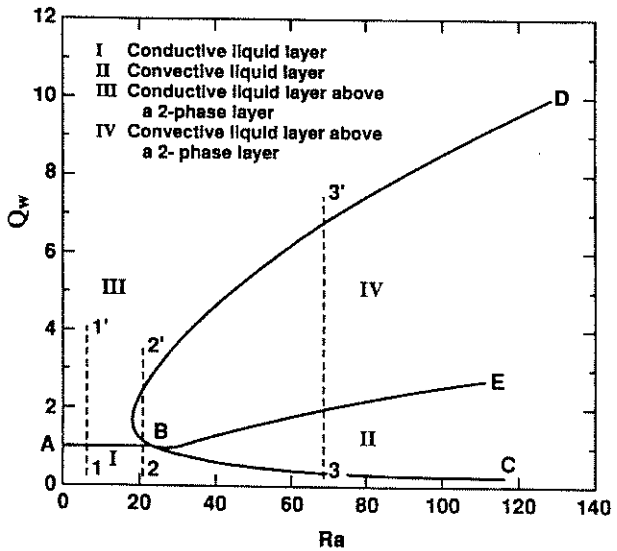

FIG. 9. Map of conductive and convective solutions for liquid-dominated two-phase systems [86]. Q_w, dimensionless heat flux; Ra, Rayleigh number.

zone. For Q_w values below ABE, boiling does not occur. The onset of convection in the liquid is denoted by curve CBD. Convection occurs only to the right of the curve. Curve CBD thus defines the critical Rayleigh number Ra_{cr} as a function of Q_w for a wave number fixed at π.

The map in Fig. 9 is extremely useful for interpreting various boiling experiments. Consider a series of experiments conducted by varying the bottom heat flux and with constant fluid and matrix properties. At low Ra (as indicated by line 1–1′) the liquid region is conductive before and after the onset of boiling. This is consistent with the experiments of Bau and Torrance [68] for low permeability beds ($K = 11 \times 10^{-12}$ m^2). At higher Ra (as indicated by line 2–2′), the liquid region is conductive before the onset of boiling, but becomes convective almost immediately when boiling starts, which is in agreement with the observations of Sondergeld and Turcotte [84] ($K = 70 \times 10^{-12}$ m^2). For large Ra (as denoted by line 3–3′) the liquid region becomes convective before the onset of boiling and stays convective after the onset of boiling, which coincides with the experiments of Bau and Torrance [85] on high permeability beds ($K = 1600 \times 10^{-12}$ m^2). The latter study also showed that at high heat fluxes the liquid region reverts back to a conductive state, which is again predicted by Fig. 9.

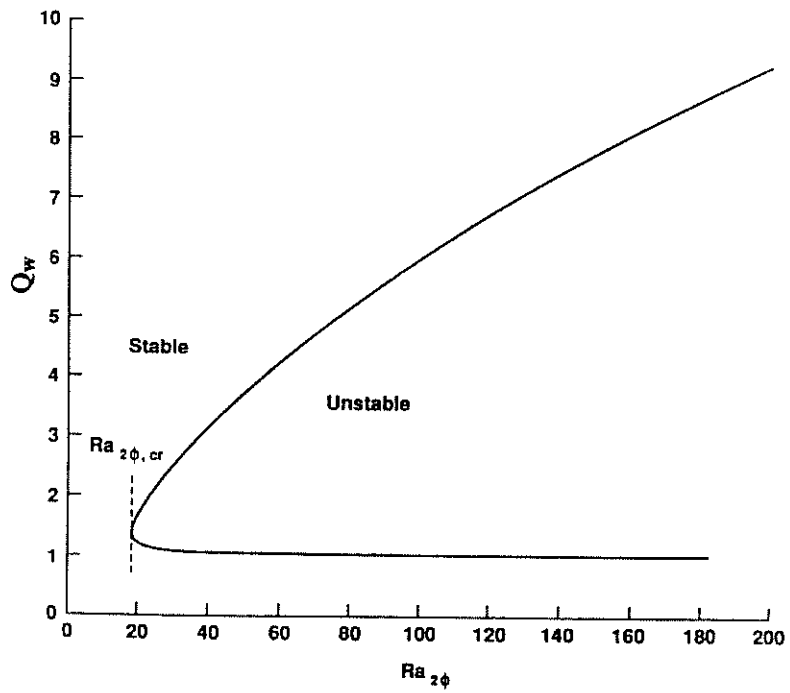

FIG. 10. Stability curves for vapor-dominated two-phase systems with Ra = 0 [86]. Q_w, dimensionless heat flux; Ra, Rayleigh number.

For vapor-dominated systems, the density difference between the liquid and two-phase regions becomes significant, and thus gravitational instability is expected to dominate over buoyancy instability. Neglecting the buoyancy effects (i.e., Ra = 0), Ramesh and Torrance [86] obtained the stability diagram shown in Fig. 10 for vapor-dominated systems. The diagram was obtained for water as the working fluid and for a top surface temperature of 30°C. For the wave number of π, the minimum value of $\mathrm{Ra}_{2\phi}$ for the onset convection was found to be 18.95, occurring at $Q_w = 1.4$.

b. Experimental Observations Observations of boiling in porous materials have been made in several studies. Sondergeld and Turcotte [84] carried out an experimental investigation in a horizontal porous cavity heated from below and cooled from the top. The experimental setup was designed to model a geological thermal reservoir on a laboratory scale. The two-dimensional (2D) porous layer was composed of spherical glass

media ($K = 7.04 \times 10^{-11}$ m^2, $d_p = 0.53$ mm, and $\varepsilon = 0.347$). The rate of heat input was varied over a range of $1.8 < Q_w < 26.0$, where Q_w is the dimensionless bottom heat flux defined in Eq. (48). The case of $Q_w = 1$ corresponds to pure heat conduction occurring inside the bed at the onset of boiling. Sondergeld and Turcotte [84] observed that as Q_w was increased to greater than unity, a single-phase polyhedral-shaped convection flow pattern with central downwelling and peripheral upwelling began to appear. Further increases in Q_w resulted in the appearance of a two-phase zone, and the buoyancy-driven convection cell remained similar to the single-phase case except for penetration into the two-phase zone. The two-phase layer was stable up to the point where $Q_w = 18$, after which a superheated vapor zone eventually appeared.

A similar system, but of cylindrical geometry, was studied by Bau and Torrance [68]. This bed consisted of closely packed glass beads with heating from the base and cooling from the top ($K = 8.5 \times 10^{-12}$ m^2, $d_p = 0.11$ mm, and $\varepsilon = 0.37$). One-dimensional boiling was observed, with the two-phase zone uniformly expanding as the bottom heat flux increases. When the height of the two-phase zone reached about 70% to 80% of the total bed height, the temperature field in the overlying liquid region became time-periodic.

In another study by Bau and Torrance [85], a bed of Ottawa sand was used ($K = 1.4 \times 10^{-9}$ m^2, $d_p = 1.06$ mm, and $\varepsilon = 0.42$). Steady single-phase convection was reported in the system up to a dimensionless heat flux of around $Q_w = 4$. For higher Q_w, boiling occurred and the system consisted of both liquid and two-phase regions. At much higher Q_w values, the cellular convection flow disappeared, and a horizontal liquid layer was then observed to overlie the two-phase zone.

An extensive series of boiling experiments in a rectangular porous bed, again heated from below and with an isothermal top condition, was undertaken by Tewari [89] for five different media permeabilities (5.0×10^{-11} m^2 $< K < 2600 \times 10^{-11}$ m^2, 0.11 mm $< d_p <$ 1.54 mm, and $\varepsilon =$ 0.41). He found that by increasing the dimensionless heat flux Q_w, the flow structure generally evolved in the following sequence:

1. Quiescent conduction
2. Single-phase convective flow across the entire bed
3. Two-phase convective flow either across both liquid and two-phase regions or isolated within the individual regions
4. Stratification of the two regions with heat transfer by conduction in the liquid region and by countercurrent liquid–vapor percolation in the two-phase zone.

In addition, Tewari [89] observed bubble formation and migration in the most permeable bed, suggesting that channeling usually occurs in coarse porous media, accompanying the non-Darcian effects discussed in Part II, Section G.

c. Numerical Analysis Using the Multiphase Flow Model (MFM) Finite-amplitude solutions of two-phase boiling convection were attempted by Ramesh and Torrance [39] using the multiphase flow model (MFM). A numerical algorithm was developed to solve the equations in the liquid and two-phase regions separately as well as to track the phase interface using the Landau coordinate transformation. Convergence and accuracy considerations of the algorithm were discussed and solutions presented for only one case based on coarse grids. Qualitative agreement between the numerical prediction and previous experimental work involving cavity boiling was noted. A major drawback of this algorithm (which is inherent in MFM) was its intensive computer time, that is, obtaining an accurate solution on a sufficiently fine grid would require substantial computational efforts. In a subsequent study [87] the algorithm was employed to perform a parametric study for various values of the liquid Rayleigh number Ra and the dimensionless bottom heat flux Q_w. Three solution regimes were found:

1. Conduction-dominated at low Ra
2. Convection-dominated at intermediate Ra
3. Oscillatory convection at high Ra.

Oscillatory convection appeared to be triggered by asymmetric disturbances in the system.

d. Numerical Analysis Using the Multiphase Mixture Model (MMM) Based on the two-phase version [51] of MMM, direct simulations of the nonlinear, 2D problem were carried out by Wang *et al.* [44]. This steady-state study successfully captured four flow patterns observed in previous experiments:

1. Conductive liquid layer before and after the onset of boiling in low-permeability media [68]
2. Conductive liquid layer before the onset of boiling but convective liquid layer after the onset of boiling for intermediate permeabilities [84]
3. Convective liquid layer before and after the onset of boiling for high permeabilities [85]
4. Convective liquid layer at low heat fluxes, but conductive liquid layer at high heat fluxes in the presence of boiling [85].

Selected results are presented below to further illustrate the intricate interplay between natural convection in the upper liquid region and boiling flow in the two-phase zone.

As observed by Sondergeld and Turcotte [84], thermal convection does not occur in porous media of intermediate permeabilities in the absence of boiling, but starts with the onset of boiling. Furthermore, a visualization study by the same authors [90] revealed distinct cellular convection patterns that involved both the overlying liquid layer and the underlying two-phase zone. These experimental runs were numerically simulated by Wang *et al.* [44]. The numerical results for a representative case are displayed in Fig. 11, which includes the isotherms, iso-liquid saturation lines, streamlines, and phase velocity distributions. This case corresponds to a dimensionless bottom heat flux, Q_w, of 4.0 and a Rayleigh number, Ra, of 60, which translate to a permeability of 7.0×10^{-11} m^2 as in the experiments by Sondergeld and Turcotte [84]. The isotherms denote lines of constant $\theta = (T - T_0)/(T_{sat} - T_0)$, with the top boundary and the

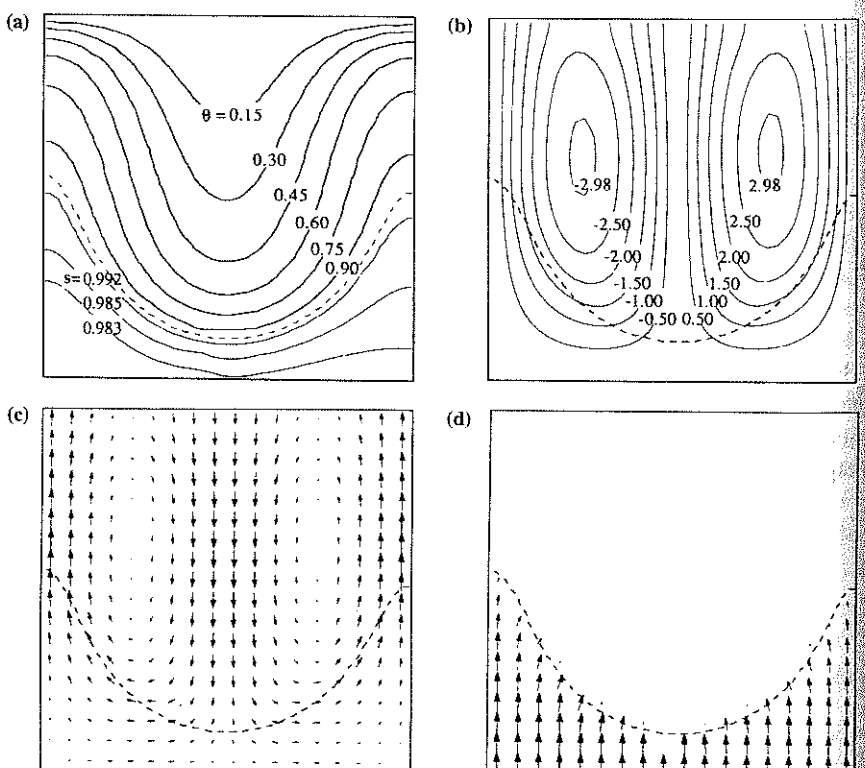

FIG. 11. Numerical results for Ra = 60 and $Q_w = 4$: (a) composite plots of isotherms and iso-liquid saturation lines; (b) streamlines for the two-phase mixture; (c) liquid velocity; and (d) vapor velocity. The dashed line denotes the phase interface between the subcooled liquid and two-phase regions. Q_w, dimensionless heat flux; Ra, Rayleigh number.

phase interface represented by $\theta = 0$ and 1, respectively. The iso-liquid saturation lines, however, denote absolute values. The steamlines are based on the dimensionless mixture velocity (which is the liquid velocity in the liquid region), and the liquid and vapor velocity vector plots correspond to $\mathbf{u}_l$ and $\bar{\rho}\mathbf{u}_v$, respectively (where $\bar{\rho}$ is the density ratio of vapor to liquid). It can be seen from Fig. 11(a) that thermal convection is so strong that the phase interface (represented by a dashed line) is highly distorted. There are two convective cells present in the liquid region with the steamlines penetrating into the two-phase zone (Fig. 11(b)). Whereas the liquid phase has considerable lateral motion (Fig. 11(c)), the vapor flows primarily vertically upward (Fig. 11(d)). These simulation results are in excellent agreement with the experimental observations by Sondergeld and Turcotte [84, 90]. The fact that the formation of a two-phase zone can drive thermal convection can be understood by recalling that the two-phase Rayleigh number $\mathrm{Ra}_{2\phi}$ is substantially higher than the critical single-phase Rayleigh number Ra. While such a steady-state investigation supported the available experiments, the fundamental process of boiling inducing natural convection can only be revealed through a fully transient analysis, as discussed below.

Another simulation was conducted by Wang *et al.* [44] for a relatively high permeability ($K = 10^{-10}$ m^2) for comparison with the experiments by Bau and Torrance [85]. In this case, the Rayleigh number (Ra = 85) was larger than the critical value for the onset of single-phase natural convection, so that steady cellular convection prevails before the onset of boiling. This is shown by the temperature and streamline contours depicted in Figs. 12(a) and 12(b) for $Q_w = 2.0$. The dashed line at the very left and right corners adjacent to the bottom heated surface suggests that this case is

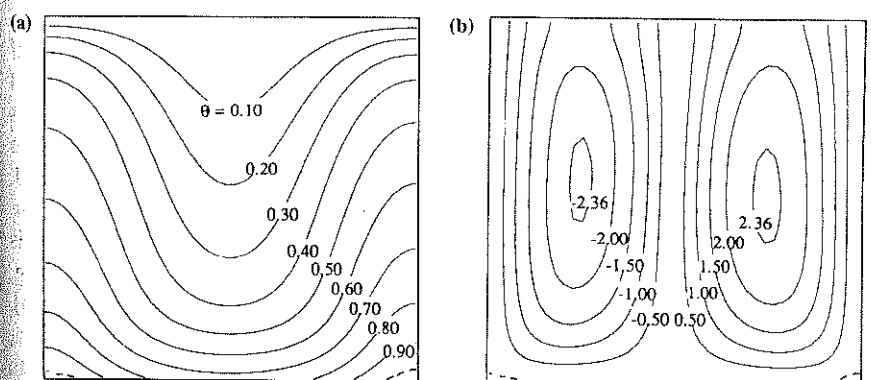

FIG. 12. Numerical results for Ra = 85 and $Q_w = 2$: (a) isotherms and (b) streamlines [44]. Q_w, dimensionless heat flux; Ra, Rayleigh number.

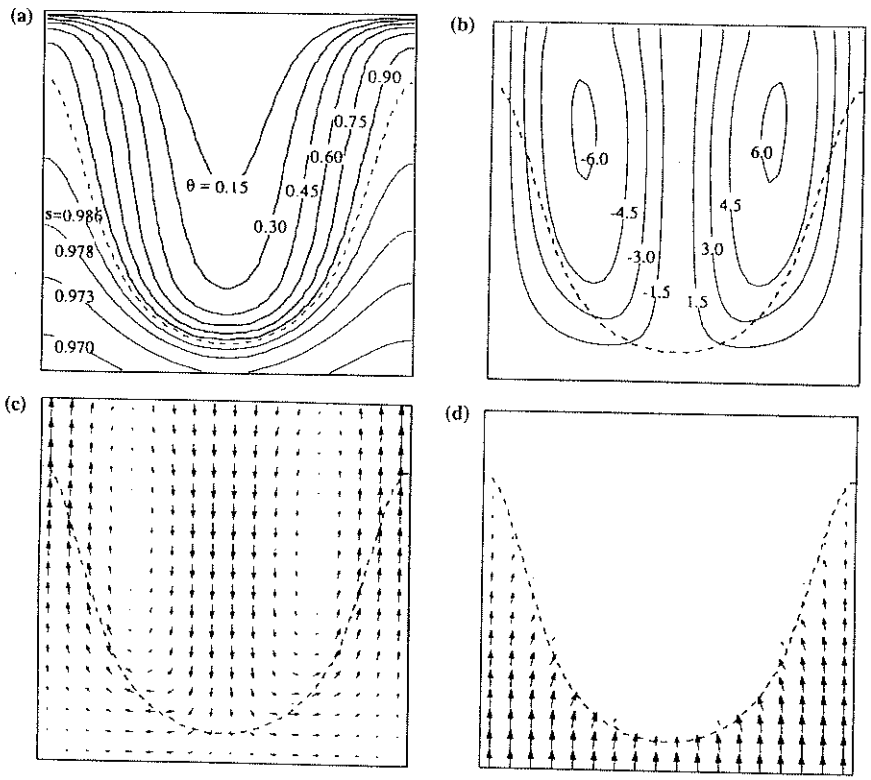

FIG. 13. Numerical results for Ra = 85 and Q_w = 10 [44]. See Fig. 11 for (a) to (d). Q_w, dimensionless heat flux; Ra, Rayleigh number.

marginal to the onset of boiling. After Q_w was raised to 5.0, a two-phase region started to develop at the bottom and thermal convection persisted. When Q_w was further increased, the two-phase zone occupied almost half of the porous bed, and the interaction between boiling and natural convection became more pronounced (see Fig. 13). However, when Q_w was finally raised to 15.0, convection in the liquid region disappeared and the phase interface became horizontally flat [44]. The high heat flux, instead, was acquired by conduction through a thin liquid layer. Clearly these results for high permeability porous media showed that the liquid layer is convective before the onset of boiling and stays convective after boiling, which is consistent with the experiments of Bau and Torrance [85]. Furthermore, it was confirmed that at large bottom heat fluxes (e.g., $q_w = 7$ kW/m^2 in the experiments), the overlying liquid region reverts back to a conductive heat transfer mode, as observed by Bau and Torrance [85].

Quantitative comparison was also attempted in Wang *et al.* [44]. Figure 14 displays the predicted and measured [84] vapor volume fractions in the test cell as a function of the bottom heat flux Q_w. The solid line represents the 2D simulation results, and the dashed line corresponds to a 1D semi-analytical solution that is applicable only to cases where the overlying liquid layer is conduction-controlled and the two-phase zone is dominated by two-phase countercurrent percolation [44]. The squares represent the data points measured by Sondergeld and Turcotte [84]. It can be seen that at low and intermediate bottom heat fluxes, the 2D numerical model predicts the experimental data reasonably well, whereas the 1D analytical model leads to considerable overpredictions. Beyond a certain value of the bottom heat flux, the 2D results merge into the 1D solution curve. This is because, at high heat fluxes, the liquid region shrinks and reverts to the conduction regime, and the flow inside the two-phase zone becomes a 1D flow, as discussed earlier. It is noteworthy that the experimental data of vapor fraction deviates from the prediction at high heat fluxes, likely due to fluidization of the solid matrix under violent boiling that created additional void spaces through which the vapor could escape [84]. However, the experiments performed by Bau and Torrance [85] do confirm the

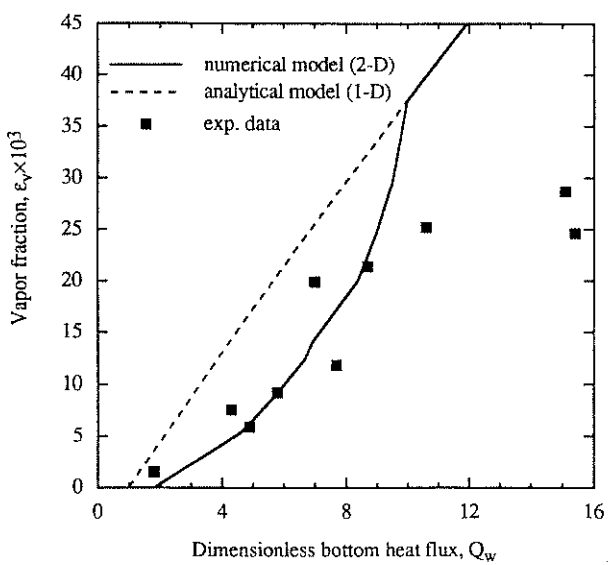

FIG. 14. Comparison of the measured and predicted vapor volume fractions in a two-phase porous layer heated from below [44]. Q_w, dimensionless heat flux; 2D, two-dimensional; 1D, one-dimensional.

transition of the flow from a 2D to a 1D mode at high fluxes. More experiments are needed to thoroughly resolve this issue.

It is also of interest to compare the numerical results of Wang *et al.* [44] with the linear stability results of Ramesh and Torrance [86], since MMM is mathematically exactly equivalent to MFM. We now return to Fig. 12, which shows that the onset of boiling takes place at a dimensionless bottom heat, Q_w, of approximately 2.0 in a porous layer with Ra $\approx$ 85. This finding validates the boiling onset curve labeled BE in the stability map shown in Fig. 9. In addition, the transition from a convective to a conductive overlying liquid layer was numerically predicted to occur at a heat flux between 10 and 15. However, the convection onset curve labeled BD in Fig. 9 indicates $Q_w \approx 7.5$ for the transition. This quantitative discrepancy was found to be related to a hysteresis effect present in the system under consideration. By performing a transient analysis, Wang *et al.* [45] showed that the transition from a convective to a conductive overlying liquid layer can occur over a wide range of bottom heat fluxes; that is, $8.9 \leq Q_w \leq 17.5$, depending on whether the applied heat flux is decreasing or increasing. The slight difference between the linear stability result and the numerically predicted minimum heat flux (i.e., $Q_w = 8.9$) for the transition is possibly due to the fact that the numerical analysis included the capillary effect, which was neglected in the linear stability analysis.

In order to understand the dynamic evolution of a two-phase boiling system and, hence, the underlying physical mechanisms leading to different flow patterns under various conditions, a transient analysis was performed by Wang *et al.* [45] using a fully implicit method. Based on a 42 × 42 grid, a typical simulation for this transient problem required a CPU (central processing unit) time of about 30 min on a Hewlett Packard (Colorado Springs, CO) 715/75 workstation. Such a CPU time is comparable to those reported in the literature for transient single-phase flows with heat transfer and similar complexity. Selected transient results are shown in Fig. 15 for a system with the following parameters: $L_w = L_h = 0.2$ m, $K = 7 \times 10^{-11}$ m^2, $\varepsilon = 0.35$, $T_0 = 293$ K and $q_w = 1020$ W/m^2 (which corresponds to $Q_w = 3.0$ and Ra = 60). This case is chosen to show the transition of the conductive liquid layer before boiling to the convection mode after boiling.

As can be seen from Fig. 15(a), boiling occurs at $t = 3.2 \times 10^4$ sec, and the two-phase region occupies the lower third of the cavity. The phase interface still remains horizontal. The liquid velocity plot shows that the liquid in the two-phase zone moves downward to replenish the bottom boiling surface. The liquid in the upper liquid region, however, is displaced upward out of the top permeable boundary because of the expansion of

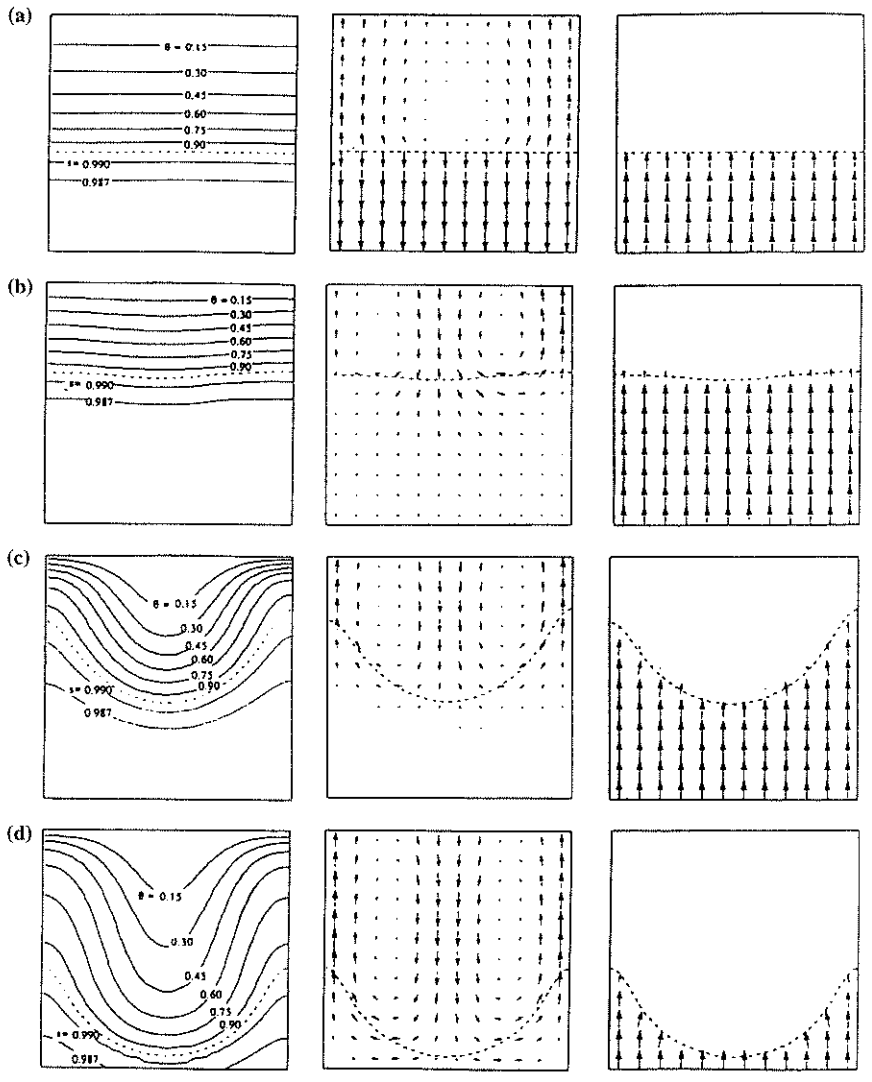

FIG. 15. Numerical results of transient boiling and natural convection in a porous cavity, including isotherms (dimensionless values), iso-liquid saturation lines, liquid and vapor velocities for $Q_w = 3.0$ and Ra = 60 [45]. The vapor velocity is normalized by the density ratio ρ_v/ρ_l. (a) $t = 3.5 \times 10^4$ sec, $|\mathbf{u}_l|_{max} = 4.57 \times 10^{-7}$ m/sec, $|\mathbf{u}_v|_{max} = 4.54 \times 10^{-7}$ m/sec. (b) $t = 5.2 \times 10^4$ sec, $|\mathbf{u}_l|_{max} = 2.23 \times 10^{-6}$ m/sec, $|\mathbf{u}_v|_{max} = 4.60 \times 10^{-7}$ m/sec. (c) $t = 6.2 \times 10^4$ sec, $|\mathbf{u}_l|_{max} = 2.32 \times 10^{-5}$ m/sec. $|\mathbf{u}_v|_{max} = 4.61 \times 10^{-7}$ m/sec. (d) $t = 8.0 \times 10^4$ sec, $|\mathbf{u}_l|_{max} = 1.78 \times 10^{-5}$ m/sec, $|\mathbf{u}_v|_{max} = 4.62 \times 10^{-7}$ m/sec. Q_w, dimensionless heat flux; Ra, Rayleigh number.

the two-phase zone. In Fig. 15(a), the velocity field in the liquid layer has been magnified by a factor of 25 for clarity. Figure 15(a) shows that the vapor generated on the bottom rises up to the phase-change interface, where it condenses. At $t = 5.2 \times 10^4$ sec, the two-phase zone has further expanded, and the system evolves into a state such that small disturbances can be amplified and 2D convection is imminent. This can be seen from the slightly distorted phase change interface shown in Fig. 15(b). The velocity fields of the two phases retain the same features as in Fig. 15(a), except that the liquid velocity in the upper region is no longer magnified.

At $t = 6.2 \times 10^4$ sec, as shown in Fig. 15(c), convection in the liquid region has fully developed. The condensation heat transfer at the phase interface is thus enhanced so that the two-phase region shrinks. The liquid velocity plot reveals two convection cells that are slightly asymmetric and able to penetrate into the lower two-phase zone. At $t = 8 \times 10^4$ sec, as shown in Fig. 15(d), the system acquires a steady state, and the two convection cells become symmetric.

2. *Internal Heating*

Multidimensional phase-change flow in porous media with volumetric heating also has been studied extensively, particularly with application to nuclear reactor safety assessment [91–93]. Experimental results of boiling in a 2D internally heated porous bed were reported by Hardee and Nilson [91] for water–glass and water–silica sand media. Akin to the case of bottom heating, the two-phase flow structure was observed to consist of a subcooled liquid region overlying a two-phase zone. The liquid region was found to decrease in size with an increase in the heat generation rate. A summary of the experimental data of Hardee and Nilson for $\dot{Q}$ versus Ra is shown in Fig. 16, where the dimensionless volumetric heat generation rate and the Rayleigh number are defined, respectively, as

$$\dot{Q} = \frac{\dot{q}L_h^2}{2k_{\text{eff}}(T_w - T_0)}, \qquad \text{Ra} = \frac{g_{\beta l} L_h K \left(\dfrac{\dot{q}L_h^2}{2k_{\text{eff}}} \right)}{\nu_l \alpha_l}. \tag{50}$$

In the single-phase regime, $\dot{Q}$ is identical to the Nusselt number; hence $\dot{Q}$ is unity for conduction, and there exists a single curve between $\dot{Q}$ and Ra for single-phase convection. These features are clearly shown in Fig. 16. The single-phase convection curve is in agreement with the following theoretical correlation:

$$\dot{Q} = \left(\frac{1}{32} \text{Ra} \right)^{1/2}. \tag{51}$$

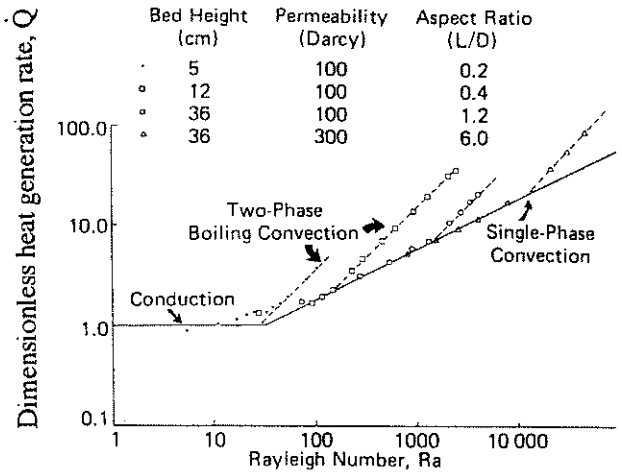

FIG. 16. Summary of conduction, convection, and boiling heat transfer data in porous media with internal heating [91].

Figure 16 or Eq. (51) indicates that the transition from conduction to convection occurs at $\text{Ra}_{cr} = 32$. The family of dotted lines in Fig. 16, which branch from the conduction–convection curve, represents the boiling regimes. In these regimes, the bottom wall temperature T_w remains constant at the saturation temperature, so that $\dot{Q}$ is linearly dependent on Ra. The Rayleigh numbers at the onset of boiling depend on the characteristics of a porous bed and are not universal.

Various attempts have been made to obtain numerical solutions of multidimensional phase-change flows after the onset of boiling. Tsai and Catton [73] used the finite difference method to simulate two-phase flow and dryout in volumetrically heated particles surrounded by nonheated gas particles. Unfortunately, the numerical scheme was not robust and stable, and the calculations had to be terminated prior to dryout. There was, however, a fair agreement between the numerical prediction and experimental data. Later, Tung and Dhir [92] used a finite-element scheme to analyze the same problem, as examined by Tsai and Catton [73]. The mechanistically derived relative permeabilities, as described in Part II, Section G, were used in their numerical model, and the interfacial drag between liquid and vapor phases was also incorporated.

Post-dryout heat transfer in a porous bed is of practical significance because excessive heat can still be removed effectively as long as the maximum temperature of the bed is kept below a critical value, such as the melting point of the bed. These problems are characterized by the simultaneous presence of all three regions: subcooled liquid, two-phase, and

superheated vapor. Neglecting the full-liquid region, Chung and Catton [93] first tackled such a multiple-region problem by coupling the transport equations in the two-phase zone with the energy equation in the superheated vapor region, taking thermal radiation into account. They reported that their solution scheme suffered from a very narrow choice of grid distribution and iteration parameters for convergence. Their results were found to be in fairly good agreement with corresponding experimental data.

Studies of transient two-phase flow and heat transfer in porous media with internal heating are rather scarce. The work of Stubos and Buchlin [94] is an exception. Within the same context of nuclear reactor debris beds, this study differs from all others in that the generalized Darcy law was used (i.e., the model is only applicable to beds of small particles) and the time response of the bed to applied power transients was modeled. The model was claimed to be multidimensional; however, only 1D results were presented and compared with the data from the Sandia National Laboratories (Albuquerque, New Mexico) and European in-pile tests. In one recent study, Stubos *et al.* [95] proposed a micro-macroscopic modeling approach in which the structural and transport properties of the porous medium, such as porosity and effective thermal conductivity, were calculated by a microscopic discrete method, such as the 3D off-lattice algorithm, whereas the transport behavior was computed from a macroscopic, continuum model (i.e., MFM). Although at first sight it appeared sophisticated, a closer examination revealed that the approach of Stubos *et al.* [95] is essentially a two-step decoupled calculation without accounting for dynamic interactions between different length scales. A tight coupling between microscopic interfacial phenomena and macroscopic transport was not established, and thus the effects of phase dynamics on the pore-level would not be captured by such an approach.

C. Internal Boiling and Forced Convection

We now consider liquid forced flow through a partially heated porous formation. When the heat input increases, boiling occurs adjacent to the heated surface and the thermodynamic state of the system then consists of a liquid region and a developing two-phase zone. If the heat flux is sufficiently large, a superheated vapor region may also appear. In these problems the resulting two-phase flow patterns are not only determined by the buoyancy forces along the gravitational direction, but also are affected by the pressure difference in the main flow direction. Such complicated two-phase flow and heat transfer processes are reviewed and discussed in this section.

1. *Experimental Studies*

An experimental study on forced convection with boiling inside a vertical porous channel heated symmetrically or asymmetrically was conducted by Cioulachtjian *et al.* [96]. The working fluid was pentane, mainly chosen for its low boiling point. The channel with an aspect ratio of 10 was packed with spherical bronze media ($K = 2.7 \times 10^{-11}$ m^2, $d_p = 0.165$ mm, and $\varepsilon = 0.40$) and was heated from either one or both vertical walls. The Reynolds numbers (based on the particle diameter) for liquid and vapor flow are smaller than 1 and 5, respectively; hence, the experiments were approximately in the Darcy flow regime. Temperature distributions were measured using an array of 130 thermocouples. Although this experimental work was able to generate a 3D temperature distribution, only the 2D results at the midplane were presented. Interesting findings from this study include: (i) a systemic progression of single-phase liquid, to two-phase, and to single-phase vapor structure occurs with time, or with increase in power input, or both, and (ii) all three regions can co-exist within the flow channel at a nonzero liquid flow rate from the bottom. No quantitative information on the two-phase zone could be yielded using thermocouples because it is nearly isothermal.

Most recently, a visualization study of interactive boiling and forced flow in a horizontal, 2D porous formation was performed by Easterday *et al.* [46]. A rectangular test cell was made of acrylic, with inner dimensions of 152.4 mm wide, 58 mm high, and 25.4 mm deep. A heat flux of 10^5 W/m^2 was applied over the central one-third portion of the bottom surface. Numerous thermocouples were mounted inside the test section from the back; the front side was a double-pane insulating window, allowing for direct observations. The other sides of the test section were well insulated, with the front insulation briefly removed at intervals to observe flow conditions, interface location, and two-phase structure, via a camera. The test cell was randomly packed with spherical soda-lime 0.5-mm-diameter glass beads, for which the porosity and absolute permeability were determined to be 0.37 and 1.77×10^{-10} m^2, respectively. Visualization of the two-phase structure on boiling was made by use of black india ink that is fully dissolved into the liquid, but that is nonvolatile. Thus the light intensity level at a certain location directly corresponds to the local liquid saturation. A charge-coupled device (CCD) camera was used to record the location of the phase interface and the light intensity field. The intensity images were then processed to generate liquid saturation plots.

The experimental images of liquid saturation are shown in Figs. 17(a), 18(a), and 19(a) corresponding to the inlet velocities of 0.15, 0.25, and 0.35 mm/s, respectively. In these images the gray scale ranges from black for

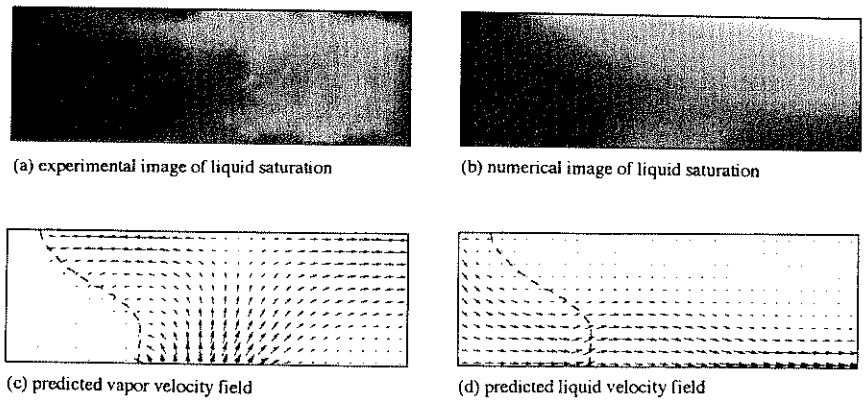

FIG. 17. Experimental and numerical results for $u_{in} = 0.15$ mm/sec [46].

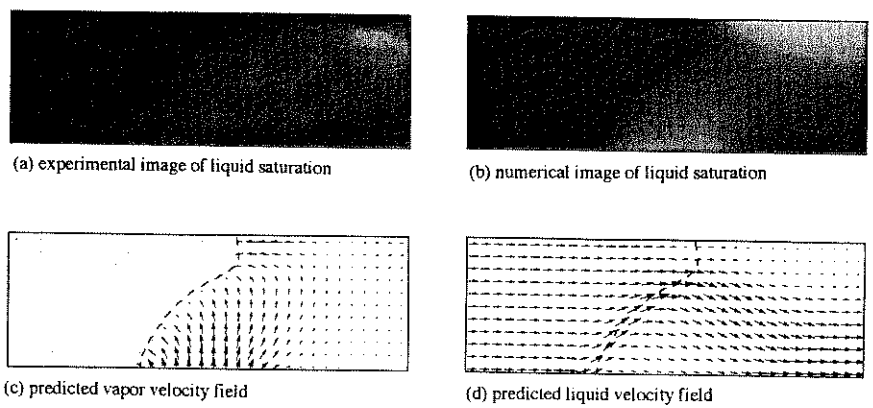

FIG. 18. Experimental and numerical results for $u_{in} = 0.25$ mm/sec [46].

the pure liquid to white for the pure vapor. It can be seen from Fig. 17(a) that the two-phase zone is extensive and the phase interface protrudes forward at the top, reminiscent of the numerical image shown in Fig. 17(b). In addition, the liquid saturation is apparently lower in the upper right-hand region than it is in the vicinity of the heated element. Physically, this phenomenon arises because the much lighter vapor migrates upward on evaporation and subsequently accumulates at the top of the formation. An engineering implication of this result is that in a vapor-dominated geothermal reservoir, the region with most thermal energy (i.e., richest in vapor) may be located significantly away from the heat source. This peculiar

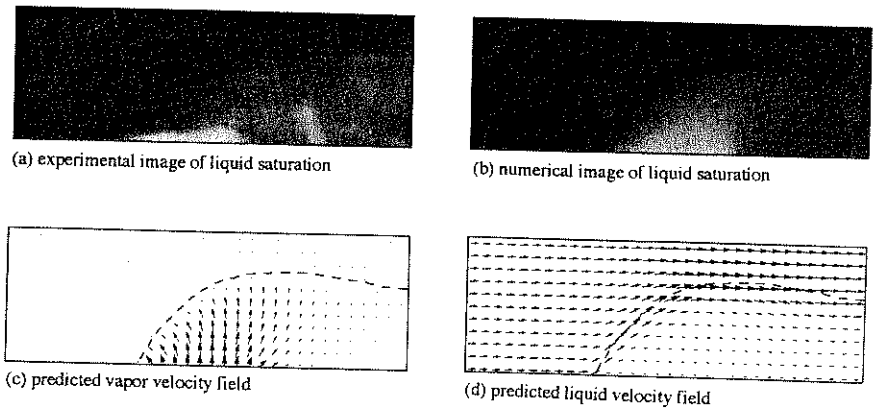

FIG. 19. Experimental and numerical results for $u_{in} = 0.35$ mm/sec [46].

feature of two-phase systems, which contradicts the common knowledge of single-phase heat transfer, clearly demonstrates the need for two-phase flow studies.

At a higher incoming flow (i.e., $u_{in} = 0.25$ mm/sec), the experimental image displayed in Fig. 18(a) shows a receding two-phase zone away from the inlet. It also is clearly visible that the upper right-hand region is saturated more with vapor (lighter in color), whereas the lower right-hand corner is full of liquid (darker). Again, this experiment confirms the second type of two-phase structures predicted by the numerical model (Fig. 18(b)). For the highest flow rate, both the experimental (Fig. 19(a)) and numerical (Fig. 19(b)) images show a dome-shaped two-phase zone underlying a pure liquid region. Despite the gravitational instability, the structure of the liquid layer over the two-phase zone appears stable, as shown in Fig. 19(a). The theoretical underpinning for this stable structure remains unknown.

2. *Numerical Analysis Using the Multiphase Mixture Model (MMM)*

The previous numerical images of the liquid saturation were obtained by Easterday *et al.* [46] based on the two-phase mixture model of Wang and Beckermann [51]. Employing a 62×22 grid, a typical simulation for this problem required CPU time of only 10 min on a Hewlett Packard 715/75 workstation. To help understand the formation of the two-phase patterns displayed in panels (a) and (b) of Figs. 17 to 19, more detailed numerical results of vapor and liquid velocity fields are presented in panels (c) and (d) of Figs. 17 to 19.

For the case of a low inlet velocity (i.e., $u_{in} = 0.15$ mm/sec), strong vapor upward flow is seen (Fig. 17(c)). When the vapor rising from the bottom heater reaches the impermeable top surface, it spreads over along both directions. The vapor flowing toward the phase interface is condensed, while the other vapor stream is carried away by the liquid toward the exit. Figure 17(d) shows that the liquid preferentially flows along the bottom surface of the channel where the liquid saturation is higher, bypassing the upper region where liquid saturation is lower and therefore resistance to liquid flow is higher. This preferential liquid flow provides an effective means to wet the heated surface.

When the inlet velocity of the liquid increases to 0.25 mm/sec (Fig. 18(c)), the vapor flow splits into two before reaching the top surface, one flowing toward the phase interface (i.e., the condensation front), and the other mixing with the liquid to exit from the channel. The liquid velocity shown in Fig. 18(d) indicates that the liquid flow remains nearly horizontal until reaching the phase interface. Inside the two-phase zone, the liquid tends to bypass both regions that are rich in vapor, namely, around the bottom heated surface and along the top of the formation.

Inspection of Fig. 19(c) for the highest liquid incoming velocity (i.e., 0.35 mm/sec) reveals that the vapor generated from the bottom surface rises to the phase interface lying above and is condensed completely there. Thus the upper one-third portion of the channel is fully saturated with liquid. In this region, the pure liquid flows over the two-phase dome despite the gravitational instability (Fig. 19(d)). The underlying two-phase dome acts as a restriction to the liquid flow and forces the liquid to bypass it.

Most recently, a fixed-grid numerical algorithm based on MMM was developed for general problems that may simultaneously involve all three regions: superheated vapor, two-phase, and subcooled liquid [46a]. The algorithm was successfully applied to simulate the above problem under post-dryout conditions.

3. *Large-Scale Numerical Simulation*

Although the foregoing laboratory-scale experimental and numerical studies have shed considerable light on the fundamental processes of boiling in a forced flow through porous media, there is a need to conduct large-scale numerical simulation for geothermal applications involving length scales on the order of kilometers. Such work has been extensively reported in a separate branch of research focused on geothermal energy exploitation [97–99]. A primary objective of these modeling studies has been to provide answers to reservoir management questions relating to well decline, well spacing, generating capacity (power potential) of the

reservoir, injection effects, and scaling problems. The numerical simulations also aimed at predicting premature breakthrough at the production wells during cold-water injection for reservoir recharge. The preferential passing would drastically reduce the enthalpy and temperature of the produced fluids. Figure 20 schematically illustrates a typical production–injection system for a doublet in a geothermal reservoir [97]. It is of particular interest to predict the movement of cold-water fronts in the modeling of fluid injection processes. Such fronts cannot be adequately resolved on the spatial scale traditionally used in discretizing flow domains (10 to 100 m or more) based on the MFM, and hence large numerical diffusion is inevitable [97]. Conversely, if based on the newly developed MMM, spatial resolution of the large-scale reservoir simulation can be greatly improved due to the much reduced computational time associated with MMM. This may be a promising area for future research.

D. External Condensing Flows

Phase change flows in unbounded porous media are encountered in numerous important technological applications. Examples include boiling flow along an igneous intrusion in geothermal reservoirs and condensing flow adjacent to a cold surface in heat pipes and porous insulation materials. Recently, there has been much research on the external condensing flow as related to enhanced condensation heat transfer in porous

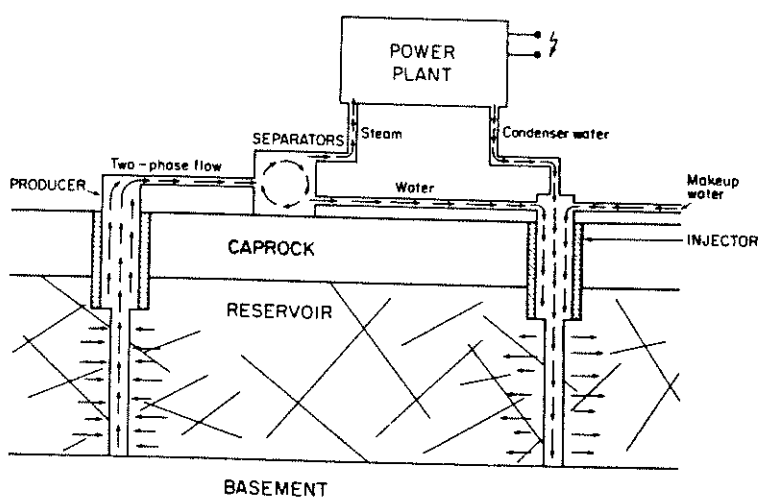

FIG. 20. Schematic illustration of an injection–production geothermal system [97].

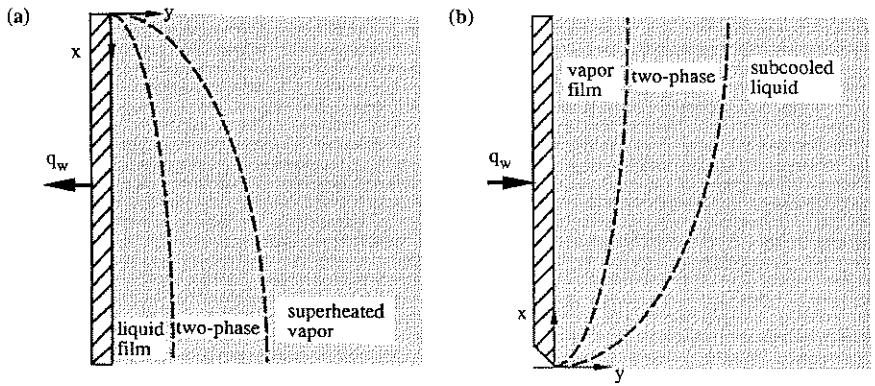

FIG. 21. External (a) condensing flow and (b) boiling flow in porous media. q_w, wall heat flux.

media [43, 100–102]. Figure 21(a) illustrates a typical three-region structure of external condensing flow in porous media, where the two-phase zone arises from the capillary effect. As the heat extraction rate increases, the liquid saturation on the cold wall increases up to unity, after which a pure liquid film begins to form adjacent to the wall. A complete problem of external condensation then involves multiple regions consisting of the pure liquid film, the two-phase zone, and the infinitely large superheated vapor region. The flow dynamics in such systems are driven by relative buoyancy forces between liquid and vapor, external pressure gradients, or both.

1. *Single-Phase Analysis*

If we neglect the two-phase zone, following the original study of Cheng [100], the condensation problem is then reduced to a single-phase transport counterpart within the liquid condensate film. Such analyses would be conceptually similar to the pioneering work by Nusselt [103] for vapor condensation in the absence of porous materials. Typical assumptions made in these analyses include

1. The interface between vapor and liquid is sharp and smooth
2. Classic boundary layer approximations are valid
3. The porous medium is isotropic.

Further assuming Darcy flow, Cheng [100] obtained the following similarity solution:

$$\mathrm{Nu}_x/\mathrm{Ra}_x^{1/2} = \left(\frac{1}{2\mathrm{Ja}} + \frac{1}{\pi}\right)^{1/2}, \tag{52}$$

where Nusselt, Rayleigh, and Jacob numbers are defined, respectively, as

$$\mathrm{Nu}_x = \frac{hx}{k_{\mathrm{eff}}}, \quad \mathrm{Ra}_x = \frac{K(\rho_l - \rho_v)gx}{\mu_l \alpha_l}, \quad \mathrm{Ja} = \frac{c_l(T_{\mathrm{sat}} - T_w)}{h_{fg}}. \tag{53}$$

2. *Two-Phase Boundary Layer Approximations*

In view of the fact that the mathematical characteristics of the governing equations in MMM for two-phase flow are similar to those governing single-phase flow, a two-phase boundary layer theory, that parallels the single-phase boundary layer theory of Schlichting [104], is conceivable. By carrying out a formal perturbation analysis, Wang and Beckermann [105] found that the two-phase boundary layer approximations are valid when the two-phase Peclet number is much larger than unity; namely,

$$\mathrm{Pe}_{2\phi} \equiv \frac{u_\infty L}{(\varepsilon K)^{1/2}\sigma/\mu_l} \gg 1, \tag{54}$$

where u_∞ is the uniform velocity at infinity in pressure-driven flows or the scaling velocity $K(\rho_l - \rho_v)g/\mu_l$ in buoyancy-driven flows. Physically, the two-phase boundary layer approximations imply that the mixture velocity component along the surface dominates the one perpendicular to it, and that changes across the two-phase boundary layer are much steeper than those along it.

3. *Two-Phase Analysis Using the Unsaturated Flow Theory*

Several attempts have been made to include the two-phase zone and, hence, the capillary effect in the analysis of condensation heat transfer inside porous media [42, 43, 101]. In order to render the problem analytically tractable, these theoretical studies based on MFM had to neglect the vapor flow. More specifically, the vapor phase was assumed to remain at a constant pressure and a two-phase flow problem thus was essentially reduced to the consideration of the liquid phase flow only. This approach is equivalent to the unsaturated flow theory discussed in Part II, Section C. The key equation governing the two-phase condensing flow based on UFT is [43]

$$\frac{(\varepsilon K)^{1/2}\sigma}{\nu_l}\frac{\partial}{\partial y}\left\{k_{rl}(s_l)\left[-J'(s_l)\right]\frac{\partial s_l}{\partial y}\right\} - \frac{K\Delta\rho}{\nu_l}g\frac{dk_{rl}}{ds_l}\frac{\partial s_l}{\partial x} = 0. \tag{55}$$

The solution to Eq. (55) along with appropriate boundary conditions eventually determines the capillary effect on condensation heat transfer in porous materials.

4. *Two-Phase Analysis Using the Multiphase Mixture Model (MMM)*

Within the framework of MMM, a set of boundary layer equations has been rigorously derived by Wang and Beckermann [105] without invoking the Richards approximation associated with UFT. In the Cartesian coordinate system shown in Fig. 21, the mixture continuity equation, the mixture Darcy law, and the liquid mass conservation equation can be written explicitly as

$$\frac{\partial(\rho u)}{\partial x} + \frac{\partial(\rho v)}{\partial y} = 0, \tag{56}$$

$$\rho u = -\frac{K}{\nu}\left(\frac{\partial p}{\partial x} - \rho_k g\right), \tag{57}$$

$$\rho \frac{d\lambda}{ds_l}\left(u\frac{\partial s_l}{\partial x} + v\frac{\partial s_l}{\partial y}\right) = \frac{\partial}{\partial y}\left(\rho D_c \frac{\partial s_l}{\partial y}\right) - \frac{K\Delta\rho}{\nu_v} g \frac{df}{ds_l}\frac{\partial s_l}{\partial x}, \tag{58}$$

where the mixture transport properties are all functions of the local liquid saturation s_l. It is worth noting that Eqs. (56) to (58) strongly resemble the boundary layer equations for single-phase binary mixture flow and transport in porous media. In the limit corresponding to UFT (i.e., $\bar{\nu} \to \infty$), it was shown by Wang and Beckermann [106] that

$$\frac{d\lambda}{ds_l} = O(\bar{\nu}^{-1}) \to 0; \quad \rho D_c \to \frac{(\varepsilon K)^{1/2}\sigma}{\nu_l} k_{rl}(s_l)[-J'(s_l)];$$

$$\frac{1}{\nu_v}\frac{df}{ds_l} \to \frac{1}{\nu_l}\frac{dk_{rl}}{ds_l} \tag{59}$$

so that Eq. (58) identically reduces to Eq. (55) of UFT.

In the case of buoyancy-driven condensing flow, Eqs. (56) to (58) admit a similarity solution in terms of the following similarity variables [106]:

$$\eta = \frac{y}{x}\mathrm{Ra}_{2\phi}^{1/2}, \quad \Psi = \rho D_c \mathrm{Ra}_{2\phi}^{1/2} F(\eta), \quad s_l = s_l(\eta), \tag{60}$$

where the two-phase Rayleigh number $\mathrm{Ra}_{2\phi}$ is defined as

$$\mathrm{Ra}_{2\phi} = \frac{K(\rho_l - \rho_v)gx}{(\varepsilon K)^{1/2}\sigma}, \tag{61}$$

and Ψ is a stream function of the two-phase mixture such that

$$\rho u = \frac{\partial \Psi}{\partial y} \qquad \rho v = -\frac{\partial \Psi}{\partial x}. \tag{62}$$

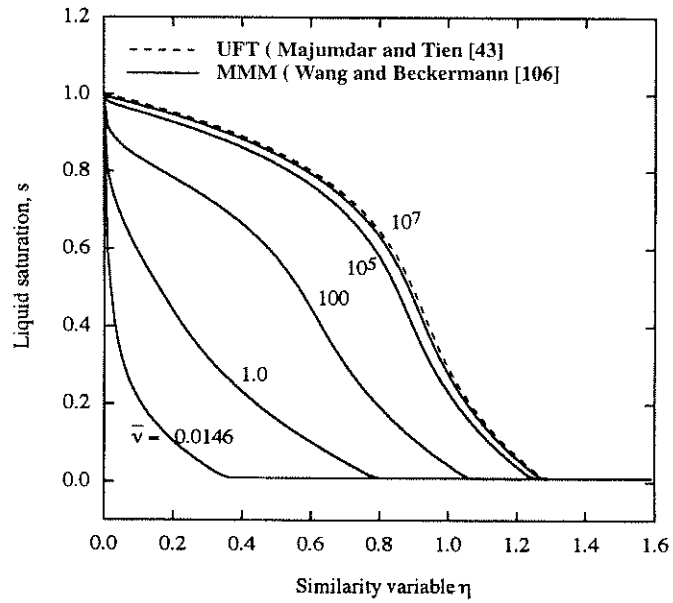

FIG. 22. Saturation profiles of two-phase boundary condensing flow as predicted by the two-phase mixture model [106] and the unsaturated flow theory [43]. UFT, unsaturated flow theory; MMM, multiphase mixture model.

Figure 22 shows the liquid saturation profiles for different values of the viscosity ratio along with the curve obtained using UFT. The latter is independent of the viscosity ratio $\bar{\nu}$ [43]. It can be seen that the curves indeed approach the limiting case represented by UFT. However, the value of $\bar{\nu}$ needed for UFT to hold true is surprisingly large—$\bar{\nu} = 10^7$! Obviously, for all common fluids, this condition cannot be satisfied, implying that UFT is generally questionable when applied to the condensation problem under consideration. In fact, for a water–steam system at atmospheric pressure ($\bar{\nu} = 0.01466$), the saturation profile predicted by MMM greatly deviates from that of UFT.

The capillary effect on condensation heat transfer is reflected by the liquid mass flux across the interface between the two-phase zone and the pure liquid film. It was shown by Wang and Beckermann [106] that UFT overpredicts this flux by a factor of 66, suggesting that the previous theoretical studies based on UFT [43, 101] have probably exaggerated the effect of capillary forces on condensation heat transfer in porous media. The overprediction results from the neglect of the vapor flow, which is actually very strong due to the low vapor density.

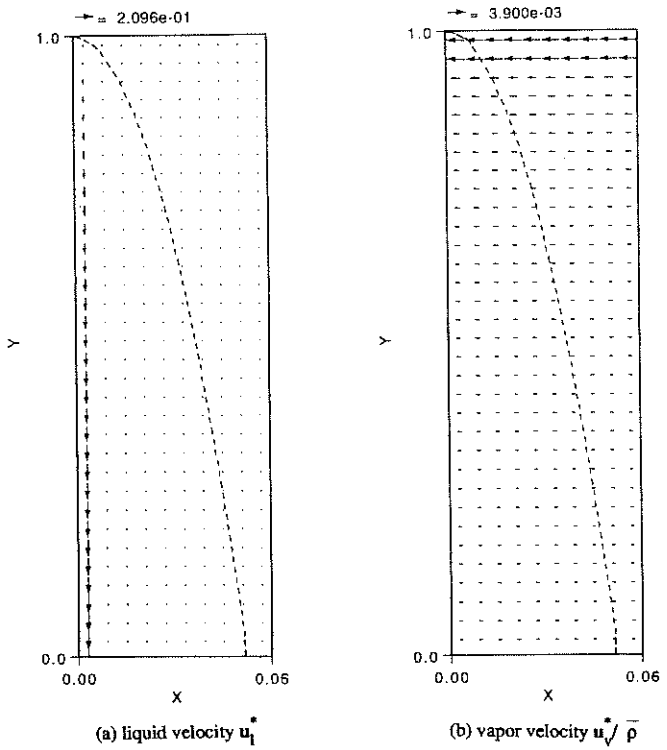

FIG. 23. Two-phase flow pattern in the external condensing case: (a) liquid velocity u_l^*, and (b) vapor velocity $u_v^* \bar{\rho}$ [106]. Dashed line, edge of the boundary layer.

Figure 23 displays representative liquid and vapor flow fields in a two-phase boundary layer of buoyancy-driven flow along a cooled vertical flat plate. The dashed line in these plots denotes the edge of the boundary layer. The liquid flow is essentially confined to a region adjacent to the cooled wall, where the vapor condenses into the liquid. As a result of its large density, the liquid moves primarily downward (see Fig. 23(a)). The downward liquid velocity quickly diminishes with the distance away from the wall, because it is proportional to the cubic of the liquid saturation, which furthermore has an extremely steep profile (see Fig. 22). Figure 23(b) shows that the vapor is only laterally entrained into the two-phase boundary layer. A two-phase cross-flow pattern is characteristic of condensing buoyancy-driven flows.

5. *Experimental Studies*

Quantitative comparisons of the foregoing two-phase analysis with the available condensation experiments [102, 107] have not been attempted for the reasons explained in Wang and Beckermann [106]. However, qualitative insight into the capillary effect can be gained from Fig. 24, which compares the single-phase theory of Cheng, the UFT model of Majumdar and Tien, and the refined two-phase model of Chung et al. with the experimental data for a porous medium consisting of small glass beads by Chung *et al.* Under the experimental conditions, the Darcy flow assumption is likely to be valid, and therefore the differences between various model predictions are mainly attributed to the capillary effect and, hence, the inclusion of the two-phase zone. As is clearly seen, the experimental data suggest that the UFT model of Majumdar and Tien significantly overpredicts the capillary effect, confirming the argument made earlier.

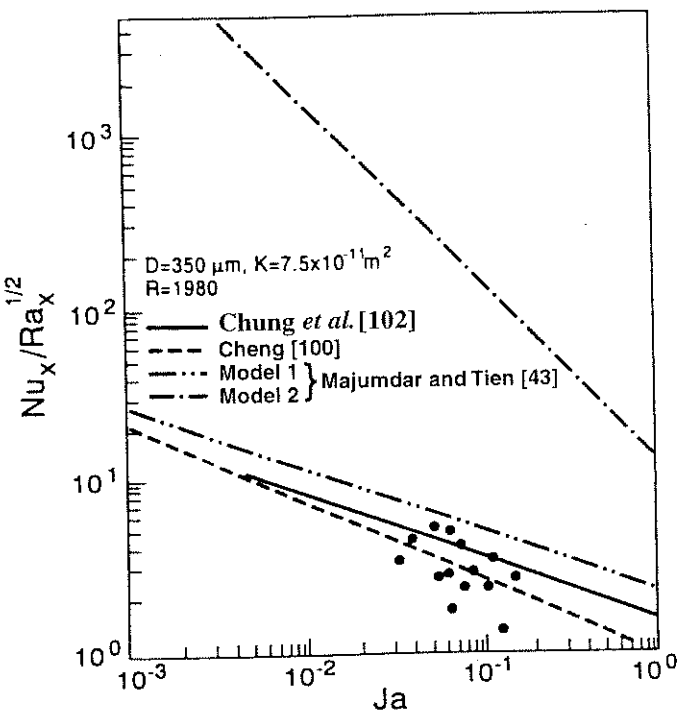

FIG. 24. Comparison of condensation heat transfer data with theories [102]. Nu, Nusselt; Ra, Rayleigh; Ja, Jacob.

The difference between the curves of Cheng and Chung is relatively small, implying that the capillary effect is insignificant in these experimental situations.

6. *Additional Issues*

The two-phase analysis of Wang and Beckermann [106] for boundary layer condensing flows focused on the development of the two-phase zone before a condensate film appears along the cold wall. Beyond the marginal condition, at which the liquid saturation at the wall becomes equal to unity, the two-phase analysis presented in the previous section needs to be modified to couple the single-phase flow within the liquid film; this can be done readily, as in many previous models. The two-phase analysis still would be valid, except that the phase interface now becomes permeable. As a result, the normal mixture velocity v is no longer zero, as specified in the above analysis, but must be obtained from the coupling between the single-phase and two-phase flows. Such an extension, although straightforward, needs to be performed in the future. In addition, neither analysis nor experiment has been performed on pressure-driven condensing flows in porous media with two-phase effects.

E. External Boiling Flows

Pool and external boiling in porous media is a time-honored research area. To date, theoretical work in the literature typically followed the standard film boiling model in the absence of porous media. The analyses were developed in parallel with that for condensing flow, as discussed in the preceding section. Hence, the following discussion on the theoretical aspects of boiling in porous media will be brief. To facilitate discussion, a sketch of the flow structure and nomenclature for external boiling along a vertical wall is illustrated in Fig. 21(b).

1. *Single-Phase Analysis of Film Boiling*

In one of the first studies on external boiling in porous media, Parmentier [108] assumed that a thin vapor film forms adjacent to the heated surface when boiling occurs, and that the vapor film and the pure liquid region of semi-infinite extent are separated by a sharp interface with no mixed region in between. As a result of this approximation, the mathematical formulation of the boiling problem was simplified to a single-phase version. Within this theoretical framework, Cheng and Verma [109] subsequently studied subcooled boiling on a vertical surface. They

reported that the following relationship exists:

$$\mathrm{Nu}_x \sim \sqrt{\mathrm{Ra}_x}, \tag{63}$$

where the proportionality constant is a function of various dimensionless parameters defined as

$$\mathrm{Nu}_x = \frac{hx}{k_{\mathrm{eff}}}, \quad \mathrm{Ra}_x = \frac{K(\rho_l - \rho_v)gx}{\mu_v \alpha_v}, \quad R = \frac{\rho_v}{\rho_l}\left[\frac{\mu_l \alpha_v (\rho_l - \rho_v) c_l}{\mu_v \alpha_l \rho_l \beta_l h_{fg}}\right]^{1/2},$$

$$\mathrm{Ja} = \frac{c_l(T_{\mathrm{sat}} - T_\infty)}{h_{fg}}, \qquad \mathrm{Sh} = \frac{c_c(T_w - T_{\mathrm{sat}})}{h_{fg}}. \tag{64}$$

Figure 25 shows the dependence of the Nusselt number on wall superheat Sh for $R = 0.05$ and various liquid subcooling Ja. As can be expected, the heat transfer coefficient decreases with wall superheat but increases with liquid subcooling. It should be mentioned that this theory neglecting the presence of a two-phase zone has not been directly verified by experiments.

2. *Two-Phase Analysis Using the Multiphase Mixture Model*

In a unified treatment, Wang and Beckermann [106] also studied buoyancy-driven boiling flow in the two-phase zone adjacent to a heated vertical flat plate, and developed a similarity solution. An important result

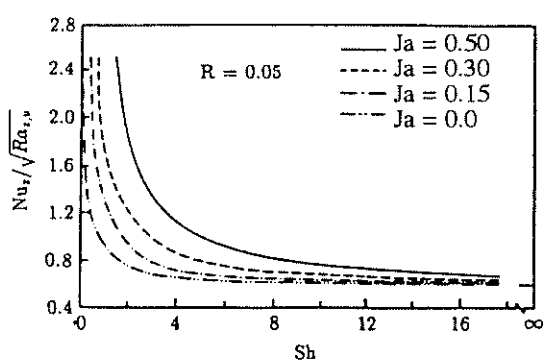

FIG. 25. Single-phase predictions of subcooled film boiling heat transfer in porous materials [109]. Nu, Nusselt; Ra, Rayleigh; Sh, Sherwood; Ja, Jacob.

from that study is the dryout heat flux corresponding to zero liquid saturation at the wall, which is given by

$$q_{\text{dry}} = 2.716 \times 10^{-3} \frac{h_{fg}\sigma}{\nu_l}\left(\frac{\varepsilon K}{L^2}\right)^{1/4}\left[\frac{(\rho_l - \rho_v)gK}{\sigma}\right]^{1/2}. \quad (65)$$

For a water–steam system with $\varepsilon = 0.4$, $K = 10^{-10}$ m^2, and $L = 0.1$ m, this equation estimates a dryout heat flux of 2.45×10^4 W/m^2. Note that the dryout heat flux is proportional to the three-fourths power of permeability and is inversely proportional to the square root of the heating length.

Figure 26 depicts the liquid and vapor phase velocity fields, respectively, in a typical two-phase boiling boundary layer at $\text{Ra}_{2\phi,L} = 50$ [106]. The dashed lines in these plots represent the edge of the boundary layer. The

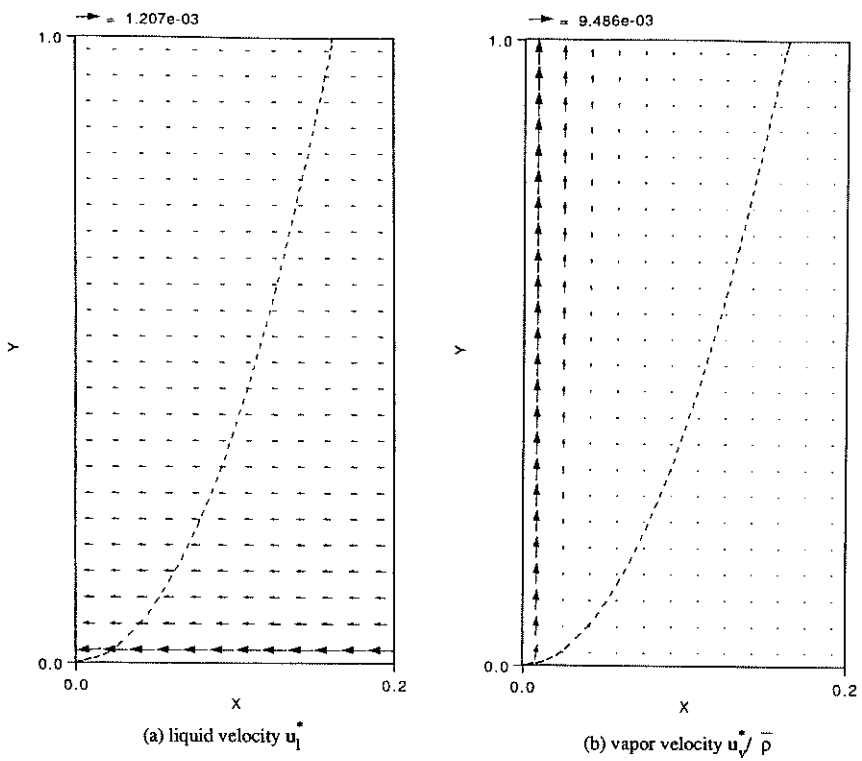

FIG. 26. Two-phase flow pattern in the external boiling case: (a) liquid velocity $\mathbf{u}_l^*$, and (b) vapor velocity $\mathbf{u}_v^*\bar{\rho}$ [106].

vapor moves primarily vertically upward due to the large density difference between liquid and vapor. The liquid is laterally entrained into the boundary layer. Once again, the two-phase cross-flow pattern is characteristic of buoyancy-driven boiling flows in porous media.

In contrast, the dryout heat flux in a pressure-driven boiling flow was found to be given by [105]

$$q_{\text{dry}} = 2.9 \times 10^{-3} \frac{h_{fg}\sigma}{\nu_l}\left(\frac{\varepsilon K}{L^2}\right)^{1/4}\left(\frac{u_\infty \mu_l}{\sigma}\right)^{1/2}. \quad (66)$$

Equation (66) gives a dryout heat flux of 4.04×10^4 W/m^2 for a water–steam system with $\varepsilon = 0.4$, $K = 10^{-10}$ m^2, and $L = 0.1$ m, and with an upward flow of $u_\infty = 5$ mm/sec. Neither Eq. (65) nor (66) has been verified experimentally. Nonetheless, it provides a simple estimate and a useful boundary of the dryout heat flux in various types of external boiling flow.

3. *Experimental Studies*

Limited experimental studies of boiling in porous media are available. Schrock *et al.* [110] performed the first study on boiling from horizontal cylinders placed in liquid-saturated sands with the particle diameters ranging from 0.16 to 1.5 mm. It was noted that with smaller particles the critical heat flux was lower than that without particles and a smooth transition occurred from nucleate boiling to film boiling regimes. The lower critical heat flux is probably caused by the difficulty in removing vapor from the heated surface through interstitial spaces. Fukusako *et al.* [111] obtained experimental curves of boiling over a horizontal heated plate embedded in a liquid-saturated porous layer. Steel, glass, and worked iron particles of 1 to 16.5 mm in diameter were used. Water, Freon-11, and Freon-113 were the test fluids. Fukusako *et al.* also found that for small particles (i.e., $d_p = 1$ to 2 mm), the heat flux increased monotonically with temperature during the transition from nucleate to film boiling, as shown in Fig. 27. Moreover, the heat flux in nucleate boiling was higher with small particles than that for large particles or without particles for the same superheat. They hypothesized that the particles constituting the porous medium serve as additional nucleation sites that are activated at low wall superheats, and furthermore, enhance heat transfer through fin effects. Nucleate boiling on a sphere placed in a coarse porous medium ($d_p = 2.9$ to 19 mm) saturated with Freon-113 was investigated by Tung and Dhir [112]. Similar behavior was observed.

Presently, there is a lack of the fundamental understanding of microscopic evaporation and bubble dynamics on the pore level, macroscopic

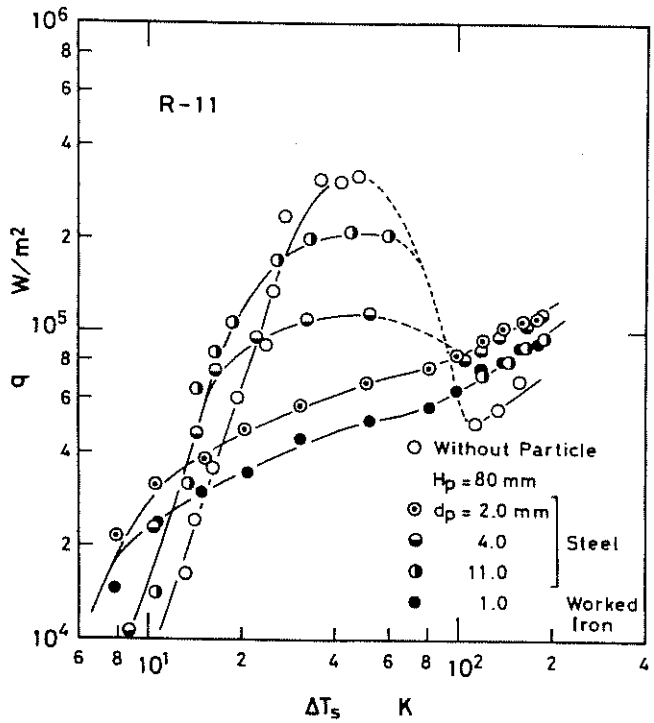

FIG. 27. Boiling curves in particulate beds saturated with Freon-11 for various particle diameters [111].

two-phase transport on the system scale, and their couplings during boiling in porous media. For example, it remains unclear how the capillary forces would influence movement of vapor bubbles away from the heated surface and liquid toward the heated surface. Dhir [6] has presented an insightful discussion on various fundamental issues related to boiling in porous media. This excellent review excluded the abundant literature of boiling in heat pipes and structured surfaces for heat transfer augmentation, because these problems typically feature a thin layer of porous materials, thus invalidating a continuum treatment of multiphase flow and heat transfer in porous media.

F. Steam Injection

Another type of two-phase flow and heat transfer problems occurs during immiscible displacement in porous media, as usually encountered in enhanced oil recovery and remediation of contaminated soils. For example, steam injection into a reservoir results in displacement of the initial pore fluids. Thus the rate of mass displaced out of the reservoir is substantially greater than the injection mass flow rate of steam. Figure 28 schematically illustrates the process of steam injection into a porous formation that is partially filled with either petroleum hydrocarbons in an oil recovery scenario or with water-immiscible contaminants in a groundwater contamination context. Steam is injected into the reservoir through vertical wells, allowed to sweep through the oil- or contaminant-rich regions, and then removed together with the mobilized volatile and semivolatile hydrocarbons. The principal mechanisms for oil or contaminant recovery in steam injection include

1. Steam distillation
2. Increased mobilization due to the decreasing viscosities with temperature
3. Displacement and dilution by the steam condensation front
4. Reduction in the amount of absorption into soil at elevated temperatures.

All these mechanisms are largely controlled by complex transport phenomena that occur during steam injection. They include phase change heat transfer, mass transfer of components between the phases, and multiphase simultaneous flows driven by the viscous, gravitational, and capillary forces.

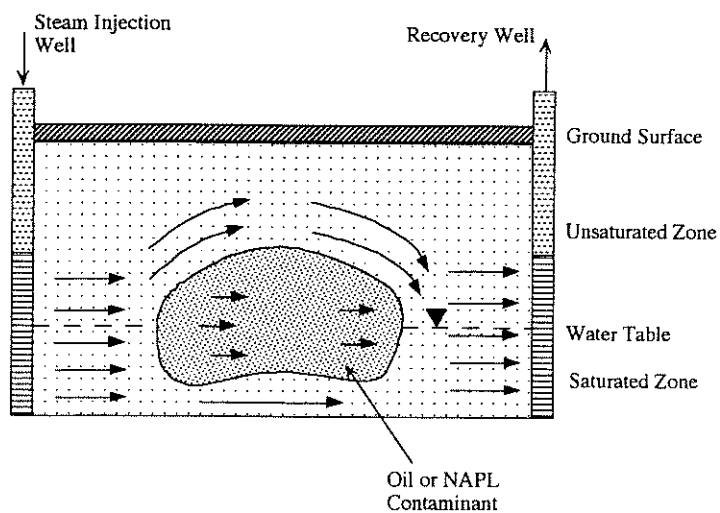

FIG. 28. Schematic illustration of steam injection into porous media. NAPL, nonaqueous phase liquids.

Moreover, these transport phenomena are inherently transient and multidimensional. Even in an idealized homogeneous reservoir, the injected steam tends to bypass the oil- or contaminant-present zones because they offer lower permeabilities to steam flow, thus resulting in a multidimensional scenario as shown in Fig. 28. In realistic geologic media, the multidimensional behavior of steam injection is further exacerbated by the reservoir heterogeneity. Certain physical phenomena may also contribute to multidimensional characteristics; for example, gravity override of steam where the light steam tends to rise to the top of the formation, thus leading to a premature breakthrough of steam into production wells. The detrimental outcome of steam override is a large reduction in the recovery rate and a significant waste of applied thermal energy (i.e., latent heat energy). In addition, buoyancy-driven flows in various phases due to both thermal and solutal gradients can result in the strongly multidimensional behavior and alter evaporation rates of oil or NAPL components at the condensation front. The role of natural convection in multiphase transport in porous media so far, has been little explored.

There is a wealth of information on steam injection for enhanced oil recovery in the petroleum industry. Examples are the experimental study of Baker [113], and the numerical work of Coats [114, 115]. However, because of the considerable commercial value of this technology, limited studies have been published in the open literature, and a fundamental understanding of the steam injection process remains proprietary. This is why a recent environmental application, that is, groundwater contamination by NAPLs and subsequent remediation by steam injection, has renewed great interest in this rather old problem [48, 55, 116, 117]. In addition, there are fundamentally different issues and approaches involved in the two types of applications. For example, in groundwater remediation, considerable attention must be given to the critical issue of complete disappearance of the NAPL, while the objective of oil recovery is to remove as much hydrocarbon from a formation as is economically feasible.

This review thus is restricted to the most recent work existing in the open literature and is focused on the fundamentals. While vapor displacement of the same-component liquid will be reviewed shortly, the topic of displacement of multicomponent fluids is deferred to Part IV.

1. *Experimental Studies*

Several experimental studies of 1D steam injection systems have appeared in the literature [55, 118–120]. In the absence of gravity, a steam condensation front propagates in the direction perpendicular to the injection velocity. The laboratory-scale experimental data demonstrated that steam injection is a viable method for contaminant recovery [55].

Experimental data of multidimensional steam injection are quite scarce. An injection of dry steam into an initially water-saturated porous medium was undertaken by Basel and Udell [116]. The test section consisted of a 2D rectangular bed. It was observed that the angle of the propagating steam front (with respect to the gravity direction) was a function of the ratio of gravitational to viscous forces. Basel and Udell [116] mapped the location of the steam front using liquid crystals formulated for color change at the boiling temperature of water. A thin layer of crystals was painted onto the innermost pane of the front side of the test section. Propagation of the front with time for different media permeabilities was reported. Later, Basel and Udell [121] experimentally examined the condensation front location in steam injection into a heterogeneous porous medium consisting of three homogeneous horizontal layers of different permeabilities.

2. *One-Dimensional Analytical Studies*

Basel and Udell [116] also developed a 1D analytical model for a dry steam front infiltrating an initially water-saturated bed. Neglecting capillary forces, the model formulated the hydrodynamic force and energy balance equations, and predicted the propagation velocity and angle (with respect to gravity) of the steam front. It was found that the angle of the steam condensation front is critically dependent on the ratio of gravitational forces to vapor phase viscous forces. A qualitatively good agreement was achieved between their model prediction and experimental data.

3. *Multidimensional Numerical Modeling*

Accurate analysis of multidimensional two-phase flow and heat transfer in porous media is intrinsically complicated and prohibitive for the reasons discussed in Part II. Chung and Catton [122] studied numerically the steam injection process into a forced water flow through a porous medium. A steam bubble develops around the injector that can either grow or become steady with time, depending on the heat removal rate at the phase interface separating the vapor and subcooled liquid regions. An important assumption made in this analysis was that there exists no two-phase zone between the two single-phase regions. Despite this simplification, the fundamental difficulty of tracking the moving and irregular phase interface is still present. A coordinate transformation was employed to find the location of the phase interface under steady-state conditions. An integral

solution was obtained to predict the vapor bubble size. It was concluded that the thermal dispersion effect is of paramount importance to achieve good agreement between theory and experiment. Applicability of this conclusion to transient steam injection processes, however, seems invalid. In fact, in a most recent study on steam injection into multidimensional porous reservoirs, Wang [48] found that the phase interface location was not affected by thermal dispersion in the subcooled liquid region.

Wang [48] described a fundamental study of steam injection into an initially water-saturated 2D reservoir. Emphasis was placed on elucidating various fundamental phenomena such as steam override, two-phase flow patterns, evaporation heat transfer, and natural convection in both phases caused by thermal gradients. The theoretical basis of this numerical study was MMM. Model assumptions included: (i) the generalized Darcy law for two-phase flow, (ii) isothermal two-phase zone, and (iii) local thermal equilibrium among the vapor, liquid, and solid phases. The numerical model was first validated against the 1D experiments of Hunt *et al.* [55], and good agreement was found between the measured and calculated steam front locations, as shown in Fig. 29. The 2D simulations were then compared with the three experiments of Basel and Udell [116], corresponding to different injection mass fluxes. Such a comparison is shown in Fig. 30, in which the steam condensation front profiles are plotted at various dimensionless times known also as the pore volumes. The pore volume is defined as the number of pore volumes filled with injected steam; namely,

$$\text{Pore volumes} = \frac{\text{Volume of injected steam}}{\text{Pore volume of formation}} = \left(\frac{\dot{m}_{\text{in}}}{\rho_v \varepsilon L_w}\right) t. \qquad (67)$$

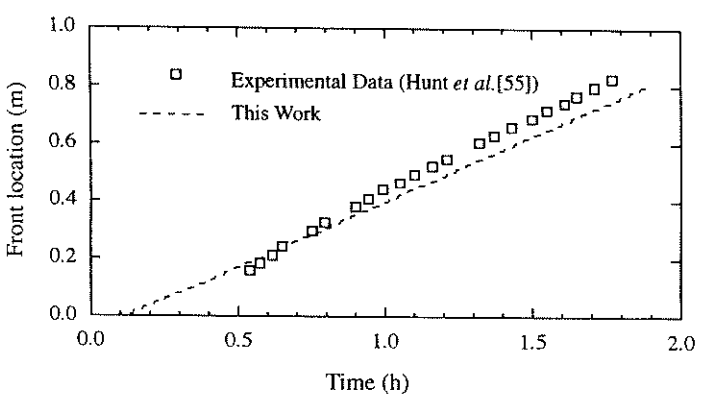

FIG. 29. Comparison of experimental and predicted steam front locations in a one-dimensional silica sand column [48].

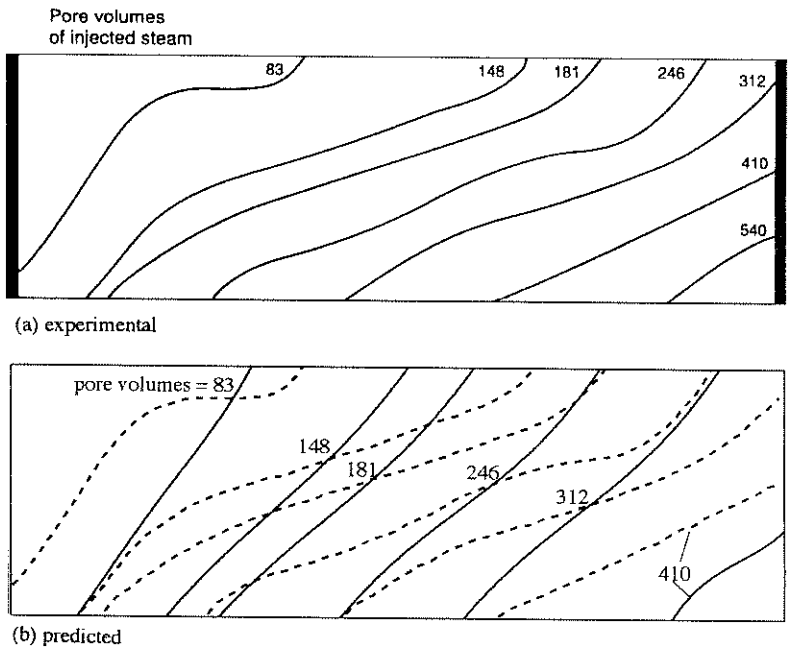

FIG. 30. Comparison of predicted (solid lines [48]) and measured (dashed lines [116]) two-dimensional steam front profiles for the injection mass flux of 0.0274 kg/m^2 · sec.

Apparently, the pore volume is equivalent to a dimensionless time. It can be seen from Fig. 30 that the predicted curves are in reasonable agreement with those measured experimentally [116]. In particular, there seems to be good agreement in terms of the mean front location as a function of time. The experimental fronts, however, are more inclined from the vertical than are the predicted counterparts. This can be explained by the fact that during experimental preparation a high permeability zone is created at the top of the sandpack, which allows the injected steam to preferentially invade along the top [116, 123]. The influence of this more permeable layer at the top of the sandpack on the measured steam front profiles is clearly visible, (see the dashed lines in Fig. 30). No attempt was made by Wang [48] to adjust the permeability of the upper region of the sandpack to reconcile the discrepancies displayed in Figs. 30.

To elucidate the fundamental transport phenomena occurring during steam injection, representative results of the temperature distribution ahead of the condensation front, liquid saturation contours within the

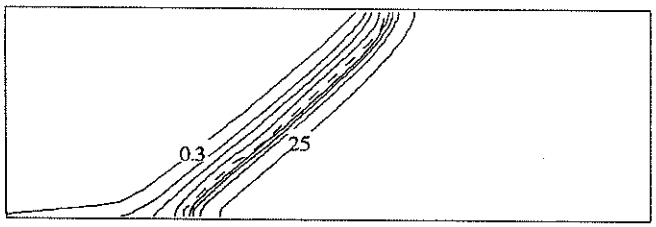

(a) Liquid saturation contours and isotherms

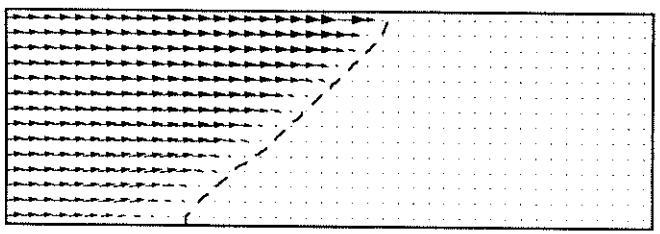

(b) vapor velocity vectors (m/s)

→ = 8.48e-02

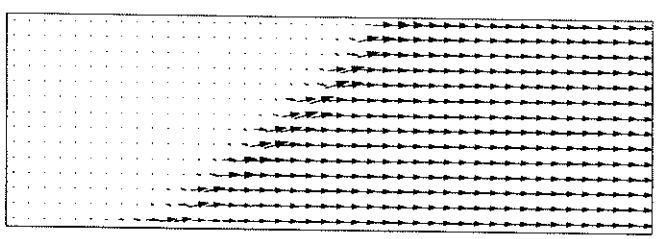

(c) liquid velocity vectors (m/s)

→ = 1.75e-04

FIG. 31. Numerical results for two-dimensional steam injection at the instant of 0.4 h: (a) liquid saturation contours ($\Delta s = 0.2$) in the two-phase zone (left to the dashed line) and isotherms ($\Delta T = 15°C$) in the pure liquid region (right to the dashed line); (b) vapor velocity field; and (c) liquid velocity field. The steam front is denoted by the dashed line [48].

two-phase zone, and vapor and liquid velocity fields are shown in Fig. 31 for the injection mass fluxes of 0.0274 kg/m^2 · sec. In Fig. 31, the isotherms are plotted for temperatures between 25 and 70°C, with an equal increment of 15°C, and the liquid saturation contours from 0.3 to 0.9, with an increment of 0.2. It can be seen from Fig. 31(a) that the steam front denoted by the dashed line is rather inclined, indicating that the gravitational forces dominate the viscous forces. Far behind the steam front, the liquid saturation is nearly constant at the residual value, that is, 0.2. Major changes in the temperature and liquid saturation occur over very small distances in the proximity of the steam condensation front. This unique feature of the steam front would invalidate the use of coarse grids, as was done by Falta [123]. The vapor motion in the two-phase zone is primarily horizontal and uniform except in the neighborhood of the condensation front (as shown in Fig. 31(b)) where the vapor velocity drastically decreases due to steam condensation. As a result, the liquid saturation increases rapidly, as can be seen from Fig. 31(a). The liquid motion features somewhat intricate characteristics in the vicinity of the condensation front, as shown in Fig. 31(c). Immediately behind the front and within the two-phase zone, liquid tends to migrate downward because its density is much larger than that of the vapor. The migration, however, occurs at a low speed because of the large resistance against liquid flow in the two-phase zone. Ahead of the front and in the full-liquid region, the liquid ascends owing to thermal buoyancy forces. Away from the steam front, the liquid velocity field becomes horizontal.

Overall assessment of steam displacement for oil recovery or contaminant removal can be made by examining the cumulative mass displaced out of the reservoir; namely,

$$m_{\text{out}} = \frac{1}{A}\int_0^t \int_A (\rho u)_{\text{out}}\, dA\, dt \tag{68}$$

From an experimental point of view, the displaced mass is also a convenient quantity to measure. Numerical results of cumulative displaced mass for three injection rates (shown as circles in Fig. 32) indicate that displaced mass increases almost linearly with time, implying that steam displacement occurs at a constant mean speed. Steam breakthrough is seen to be characterized by a sharp change in the slope of a displacement curve. At times sufficiently later than the steam breakthrough, the slope of the displacement curve should asymptotically approach the injection mass flux because the system has reached steady state. The slopes of the displacement curves, shown in Fig. 32 before steam breakthrough, range between 3.0 and 3.3 times larger than their respective injection mass fluxes, indicating that steam injection is a viable method of removing oil or contaminants from the subsurface. Also plotted in Fig. 32 are the solid lines obtained from 1D simulations in which the gravitational acceleration is set to zero, with other conditions remaining the same. Apparently, 2D displacement can be well approximated by the 1D behavior, regardless of the severe steam override and natural convection present in some of the cases. This might provide a reason why most 1D models give good predictions of the

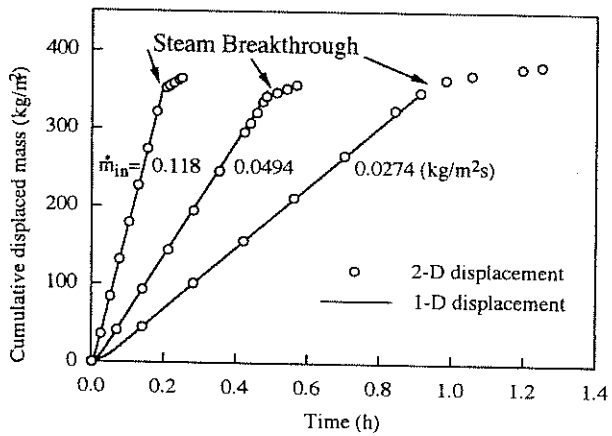

FIG. 32. Cumulative displaced mass for various injection fluxes and comparison to one-dimensional (1D) predictions [48]. 2D, two-dimensional.

performance curves, even though steam override is a complex multidimensional phenomenon.

The thermal dispersion effect on convection in the full-liquid region and, hence, steam displacement can be qualitatively assessed by artificially increasing the effective thermal conductivity. Figure 33 shows that doubling the effective thermal conductivity does not influence the displacement curve, demonstrating that heat conduction into the liquid ahead

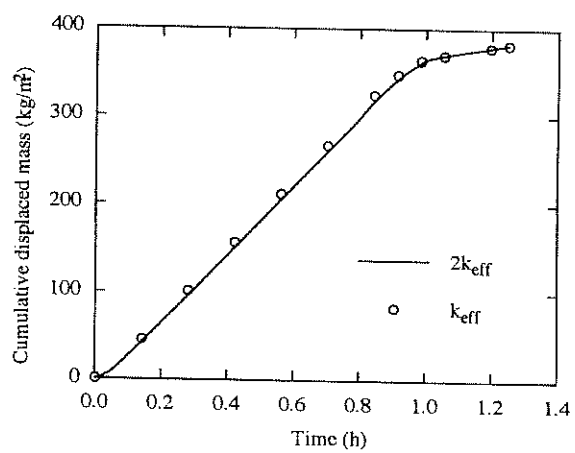

FIG. 33. Effect of thermal dispersion on steam displacement [48].

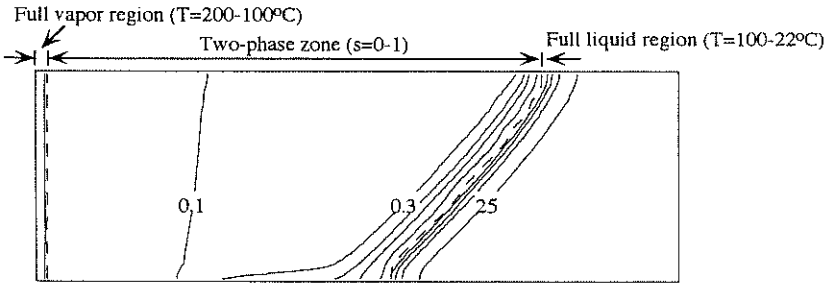

FIG. 34. Numerical results for superheated steam injection with ΔT_{sup} = 100°C, displaying evaporation and condensation front locations, isotherms, and liquid saturation contours (Δs = 0.2). The isotherms in the full vapor region are for T = 200, 150, and 100°C, whereas the isotherms in the full liquid region are in increments of 15°C [48].

of the condensation front plays a negligible role in controlling steam displacement.

Finally, superheated steam injection was studied for a moderate superheat of 100°C. It was found that the superheat helps to displace more liquid out of the porous formation due to the evaporation of residual water as stimulated by the superheated steam. Inspection of the liquid saturation contours shown in Fig. 34 for superheated steam injection indeed reveals that the liquid saturation in a large portion of the two-phase zone becomes lower than the residual value of the water saturation (i.e., 0.2). Figure 34 also illustrates the capability of the present model of handling a three-region problem encompassing superheated vapor, two-phase, and liquid zones, despite the fact that the superheated vapor region is quite narrow due to the small specific heat of the vapor.

G. SUMMARY

This section has presented a review of existing theoretical and experimental work for two-phase, single-component systems in porous media. Considerable progress has been made in the theoretical analysis of these systems in recent years. In particular, with the development of the multiphase mixture model (MMM), numerical solution of multidimensional, two-phase flow, and heat transfer problems in porous media can now be routinely performed on engineering workstations. Several examples reviewed indicate clearly that the computer time using MMM has decreased to a fraction of that required for MFM. The numerical capabilities and advantages of MMM have been fully demonstrated by successful applications to three-region problems including the liquid, two-phase, and super-

heated vapor zones simultaneously [46a, 48]. In addition, the MMM also shed new light on the analytical aspects of two-phase flow and heat transfer in porous media. A number of exact or similarity solutions have been found or expected.

While more applications of MMM to important engineering systems continue, a parallel development of new, accurate, experimental techniques for studying two-phase flow and heat transfer characteristics in porous media cannot be overemphasized. Careful experimentation is required both for gaining a thorough understanding of the two-phase transport phenomena inside porous media and for validating theoretical predictions to be produced. In particular, nonintrusive techniques to measure liquid saturations and phase velocities in the two-phase zone are highly desirable. In addition, the following fundamental issues also require special attention:

- Effects of medium heterogeneity on two-phase flow and heat transfer, and exploitation of heterogeneous materials for dramatic improvement of conventional capillary systems
- A fundamental model describing highly transient, localized, two-phase transport phenomena to be used in the modeling of nucleate and transitional boiling in porous media
- Thermal nonequilibrium models to capture the physics of boiling in porous materials
- Multidimensional solutions of non-Darcian two-phase flows that occur in coarse porous media
- Micro-macroscopic models to rigorously address the couplings between the vapor dynamics on the pore level and two-phase transport phenomena on the system level
- Design of novel thermal devices by taking advantage of two-phase transport principles in porous capillary materials, such as a capillary evaporator

VI. Multiphase, Multicomponent Systems

Multiphase flow and transport in multicomponent systems differ markedly from what was discussed in the preceding section for single-component systems. The fundamental differences arise from the thermodynamics of gas–liquid phase equilibrium of mixtures that allow the gas and liquid phases to be of differing compositions. This is exemplified in Fig. 35 for a typical binary phase diagram. As can be seen, in binary and multicomponent systems the various phases can co-exist in equilibrium

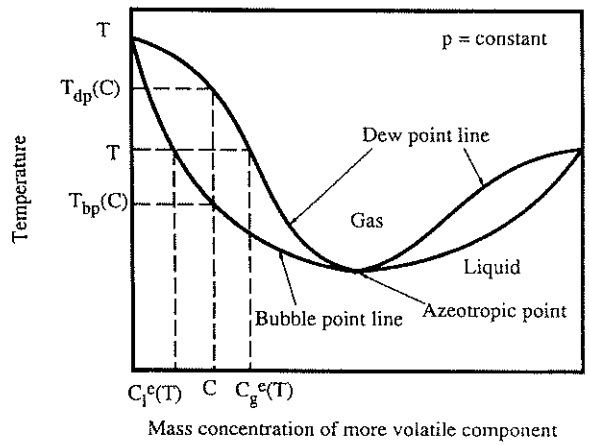

FIG. 35. A typical equilibrium phase diagram for an azeotropic mixture.

over a range of temperatures, thus leading to a nonisothermal multiphase zone. In the case of binary mixtures with a noncondensable gas, Eq. (41) for the equilibrium temperature in a two-phase zone is modified as [124]

$$T = \frac{T_0\left[1 + \dfrac{p_c - yp_g}{h_{fg}\,\rho_l}\right]}{1 - \dfrac{RT_0}{h_{fg}} \ln \dfrac{p_g(1-y)}{p_0}}, \tag{69}$$

where the vapor partial pressure is expressed by $p_g(1-y)$, with y being the molar fraction of the noncondensable gas. It is clear from Eq. (69) that the two-phase temperature strongly varies with the content of the noncondensable gas. Note that in this section the liquid and gas phases are denoted by subscripts l and g, respectively, while the subscript v is reserved for the vapor component in the gas phase.

The second consequence of the phase diagram of mixtures shown in Fig. 35 is that during phase change a chemical species may be preferentially incorporated or released at the interphase boundary because of the differing solubilities in various phases. Thus mass transfer, in addition to heat transfer, plays a critical role in controlling phase change of multicomponent fluids. Moreover, the mass transfer process is often dominant because the rate of mass diffusion is normally much lower than that of heat diffusion in the liquid phase. In addition, the presence of species gradients may cause thermosolutal convection in each fluid phase. The

topic of thermosolutal convection in porous media—although it has received wide attention for single-phase systems over recent years—remains to be explored in multiphase systems. It is well known that thermosolutal convection patterns can be extremely intriguing in situations where the rates of heat and mass diffusion are vastly different.

The strong dependence of interfacial tension on species concentration gives rise to yet another new phenomenon called solutal-capillary flow in multicomponent systems. The capillary forces altered by species concentration (and temperature) variations may either accelerate or retard multiphase flow and transport in porous media.

The objective of this section is to review the significant advances in the understanding of multiphase flow and transport processes in porous media germane to mixtures. Section A explores 1D systems for basic insight into the physical phenomena involved and to establish a basis for further discussion of more complicated configurations arising from practical applications. Section B considers a particular subset of general multiphase systems, that is, liquid–gas systems that are of technical relevance in innumerable applications. Section C presents an overview of the recent efforts toward understanding dynamics of three-phase systems consisting of a gas and two immiscible liquid phases, with particular application to groundwater contamination and remediation. Finally, Section D gives a summary of future research needs in the area of multiphase, multicomponent transport in porous media.

A. One-Dimensional Systems

To delineate the general characteristics of multiphase flow and transport of mixtures in porous media, it is instructive to consider 1D situations in which the governing equations are still represented by Eqs. (42) and (43) but rewritten in terms of the subscripts l and g; that is,

$$\varepsilon \frac{\partial \rho}{\partial t} + \frac{\partial (\rho u)}{\partial x} = 0, \tag{70}$$

$$\varepsilon \frac{\partial (\rho_l s_l)}{\partial t} + \frac{\partial (\rho u \lambda_l)}{\partial x} = \frac{\partial}{\partial x}\left(\rho_l D_c \frac{\partial s_l}{\partial x}\right) - \frac{\partial}{\partial x}\left(\frac{\lambda_l \lambda_g K(\rho_l - \rho_g) g_x}{\nu}\right) + \overline{m}_l. \tag{71}$$

Subject to the appropriate initial and boundary conditions, this equation set can be solved for the mixture velocity u and liquid saturation s_l. Other

secondary variables such as phase velocities and pressures are determined algebraically thereafter.

1. *Steady Multiphase Flows*

As an example of multiphase flows, consider two-phase, two-component flow in a 1D porous medium, as shown in Fig. 3(a). The two components are taken to be air and water, with air being initially present in the porous medium. Thus the liquid phase consists of pure water, whereas the gas phase is binary in water vapor and air. To investigate two-phase flow characteristics in this situation, we can integrate Eqs. (70) and (71) in much the same way as in Part III, Section A.1, except for two notable differences. First, the actual energy used for liquid–vapor phase transformation is now equal to $[q_w - (-k\partial T/\partial x)]$, where the second term accounts for the flux by heat conduction through a nonisothermal two-phase zone. Second, the mixture mass flux across the condensation front $\dot{m}_w$ is no longer zero because the mass transfer of components amounts to a net flow perpendicular to the front. Because the condensation front is impermeable to the noncondensable gas, the mixture mass flux must be given by

$$\dot{m}_w = -\rho_g D \frac{\partial y}{\partial x}, \tag{72}$$

where D is the binary diffusion coefficient of the gas phase. The net mixture flow is to counteract mass diffusion of the noncondensable gas toward the condensation front. Taking these differences into account, Eq. (45) can be modified into the following form for a binary mixture:

$$\rho_l D_c(s) \frac{\partial s_l}{\partial x} - \frac{\lambda_l \lambda_g K(\rho_l - \rho_g) g_x}{\nu} = \frac{1}{h_{fg}}\left(q_w + k \frac{\partial T}{\partial x}\right) - \lambda_l \rho_g D \frac{\partial y}{\partial x}. \tag{73}$$

The last two terms of this equation reflect the effects of heat conduction and mass diffusion on the two-phase characteristics of a binary mixture. The two mechanisms are further interlinked via Eq. (69), which relates the two-phase temperature to the molar fraction of the noncondensable gas. Figure 36 compares the liquid saturation profiles predicted by Eq. (73) for cases with and without a noncondensable gas [124]. The curve for the condensation front temperature equal to 100°C corresponds to the absence of noncondensable gas at atmospheric pressure, whereas the cases denoted by lower temperatures indicate increasingly higher contents of the noncondensable gas. It is seen that the liquid saturation gradients decrease as the

topic of thermosolutal convection in porous media—although it has received wide attention for single-phase systems over recent years—remains to be explored in multiphase systems. It is well known that thermosolutal convection patterns can be extremely intriguing in situations where the rates of heat and mass diffusion are vastly different.

The strong dependence of interfacial tension on species concentration gives rise to yet another new phenomenon called solutal-capillary flow in multicomponent systems. The capillary forces altered by species concentration (and temperature) variations may either accelerate or retard multiphase flow and transport in porous media.

The objective of this section is to review the significant advances in the understanding of multiphase flow and transport processes in porous media germane to mixtures. Section A explores 1D systems for basic insight into the physical phenomena involved and to establish a basis for further discussion of more complicated configurations arising from practical applications. Section B considers a particular subset of general multiphase systems, that is, liquid–gas systems that are of technical relevance in innumerable applications. Section C presents an overview of the recent efforts toward understanding dynamics of three-phase systems consisting of a gas and two immiscible liquid phases, with particular application to groundwater contamination and remediation. Finally, Section D gives a summary of future research needs in the area of multiphase, multicomponent transport in porous media.

A. One-Dimensional Systems

To delineate the general characteristics of multiphase flow and transport of mixtures in porous media, it is instructive to consider 1D situations in which the governing equations are still represented by Eqs. (42) and (43) but rewritten in terms of the subscripts l and g; that is,

$$\varepsilon \frac{\partial \rho}{\partial t} + \frac{\partial (\rho u)}{\partial x} = 0, \tag{70}$$

$$\varepsilon \frac{\partial (\rho_l s_l)}{\partial t} + \frac{\partial (\rho u \lambda_l)}{\partial x} = \frac{\partial}{\partial x}\left(\rho_l D_c \frac{\partial s_l}{\partial x}\right) - \frac{\partial}{\partial x}\left(\frac{\lambda_l \lambda_g K(\rho_l - \rho_g) g_x}{\nu}\right) + \bar{m}_l. \tag{71}$$

Subject to the appropriate initial and boundary conditions, this equation set can be solved for the mixture velocity u and liquid saturation s_l. Other secondary variables such as phase velocities and pressures are determined algebraically thereafter.

1. *Steady Multiphase Flows*

As an example of multiphase flows, consider two-phase, two-component flow in a 1D porous medium, as shown in Fig. 3(a). The two components are taken to be air and water, with air being initially present in the porous medium. Thus the liquid phase consists of pure water, whereas the gas phase is binary in water vapor and air. To investigate two-phase flow characteristics in this situation, we can integrate Eqs. (70) and (71) in much the same way as in Part III, Section A.1, except for two notable differences. First, the actual energy used for liquid–vapor phase transformation is now equal to $[q_w - (-k\partial T/\partial x)]$, where the second term accounts for the flux by heat conduction through a nonisothermal two-phase zone. Second, the mixture mass flux across the condensation front $\dot{m}_w$ is no longer zero because the mass transfer of components amounts to a net flow perpendicular to the front. Because the condensation front is impermeable to the noncondensable gas, the mixture mass flux must be given by

$$\dot{m}_w = -\rho_g D \frac{\partial y}{\partial x}, \tag{72}$$

where D is the binary diffusion coefficient of the gas phase. The net mixture flow is to counteract mass diffusion of the noncondensable gas toward the condensation front. Taking these differences into account, Eq. (45) can be modified into the following form for a binary mixture:

$$\rho_l D_c(s) \frac{\partial s_l}{\partial x} - \frac{\lambda_l \lambda_g K(\rho_l - \rho_g) g_x}{\nu} = \frac{1}{h_{fg}}\left(q_w + k \frac{\partial T}{\partial x}\right) - \lambda_l \rho_g D \frac{\partial y}{\partial x}. \tag{73}$$

The last two terms of this equation reflect the effects of heat conduction and mass diffusion on the two-phase characteristics of a binary mixture. The two mechanisms are further interlinked via Eq. (69), which relates the two-phase temperature to the molar fraction of the noncondensable gas. Figure 36 compares the liquid saturation profiles predicted by Eq. (73) for cases with and without a noncondensable gas [124]. The curve for the condensation front temperature equal to 100°C corresponds to the absence of noncondensable gas at atmospheric pressure, whereas the cases denoted by lower temperatures indicate increasingly higher contents of the noncondensable gas. It is seen that the liquid saturation gradients decrease as the

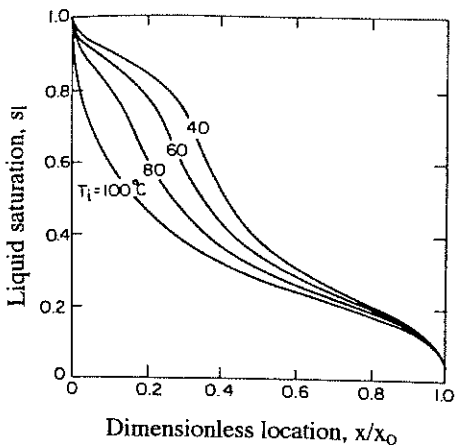

FIG. 36. Effects of a noncondensable gas on a two-phase flow pattern [124].

concentration of the noncondensable gas increases. The smaller saturation gradients, in turn, increase the wicking limit of heat transfer [124].

2. *Transient Multiphase, Multicomponent Flows*

Under transient conditions and ignoring the interphase mass transfer $\overline{m}_l$, Eqs. (70) and (71) may admit two possible similarity solutions, depending on particular types of boundary conditions. One corresponds to constant mixture velocity at the boundaries of a multiphase zone. In this situation, a similarity transformation $\eta = x - v_c t$ can be derived from Eqs. (70) and (71), where v_c represents the constant characteristic velocity of the moving boundary. Examples of this family of exact solutions include constant rate injection of steam into porous media. Yuan and Udell [125] studied steam distillation of a single component hydrocarbon liquid in a 1D porous media, both theoretically and experimentally. Assuming a constant injection rate of the steam with constant quality, the previously mentioned similarity solution was obtained, and the characteristic velocity of the distillation front was found to be a function of the residual saturation of the hydrocarbon liquid as well as the thermodynamic properties of water and the hydrocarbon liquid. Experimental results confirmed this similarity theory and, furthermore, determined that the interphase mass transfer coefficient (a parameter gauging the departure from local chemical nonequilibrium) increases linearly with the saturation of the liquid hydrocarbon [125].

The other family of similarity solutions that can be foreseen from Eqs. (70) and (71) assumes the negligible gravity effect and the boundary velocity of the mixture to follow the $t^{-1/2}$ profile. Then the similarity transformation $\eta = x/\sqrt{t}$ exists. This type of solution is applicable to situations such as constant pressure injection (the relationship $u \sim x^{-1} \sim t^{-1/2}$ is evident from the Darcy equation) and drying of porous slabs. Within this family, Morrison [76] obtained an analytical solution for a two-phase binary system under the assumption of negligible capillary pressure; however, this assumption is unnecessary in light of MMM, as has been explained earlier in Section II.

B. Liquid–Gas Systems

Liquid–gas multicomponent systems represent an important subset of general multiphase, multicomponent systems, and arise in a wide variety of applications in thermal, chemical, and environmental engineering.

1. *Convection in Unsaturated Media*

The topic of convection in unsaturated porous media, with and without evaporation or condensation, was systematically discussed by Plumb [126], who also concluded that very little work has been done on convection in the vadose zone of the subsurface. Technological examples where this subject may be important include heat losses from underground thermal structures, ground coupled heat pumps, repositories of high-level radioactive waste, and trickled-bed chemical reactors. Plumb [127] considered convection in a parallel flow from a heated horizontal surface embedded in the vadose zone. Assuming the Richards approximation in UFT (i.e., neglecting the gas phase motion), Plumb [127] obtained a boundary layer solution to the convective heat transfer problem. The interrelation between heat transfer and capillary-driven flow was shown. The analytical solution, however, has not been verified experimentally. In view of the similarities between UFT and MMM discussed in Section II, it appears possible and straightforward to remove the Richards assumption from the Plumb analysis, and to carry out a more accurate analysis of convection in unsaturated porous media using MMM.

Recent application to repositories of high-level radioactive waste has prompted renewed research interest in convection in unsaturated media. A large amount of decay heat is expected to be generated as a result of placing spent nuclear fuel in a potential repository site. Understanding the resulting thermal–hydrological scenarios is essential for repository assess-

ment. Pollock [128] employed a 1D mathematical model of the coupled heat and mass transfer to analyze vertical transport of energy and moisture above and below a horizontal repository. However, the 1D model is inherently incapable of describing the thermally induced gas circulation around a repository. Most recently, Chen and Boehm [129] presented an overview of heat transfer around an underground storage of high-level radioactive waste, and pointed out the need for careful experimentation in order to calibrate various existing models. Several experiments were carried out to measure the temperature distribution throughout an unsaturated packed bed. It was found that water vapor generated in the vicinity of the heater could be advected over a large portion of the bed, thus significantly altering the entire temperature field. Conduction was identified as a principal mechanism for heat transfer around the heater; however, convection and two-phase transport combined to contribute to heat transfer far away from the heater.

Another potential application of convection in liquid–gas systems concerns trickled-bed chemical reactors featuring liquid–gas co-current and countercurrent flows in packed beds [5]. Heat transfer in such two-phase systems is crucially important for reactor design, especially when higher exothermic reactions such as hydrogenation and oxidation take place. There appears to be only a few articles in the literature on the thermal aspects of trickle bed reactors. Weekman and Myers [130] measured radial temperature profiles in a co-current air–water downward flow through a packed column. Three types of packings with beads of 3.8 to 6.5 mm in diameter were examined. The experimental data was then interpreted by a simple heat transfer model for the two-phase mixture with the effective thermal conductivity being an adjustable parameter. Specchia and Baldi [131] interpreted similar experiments but employed a two-parameter heat transfer model (i.e., the effective thermal conductivity and the wall-to-bed heat transfer coefficient are adjustable). These authors proposed correlations of both parameters as functions of the operating conditions. It should be mentioned that all these primitive models have ignored the complicated two-phase flow patterns in trickled beds. Crine [132] took an important step toward establishing the effects of the two-phase distribution on the heat transfer phenomena using a percolation theory. However, much more research, both experimental and theoretical, is left to unravel the coupling between heat transfer and two-phase hydrodynamics in packed beds.

2. *Drying of Porous Materials*

Within the general area of multiphase, multicomponent heat and mass transfer in porous media, the problem of drying has probably received the most research attention. Classic work includes Krischer [33], Luikov [134], Whitaker [4], and Eckert and Faghri [135]. Recent literature of drying was reviewed by Plumb [136] and Bories [137]. Additional references were cited in a general review on porous media transport by Tien and Vafai [13].

Without attempting an exhaustive review on drying, suffice it to mention the pioneering work of Luikov [134] and Whitaker [4]. These models constitute the theoretical basis of a large body of previous work. Luikov's model assumed that moisture transfer in a porous material is driven by gradients of moisture content, temperature, and pressure in a diffusion-like fashion. Whitaker [4] developed a comprehensive theory of drying using the technique of volume averaging. In a later study, Whitaker [138] specifically demonstrated that for low-intensity drying conditions the liquid transport is only due to capillary action and the governing transport equation can be written in terms of the liquid saturation:

$$\varepsilon \frac{\partial(\rho_l s_l)}{\partial t} = \frac{\partial}{\partial x}\left(D \frac{\partial s_l}{\partial x}\right) + \frac{\partial}{\partial x}\left(K \frac{k_{rl}}{\nu_l} \rho_l g\right), \tag{74}$$

where D is given by

$$D = \frac{K k_{rl}}{\nu_l} \frac{dp_c}{ds_l}. \tag{75}$$

A comparison with Eq. (15) shows that Eq. (74) is exactly the duplicate of UFT for problems of drying. Thus implicit in Eq. (74) is the assumption that the gas phase pressure remains constant. This assumption has been commonly invoked, both implicitly and explicitly, in the majority of current drying models. Apparently, the assumption is likely to break down for rapid drying processes where the gas phase dynamics become critical. As a significant departure from previous reviews on drying, the following discussion concentrates on systems in which simultaneous liquid and gas flows take place.

Consider a porous medium initially saturated or near-saturated with liquid. When drying occurs by passing heated air or vapor over the surface of the porous material, as illustrated in Fig. 37, three distinct regions may appear inside the porous medium. Near to the drying surface, a superheated vapor region results due to high drying rates. Adjacent to this region and extending into the porous material will be a two-phase zone in which the two-phase flow and transport is driven by both gravitational and capillary forces. Ahead of this zone the medium will remain saturated with liquid. The temperature profile in each region is also sketched in Fig. 37.

In 1D situations, an exact similarity solution can be developed for the problem. This was first shown by Udell [139] for the case of superheated steam drying of a semi-infinite slab initially saturated with liquid water. Analytical profiles of temperature and liquid saturation were found using

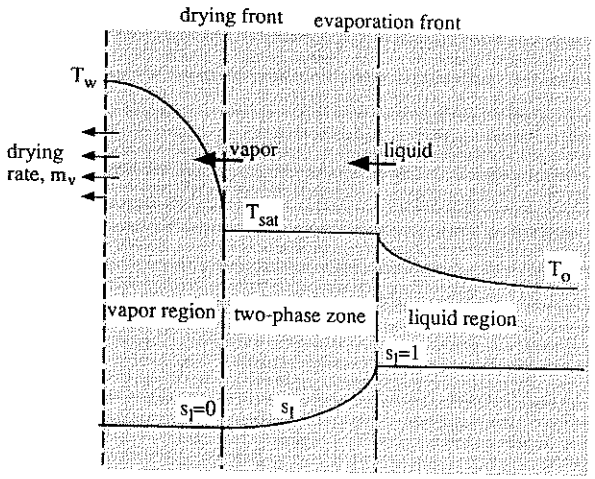

FIG. 37. Schematic illustration of drying of porous material and the different drying regimes.

the similarity transformation $x/\sqrt{t}$, as predicted in Part IV, Section A.2. While accounting fully for the two-phase simultaneous flows, however, Udell did make a quasi-steady assumption, namely that the two-phase dynamics is steady within the moving coordinate attached to the evaporation front. While this assumption was instrumental in Udell [139] arriving at the similarity solution based on MFM, it appears unnecessary within the framework of MMM. To elaborate on this, we can apply the energy equation of MMM, Eq. (35), to the current 1D problem; that is,

$$\frac{\partial}{\partial t}[(1-\varepsilon)\rho_s h_s + \varepsilon\rho h] + \frac{\partial}{\partial x}(\gamma_h \rho u h) = \frac{\partial}{\partial x}\left(k_g \frac{\partial T}{\partial x}\right) + \frac{\partial}{\partial x}\left(-h_{fg}\rho_l D_c \frac{\partial s_l}{\partial x}\right). \quad (76)$$

This equation, together with Eq. (70), then constitutes a complete mathematical system for two unknowns: the mixture enthalpy h and velocity u. The mixture enthalpy in a single-phase region is nothing more than the temperature T times a specific heat, whereas in the two-phase zone the temperature corresponds to the known saturation state, and thus the enthalpy h is linearly proportional to the liquid saturation s_l. Equations (70) and (76) admit a similarity solution provided that the boundary

conditions are as follows:

$$\text{at } t = 0, \quad h = c_l T_0 = \text{const}, \quad u = 0, \quad (77)$$

$$\text{at } x = 0, \quad h = h_{fg} + c_{l} T_w = \text{const}, \quad (78)$$

$$\text{at } x \to \infty, \quad h = c_l T_0 = \text{const}, \quad u = 0. \quad (79)$$

With a similarity transformation $\eta = x/\sqrt{t}$, Eqs. (70) and (76) are readily cast into two ordinary differential equations, which can then be solved using routine numerical methods such as the Runge-Kutta scheme. Results of this analytical study will be detailed in a forthcoming publication. Note that no quasi-steady assumption needs to be employed, and thus the exact nature of the solution is retained. Such more exact solutions will be useful in providing physical insight into the drying process as well as a benchmark to validate sophisticated numerical models. For instance, as revealed in Part IV, Section A.2, the similarity solution indicates that the drying rate, that is, the mixture velocity at the drying surface, is inversely proportional to the square root of time.

For drying samples of finite dimension, numerical methods are usually required. An example was given by Rogers and Kaviany [140] who experimentally and numerically studied drying of an initially partially saturated packed bed during both funicular and drying-front periods. In the funicular regime, the liquid phase is continuous, and simultaneous two-phase flow occurs. In the second period, the liquid saturation at the drying surface drops below the irreducible value, and a superheated gas region begins to develop at the surface and to expand into the porous medium. Rogers and Kaviany [140] used MFM to simulate the funicular drying process, but had to terminate the numerical simulation when the drying front regime was reached. This numerical difficulty arises from the inherent nature of MFM; that is, MFM is inconvenient to handle a multiregion problem encompassing single- and two-phase subregions simultaneously or a problem involving phase appearance and disappearance. Figure 38 shows the predicted and measured mass transfer rates as a function of time [140]. As seen, the drying rate decreases initially, and then remains constant, signifying that the surface lies within a two-phase zone. The mass transfer rate drastically decreases when reaching the drying front regime (called the evaporative front in the original article and Fig. 38), where the surface becomes completely dry. The numerical prediction in the funicular regime compared favorably with the experimental data.

While it still may be possible to use MFM and track a moving front separating various regions for 1D drying problems, significantly more difficulties will be experienced in multidimensional problems. The numerical problem of interface tracking and various remedial methods have been

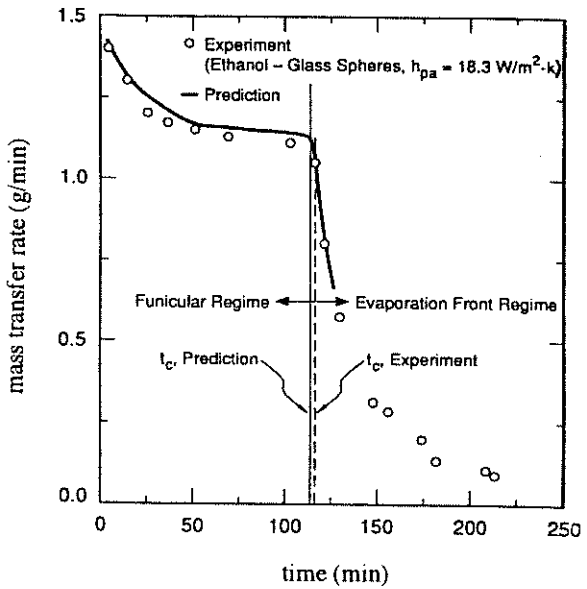

FIG. 38. Variation of the drying rate with respect to time in both the funicular and drying front regimes [140].

discussed in the work of Perre *et al.* [141, 142] on 2D drying. Unfortunately, all of these methods require certain approximations. On the other hand, if MMM is used, the numerical difficulty would vanish, making it possible to develop a general-purpose drying simulation code. Such a multidimensional code would be particularly useful to analyze and understand the drying process of anisotropic materials, as studied by Ouelhazi *et al.* [143].

Well-controlled and carefully defined experimental studies are scarce in the literature. Lee *et al.* [144] conducted an experiment in an attempt to provide a database for drying packed beds of granular nonhygroscopic materials. Experimental results for drying rate, saturation distribution, temperature distribution, and surface saturation were reported for drying glass beads under various drying conditions. Their results revealed that, contrary to available model predictions, porous materials do not necessarily exhibit saturation gradients that always increase with distance from the drying surface. Under certain conditions, the capillary action may be sufficient to create an internal drying front. The data of Lee *et al.* [144] can be used to validate drying models applicable to different materials and drying scenarios.

3. *Boiling of Multicomponent Liquids*

Boiling of multicomponent liquids in porous materials is a topic closely related to many two-phase thermal devices such as heat pipes, capillary pumped loops, and porous media heat exchangers. In the past, these systems employed mostly single-component working fluids. However, it seems worthy of exploring a binary or multicomponent mixture as the working fluid in order to leapfrog the current thermal technologies for meeting future needs of higher heat load systems. This is based on several well-known attributes of binary mixture boiling without porous media:

1. Increase in critical heat fluxes
2. Creation of a passive control mechanism for device operation
3. Substantial decrease in the temperature overshoot typically associated with single-component liquid boiling.

Earlier studies on pool boiling of binary mixtures observed that the critical heat fluxes for water–alcohol mixtures at low alcohol concentrations were much higher than the corresponding values for pure water under comparable conditions [145]. Recently, Peterson *et al.* [146] reported that by using a binary mixture, the system pressure of a reflux thermosyphon can remain virtually constant with varying power input, thus achieving desirable passive control for sustainable device operation. This mechanism of passive control can be explained by the phase diagram of a binary mixture that requires evaporation to occur over a range of temperatures at a constant pressure. Normington *et al.* [147] performed extensive experiments to demonstrate that the use of mixtures of dielectric liquids can reduce or eliminate the temperature overshoot that occurs during boiling at high heat fluxes.

These unique features of binary mixture pool boiling can be extended to capillary systems. In addition, and perhaps more important, there exist particular merits of using binary mixtures in capillary structures. For instance, the addition of a more volatile component generates a larger amount of vapor in a porous wick, thus lowering the average liquid saturation and, hence, increasing the capillary pressure for feeding liquid into the system. This is because the capillary pressure increases markedly as the liquid saturation decreases (see Fig. 1). The augmented wicking effect may extend the capillary pumping limit substantially and increase the dryout heat flux of wicks. Another beneficial effect of binary mixtures is to improve the start-up transients during which vapor bubbles of the more-volatile component are first generated and serve as the "seeding vapor" to induce capillary forces.

The only work on boiling in porous wicks saturated with a binary fluid was performed by Pruzan *et al.* [148], who demonstrated that the maximum

heat flux with water–ethanol mixtures is 2.35 times larger than that for pure water. To date, these test data have not been supported and analyzed through corresponding fundamental studies, and none of the above-mentioned features of binary mixture boiling in porous structures has been explored.

4. *Nonaqueous Phase Liquids–Air Flow and Transport in the Unsaturated Zone*

In the category of liquid–gas systems, another important class of problems is concerned with groundwater contamination and remediation. Recently, groundwater contamination by nonaqueous phase liquids (NAPLs) such as hydrocarbon fuels and halogenated organic solvents has become a major environmental concern and, hence, has received intense research attention [149].

Figure 39 depicts a typical scenario of NAPL contamination. In the unsaturated zone near the ground surface, an organic liquid spilled from a leaky storage tank may migrate downward due to gravitational forces. Concurrently, the chemical volatilizes into the air in the pores, and the organic vapor advects laterally in the unsaturated zone, thereby greatly increasing the area of contamination. When the NAPL reaches a low-

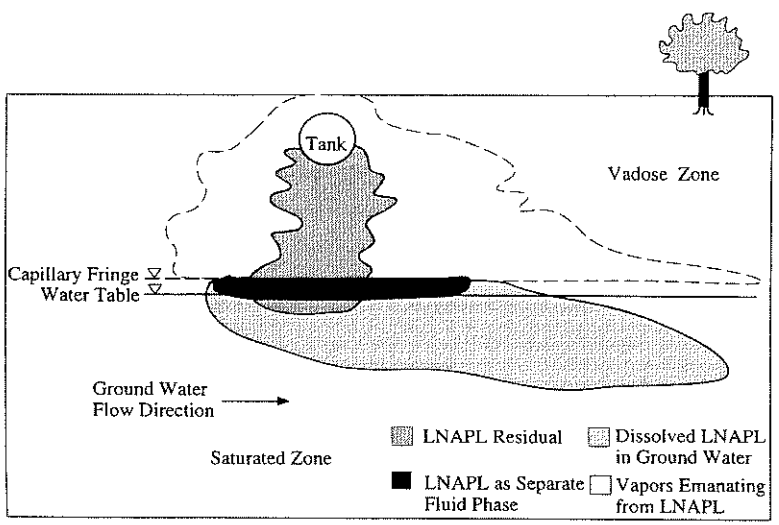

FIG. 39. Schematic illustration of LNAPL (lighter than water nonaqueous phase liquids) infiltration and redistribution in the vadose zone (after [149]).

permeability barrier or the saturated zone (in the case of a lighter than water NAPL), it spreads laterally, forming a pool or lens floating over the barrier or the water table. Clearly the most important NAPL contamination mechanisms in the unsaturated zone include NAPL transport as a separate phase and organic vapor transport via gas phase advection. The contaminant volatilized into the air in the soil pores may subsequently be dissolved into flowing groundwater or infiltrating recharge water, thereby contributing to contamination of the underlying groundwater. Modeling of these strongly coupled transport processes will ultimately determine the contaminant fate in the subsurface and subsequently define the task of locating and removing contaminants. A currently popular remediation technology involves injecting clean air into the contaminated site to recover contaminants. This method called soil vapor extraction (SVE) proves very effective for removing volatile organic compounds, which have high vapor pressures and large Henry constants at the ambient surface temperature. For semivolatile or low-volatile compounds, however, a thermally enhanced SVE would be necessary that injects heated air (instead of cold air) into the contaminated site to increase the subsurface temperature, thereby enhancing volatilization of contaminants and accelerating the rate of remediation.

To date, a good understanding and control of contaminant transport during thermal venting is absent. While the traditional soil vapor extraction has been studied both experimentally [150] and numerically [151], very little research has been performed for thermally enhanced SVE. Lingineni and Dhir [152] conducted 1D experiments of thermally enhanced SVE in a homogeneous sand column filled with gasoline at residual saturation. They also developed a nonisothermal mass transport model only for the gas phase. Figure 40 shows a favorable agreement between their experimental and numerical temperature profiles for normal and thermal venting, respectively, at an air flow rate of 234 L/min. It is also seen that temperature decreases occur due to evaporation of the contaminant in both normal (Fig. 40(a)) and thermal venting (Fig. 40(b)) cases. Moreover, the temperature decrease in the normal venting case is more severe than in that with thermal venting, because there is no external heat source in the former case to compensate for the latent heat of vaporization. Lingineni and Dhir [152] concluded that the effect of thermal energy on remediation of less-volatile contaminants is substantial, whereas the effect on high-volatile contaminants is minimal. In another recent study, Kaluarachchi and Islam [153] developed a nonisothermal model to describe gas flow, energy transport, and multicomponent mass transport and applied it to both 1D and 2D situations. The 1D results were favorably compared with the experimental data of Lingineni and Dhir [152], and hypothetical 2D

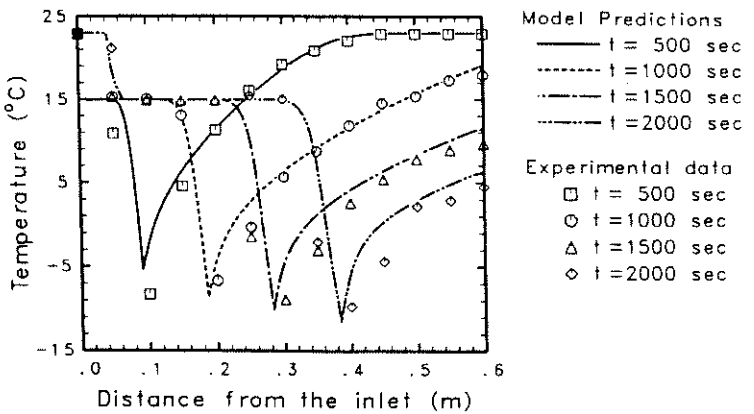

(a) normal venting

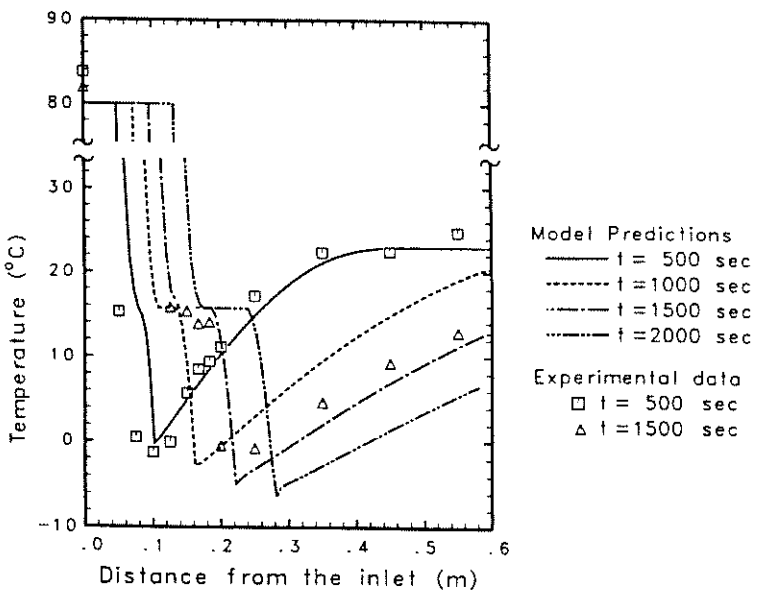

(b) thermal venting

FIG. 40. Comparison between the predicted and measured temperatures in a soil column for: (a) normal venting, and (b) thermal venting [152].

simulations provided considerable insight into thermally enhanced SVE for subsurface remediation. However, both studies have considered the gas phase flow only, and thus their applicability is limited to the vadose zone with immobile water and NAPL phases.

In an attempt to understand the SVE processes in cases of mobile NAPL, Cheng and Wang [47] considered infiltration and redistribution of a NAPL in a 2D homogeneous sand aquifer. The NAPL was introduced into the system through a small opening along the left boundary, which models a contaminant source resulting from a leaky underground tank. A constant NAPL saturation was assumed to prevail inside this region during the entire infiltration process. The aquifer initially contained air and water, while the water saturation was assumed to be uniform and at a residual value. In this numerical study, the water phase was excluded from the system for simplicity, because it is practically immobile ($k_{rw} = 0$) during the NAPL transport; the problem was thus reduced to a two-phase (i.e., gas and NAPL), binary mixture system. As a first approximation, an isothermal system was also assumed.

Cheng and Wang's numerical study [47] was based on MMM, which fully accounts for the strong interactions between the two phases through the evaporation of the organic liquid into the gas phase. In the two-phase zone, the two-phase flow is driven by both capillary and gravitational forces, whereas in the pure gas phase region, the gas flow may be induced by the buoyancy forces due to concentration gradients. This solutal convection is important for the transport of chemical compounds through the gas phase. The vapor phase transport also represents a key mechanism for SVE. The rectangular domain shown in Figs. 41 to 43 was divided into a uniform 82 × 32 grid. The choice of this fine grid size was made possible due to the high computational efficiency of MMM. A typical transient simulation required only 2.7 hours of computation on a Hewlett Parkard 715/75 workstation. Such CPU time is on the same order of magnitude as for a single-phase problem with similar complexities [47]. Sample calculations were performed for three common contaminants: carbon tetrachloride (CCl_4), toluene, and trichloroethylene (TCE). Carbon tetrachloride is dense and more volatile, so that the resulting two-phase flow and gas phase advection are strong. Toluene represents an opposite case because its density is relatively low and its volatilization also is to a lesser extent. As an intermediate case, TCE is heavier and more volatile than is toluene, but is lighter and less volatile than CCl_4.

Figure 41 shows the composite plots of NAPL saturation distributions in the two-phase zone and contours of constant air concentration in the pure gas phase region at 3, 6, and 12 hours after the spill of CCl_4. The mass concentration of the organic vapor in the gas phase can be read from Fig.

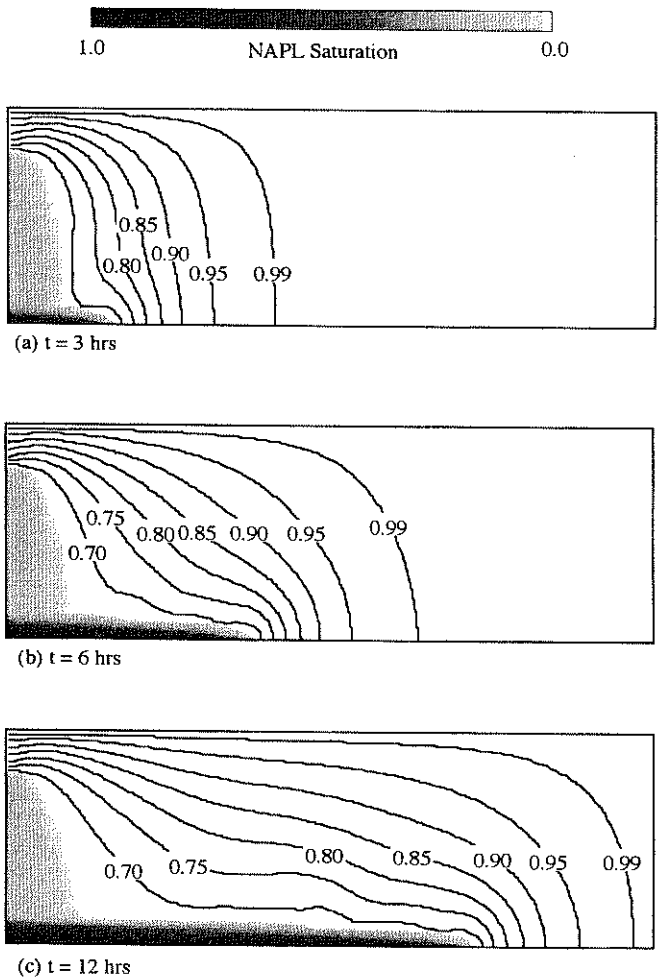

FIG. 41. Composite plots of carbon tetrachloride (CCl_4) saturation in the two-phase zone and air concentration in the gas phase for CCl_4, where $(1 - C_g)$ represents the organic vapor concentration [47]. NAPL, nonaqueous phase liquids.

41 using the conversion relation $C_v = (1 - C_g)$. Thus the 0.99 contours shown in Fig. 41 denote 1% of organic vapor present in the gas phase, a threshold value to define the contaminant front. The phase interface, which separates the two-phase zone from the all gas region, is also the evaporation front at which the air concentration is constant and equal to

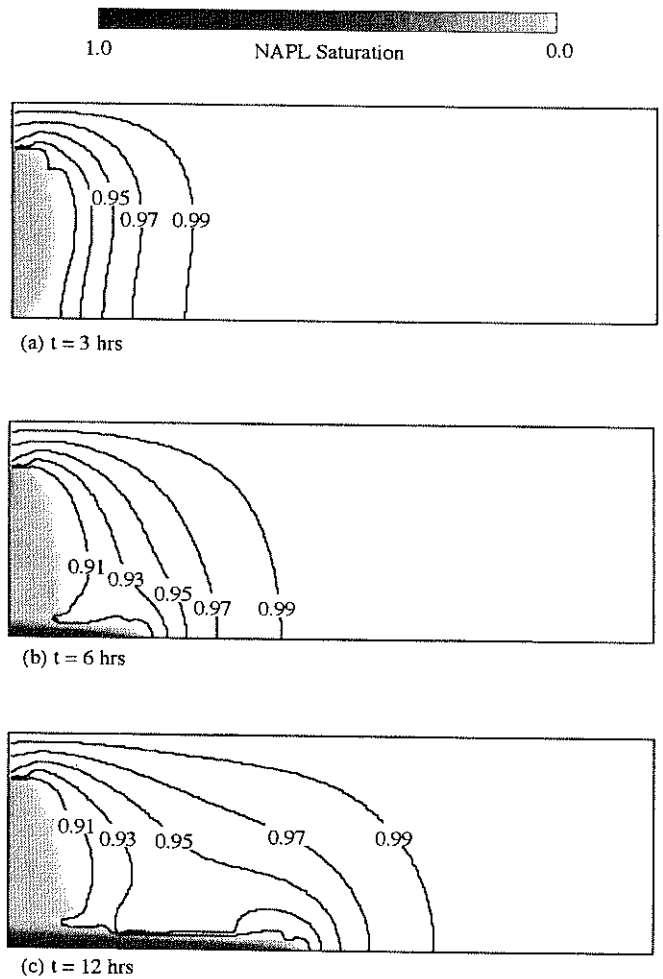

FIG. 42. Composite plots of toluene saturation in the two-phase zone and air concentration in the gas phase for toluene, where $(1 - C_g)$ represents the organic vapor concentration [47]. NAPL, nonaqueous phase liquids.

its equilibrium value (i.e., 0.513 in the case of CCl_4 at the ambient temperature).

At the very initial stages of NAPL invasion, a two-phase semicircular zone develops that covers the spill spot. This is expected because the initial infiltration is governed principally by isotropic capillary diffusion. At 3 h

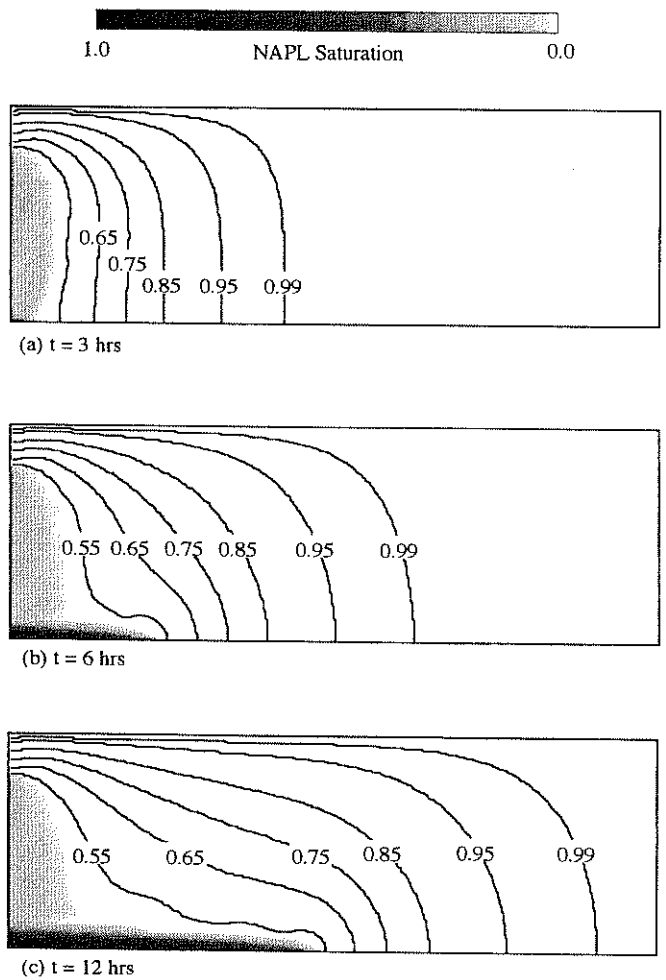

FIG. 43. Composite plots of trichloroethylene (TCE) saturation in the two-phase zone and air concentration in the gas phase for TCE, where $(1 - C_g)$ represents the organic vapor concentration [47]. NAPL, nonaqueous phase liquids.

after the spill (Fig. 41a), the NAPL infiltration front reaches the bottom water table. The gravitational forces due to the disparate density difference between the NAPL and gas has dominantly controlled the two-phase flow, resulting in preferential spreading in the vertical direction rather than in the lateral direction. This predicted shape of the NAPL infiltration front is reminiscent of those observed experimentally by Schwille [154] for

a dense NAPL, and by Pantanzidou and Sitar [155] and Geel and Sykes [156] for light NAPLs in the unsaturated zone. The gas phase advection induced by concentration gradients spreads the volatilized organic vapor far beyond the NAPL infiltration front (Fig. 41(a)). The contaminant front denoted by the 1% contour in the organic vapor concentration is seen to penetrate deeply into the aquifer away from the contaminant source. It should be noted that several single-phase studies [157, 158] also indicated the wide spreading of the organic vapor by solutally induced convection. However, in the conjugate single- and two-phase flow system, the displacement flow in the gas phase caused by the propagation of the phase interface overrides the density-driven flow [47]. This indicates a need for the consideration of NAPL movement in modeling gas flow and quantifying the vapor phase transport for remedial operations such as SVE.

At 6 h after the spill, the phase interface motion is characterized by the horizontal migration of the NAPL along the impermeable bottom. A NAPL lens is seen to float over the impermeable barrier (Fig. 41(b)). Greater lateral spreading occurs as a result of diminishing vertical movement of the NAPL and increasingly dominant capillary forces at the leading edge of the NAPL infiltration front. The volatilized vapor is spread farthest at the bottom because of combined density-driven downward flow and outward flow caused by the displacement of the infiltrating NAPL (Fig. 41(b)). By 12 h the zone of contamination has become so extensive that the contaminant front almost reaches the right boundary, which models an infinite boundary (Fig. 41(c)). It is also shown that the NAPL lens at the bottom of the aquifer becomes elongated and pancake-shaped, and higher NAPL saturations are found inside the lens because the NAPL is continually fed from the vertical infiltration. These predicted features are again in good agreement with the experimental observations by Pantanzidou and Sitar [155]. The NAPL saturation inside the lens can be significantly higher than that of the contaminant source due to the gravity-induced phase separation. The thickness of the NAPL lens depend on the equilibrium between the gravitational and capillary forces; therefore, the thin lens predicted implies that the gravitational forces override the capillary forces in the system under consideration.

Toluene has a lower density than does CCl_4, and therefore a lesser amount of the NAPL entering the subsurface is expected for the same saturation of the contaminant source. However, toluene is also less volatile, so that the amount of the chemical evaporated into the air in the soil pores decreases. The net effect of these counter factors results in a two-phase zone of almost the same extent, as shown in Fig. 42. Nonetheless, the all gas phase region contaminated by the organic vapor is minimal because of the low volatility of toluene. Therefore, the whole zone contaminated by

toluene is less extensive as compared with CCl_4, provided all other conditions are maintained the same. The air concentration isopleths in Fig. 42(c) indicate that the organic vapor concentrations are high near the water table. The gas of high organic vapor content combined with the direct dissolution of the NAPL lens into the water phase may cause serious contamination of the groundwater system underlying the water table.

Trichloroethylene is as dense as CCl_4, but less volatile. Moreover, TCE has an interfacial tension similar to CCl_4. Because the NAPL infiltration rate into the subsurface is determined mainly by the density difference between the phases and the interfacial tension, the rates for TCE and CCl_4 are expected to be about the same. The two chemicals differ only in volatility, which leads to a smaller two-phase zone in the case of CCl_4. This is indeed the case, as can be seen by comparing Fig. 43 with Fig. 41. However, the gas phase region contaminated by chemical vapor is less extensive for TCE than it is for CCl_4. Therefore, the whole zone of contamination remains almost the same for both TCE and CCl_4.

It is of practical interest to visualize all stages of groundwater contamination and remediation processes, starting from the NAPL spill, to the redistribution after the contaminant source is removed, and finally to the NAPL removal from the subsurface. MMM promises to provide a tool for such computationally intensive simulations [159]. Some illustrative results are presented below for a hypothetical 2D aquifer contaminated by CCl_4, as described earlier. The first phase of this simulation consisted of predicting the NAPL infiltration event for 3 h as described above. During the second phase, the leaking contaminant source was removed and the NAPL was allowed to redistribute in the aquifer due to gravity gradients and capillary forces. The last phase of the simulation considered a SVE remedial action by injecting clean air from a fully penetrated well along the right boundary. Figure 44 (in color section) presents selected results of the entire simulation, which include the NAPL saturation distribution (the color images), the iso-concentration contours in the gas phase (the color lines), and the gas phase velocity vectors (white arrows).

Figure 44(a) displays the composite plots at 3 h after the spill. The NAPL is seen to reach the impermeable bottom. At the same time, the organic vapor emanating from the NAPL-gas two-phase zone has widely spread into the aquifer due to a displacement flow in the gas phase caused by the infiltrating NAPL. It should be pointed out that in this figure the velocity scale has been chosen small enough to show the details of the velocity field in the all-gas region while omitting some large velocity vectors in the two-phase zone. It can be seen that the displacement stems mainly from the vicinity of the contaminant source at the left boundary as well as the leading infiltration front along the bottom impermeable boundary; both locations are characterized by rapid infiltration of the NAPL and hence significant displacement of the gas. The displaced gas exit through the permeable ground surface.

The plots displayed in Fig. 44(b) show the NAPL redistribution process after the contaminant source is removed. At 9 h of redistribution, the NAPL is seen to accumulate at the bottom because of the NAPL being much heavier than the gas. The maximum NAPL saturation is found therein, which may greatly endanger the underlying groundwater system. The NAPL saturation in the area adjacent to the original contaminant source is, however, decreasing so as to maintain the mass balance in the system. The gas phase in most of the aquifer has been contaminated by the organic vapor volatilized from the two-phase zone. Fast spreading of the contaminant is partly due to rapid infiltration of the NAPL along the bottom, and partly due to the displacement of the gas phase by the infiltrating NAPL.

Figure 44(c) displays results of the SVE process in which clean air is injected uniformly along the right boundary (i.e., the injection well) and the organic vapor is recovered through a production well sitting along the left boundary. Both injection and production wells were fully screened to the bottom of the aquifer. The ground surface is now covered to prevent the organic vapor from escaping to the atmosphere. The air velocity blown into the aquifer is 0.36 m/h. Comparing Fig. 44(b) and 44(c), it can be seen that the two-phase zone shrinks due to the evaporation of the organic liquid into the injected clean air, which is then removed. However, some portion of clean air bypasses the two-phase zone where the soil pores are partially occupied by the liquid contaminant and, hence, offer a higher resistance to air flow; only a portion of air actually penetrates through the two-phase zone and becomes saturated with the organic vapor. The bypassing phenomenon is also evident from the iso-concentration contours inclined toward the outlet at the top, which apparently limits the effectiveness of the remediation system. To alleviate this problem, a second SVE process is analyzed in which the production well is only half-screened from midheight to the bottom. All other conditions remain the same. The screened zone is designed to direct the injected air through the contamination zone to augment the recovery efficiency. Figure 44(d) shows that the two-phase zone indeed recedes more significantly than the first remediation system. The iso-concentration contours also demonstrate a nearly pistonlike displacement. Clearly, the two designs shown in Figs. 44(c) and 44(d) indicate the importance of a good understanding and control of the multidimensional distribution of the injected fluid in the subsurface. Herein lies the practical significance of a powerful and efficient analysis tool.

The previous simulation for all stages of infiltration, redistribution, and

remediation required approximately 3 CPU hours on a Hewlett Packard 715/75 workstation, and a total of 2700 grid blocks was used. Many fine-scale phenomena such as the island of residual NAPL (Fig. 44(d)) would not have been captured if coarser grids were used. Future research is to extend this numerical study to nonisothermal systems to allow for virtual remediation using thermal methods, thus providing a guide in designing actual field remedial systems.

C. Three-Phase Systems

The simultaneous presence of three phases such as water, gas, and an organic liquid immiscible with water in a porous medium significantly complicate transport processes. The scenarios are commonly encountered in the subsurface environment and petroleum reservoirs. Chemical components present in such systems may include water, air, and various hydrocarbons. Nonisothermal processes are of interest for thermally enhanced methods of recovering oil or contaminant. Typical thermal methods involve steam and hot water injection. In these complex multicomponent three-phase systems, a whole spectrum of transport phenomena is expected to occur and interact with one another. Examples are interphase solute partitioning, interfacial mass and heat transfer, evaporation, condensation, thermosolutal convection in the gas phase, phase migration driven by capillary forces, gravity-induced phase separation, and unstable immiscible displacement due to both density and viscosity contrasts. These complexities make numerical methods the only realistic choice in the pursuit of solutions for practical problems. For the same reason, explained in Part III, Section F, the following review excludes the petroleum engineering literature.

Very few experimental investigations on these systems existed in the open literature. Udell and coworkers [160, 161] conducted an extensive series of experiments using steam to displace various NAPLs such as xylene, diesel fuel, and perchlorolethylene (PCE). Visual observations of the contaminant front were made, and effluent concentrations of contaminants were measured as functions of the displacement time. No temperature and saturation distributions were presented, however, making it difficult to acquire a detailed understanding of the steam injection processes.

Numerical modeling of nonisothermal three-phase flow and transport in porous media was attempted only recently, and modeling issues essentially center on the treatment of phase appearance and disappearance. This issue is significant for the types of nonisothermal systems being considered, not only because it is inherent to MFM that has been used in all the

previous numerical work, but also because the practical goal of clean-up efforts is to completely remove NAPLs from the subsurface. Falta *et al.* [117] employed an integral finite difference method to discretize MFM, and proposed a variable substitution scheme that switches primary variables and governing equations whenever phase transitions occur at a location in the model domain. The variable switching criteria consist of minimum residual saturation requirements for gas and aqueous phases. Adenekan *et al.* [162] further refined the switching procedure, but did not demonstrate the performance of their improved algorithm. Forsyth [163] showed several sample calculations of steam injection in both Cartesian and axisymmetric geometries using a different technique to handle phase appearance and disappearance, which required the gas phase to always be present. Most recently, Panday *et al.* [40] categorized previous formulations and highlighted their respective advantages and disadvantages. In summary, all the previous numerical models were based on MFM and employed the procedure of switching variables and governing equations, which is inherently susceptible to poor convergence. In addition, because of intensive computational efforts associated with MFM, very coarse grids were used in numerical simulations. These grids certainly cannot capture the detailed behavior in the vicinities of moving evaporation and condensation fronts where large gradients occur over a rather short distance.

In conclusion, three-phase multicomponent systems remain largely unexplored and present very challenging numerical tasks. A robust and efficient model with three-phase multicomponent and nonisothermal capabilities is presently not available. Much more research, in particular on the fundamentals, is required to advance the development of various thermal technologies with application to environmental restoration.

D. Summary

This section has exposed a full spectrum of fascinating physical phenomena involved in multiphase flow and multicomponent transport in porous media along with several emerging applications of great importance. Both fundamental and applied research in this area has been of recent origin. Much remains to be done in years to come. Whereas general applications of MMM to multiphase flow and multicomponent transport in porous media look promising, the capabilities of MMM need to be fully demonstrated. The following areas deserve immediate attention:

- Numerical modeling of three-phase systems. This is needed to provide a routine predictive tool for a wide variety of subsurface transport problems.

- Modeling of multicomponent transport. Although the application of MMM to single-component organic liquids has been demonstrated, many groundwater pollution problems involve multicomponent organic liquids, such as gasoline. When the gas phase is contaminated by multiple organic components with differing molecular diffusivities, the density-driven gas flow may become unstable, and thus enhance the transport of contaminants. Under these circumstances, multidiffusive convection occurs as a result of local buoyancy-driven instabilities formed by the difference in diffusivity of the various components.
- Effect of heterogeneities. Heterogeneities (e.g., zones of differing permeability) will contribute to contaminant spreading in a number of fundamental ways. For example, an NAPL tends to spread out horizontally when it encounters a low-permeability layer. In addition, the vapor phase transport is diffusion-dominated in low-permeability areas.
- Thermal effects in alternative remedial technologies. Such effects include thermally enhanced soil vapor extraction and hot water or steam injection.

V. Conclusions

This review has summarized the recent development in both theoretical and experimental studies of multiphase flow, heat transfer, and multicomponent transport in porous media. The available models were carefully compared and their respective merits pointed out. In particular, the recently developed multiphase mixture model (MMM) was reviewed in detail. This model was rigorously derived from the traditional multiphase flow model (MFM) without making further approximations. The new model views the multiple phases as constituents of a mixture, and thus consists only of the conservation equations for the whole multiphase mixture. All primary variables in this model are mixture properties; therefore, complex tasks to track phase interfaces separating various subregions and handle phase appearance or disappearance are avoided. In addition, explicit relations have been established to obtain the individual phase characteristics from the mixture variables in a postprocessing fashion. Finally, the new model strongly resembles the single-phase counterpart, thus offering an attractive alternative for the theoretical analysis and numerical simulation of multiphase transport phenomena in porous media. A number of successful applications of the model have been demonstrated and an efficient numerical methodology developed. It is expected that this new model will provide a viable analysis and design tool in broad engineering fields involving multiphase flow and transport in porous media.

A large variety of fundamental topics have been covered in the present review, ranging from: (1) local thermal and chemical nonequilibrium among phases; (2) non-Darcian effects such as boundary and inertia effects; (3) 1D exact solutions for steady and transient flows; (4) onset of thermal instability in the presence of boiling; (5) interactive boiling and natural or forced convection; (6) boundary-layer multiphase flow with or without phase change; (7) dryout heat flux in porous medium systems; (8) propagation of evaporation and condensation fronts in steam injection; (9) effects of mass diffusion and heat transfer on multiphase flows; (10) thermosolutal convection in multiphase, multicomponent systems; and finally (11) effects of medium heterogeneity. There are many other fundamental issues present in multicomponent, multiphase systems that remain unexplored.

Practical applications involving multiphase flow and transport in porous media were also discussed. Particular emphasis was placed on multidisciplinary and emerging areas, such as novel capillary devices for cooling of high heat load electronics, enhancement of condensation heat transfer by the use of porous structures, environmental heat transfer, drying of porous materials, and remediation of contaminated soil and groundwater.

Future research areas have been identified in individual sections where appropriate. Overall, it can be said that a continuum approach of single-component, two-phase systems in porous media has been well established. The remaining issues lie only in the more accurate description of constitutive relationships through a proper account of microscopic phase distribution and dynamics on the pore level. This will require combined modeling and experimentation efforts. However, the studies of heat transfer in multicomponent porous media systems are only at the initial stage, and very extensive research is needed in this technologically important and fundamentally intricate subfield of heat transfer.

Nomenclature

c	specific heat
C	species concentration
Ca_{ik}	capillary coefficient, $\sum_j \lambda_j \frac{\partial p_{cjk}}{\partial s_i}$
$Cs_{\alpha k}$	solutal-capillary coefficient, $\sum_j \lambda_j \frac{\partial p_{cjk}}{\partial \sigma_{jk}} \frac{\partial \sigma_{jk}}{\partial C^\alpha}$
Ct_k	thermocapillary coefficient, $\sum_j \lambda_j \frac{\partial p_{cjk}}{\partial \sigma_{jk}} \frac{\partial \sigma_{jk}}{\partial T}$
d_p	particle diameter
D	diffusion coefficient
$D(s)$	capillary diffusion coefficient
$f(s)$	hindrance function
$\mathbf{g}$	gravitational acceleration

h	enthalpy or heat transfer coefficient
h_{fg}	latent heat of liquid–vapor phase change
$\mathbf{j}$	diffusive mass flux
$J(s)$	capillary pressure function
Ja	dimensionless subcooling
k_r	relative permeability
k_{eff}	effective thermal conductivity
K	absolute permeability
L	length
$\dot{m}$	mass flux of multiphase mixture, ρu
Nu	Nusselt number
p	pressure
Pe	Peclet number
q	heat flux
$\dot{q}$	volumetric heat generation rate
Q	dimensionless heat flux
$\dot{Q}$	dimensionless heat generation rate
Ra	Rayleigh number
s	phase saturation
Sh	dimensionless superheat
t	time
T	temperature
$\mathbf{u}$	superficial or Darcian velocity vector
u_{in}	inlet velocity
v_c	characteristic velocity
x	coordinate in horizontal direction
X	quality of steam
y	coordinate in vertical direction or molar fraction of species

GREEK SYMBOLS

α	thermal diffusivity
β	thermal expansion coefficient
γ	multiphase correction coefficient
$\Delta\rho$	density difference, $\rho_l - \rho_v$
δ	boundary layer thickness
ε	porosity
η	similarity variable
λ	relative mobility
μ	viscosity
ν	kinetic viscosity
ρ	density
σ	interfacial tension

SUBSCRIPTS

c	capillary
dry	dryout
g	gas phase
h	in vertical direction
i	phase i
in	injection
k	phase k
kj	interface between phases k and j
j	phase j
l	liquid phase
O	initial state
out	outlet
r	residual or irreducible
sat	saturated state
v	vapor phase
w	wall
α	pertinent to species α
κ	"kinetic" property
2ϕ	two-phase
∞	infinite

SUPERSCRIPTS

e	equilibrium
$-$	interfacial

References

1. Boberg, T. (1988). *Thermal Methods of Oil Recovery*. Wiley, New York.
2. Abriola, L. M. (1988). *Multiphase Flow and Transport Models for Organic Chemicals: A Review and Assessment*, EA-5976, EPRI, Palo Alto, CA.
3. Faghri, A. (1995). *Heat Pipe Science and Technology*. Taylor & Francis, Washington, DC.
4. Whitaker, S. (1977). Simultaneous heat, mass, and momentum transfer in porous media: A theory of drying. In *Advances in Heat Transfer* (J. P. Hartnett and J. F. Irvine, Jr., eds.), Vol. 13, pp. 119–203, Academic Press, New York.

4a. Vafai, K., and Whitaker, S. (1986). Simultaneous heat and mass transfer accompanied by phase change in porous insulations. *J. Heat Transfer*, **108**, 132–140.
5. Shah, Y. T. (1979). *Gas-Liquid-Solid Reactor Design*. McGraw-Hill, New York.
6. Dhir, V. K. (1994). Boiling and two-phase flow in porous media. *Annu. Rev. Heat Transfer* **5**, 303–350.
7. Witherspoon, P. A., and Pruess, K. (1988). Environmental heat transfer in porous media. In *Collected Papers in Heat Transfer*, ASME HTD-Vol. **104**, Part 3, pp. 17–23. ASME, New York.
8. Cheng, P. (1978). Heat transfer in geothermal systems. In *Advances in Heat Transfer* (J. P. Hartnett and T. F. Irvine, Jr., eds.), Vol. 14, pp. 1–105, Academic Press, New York.
9. Wooding, R. A., and Morel-Seytoux, H. J. (1976). Multiphase fluid flow through porous media. *Annu. Rev. Fluid Mech.* **8**, 233–274.
10. Morel-Seytoux, H. J. (1973). Two-phase flows in porous media. *Adv. Hydrosci.* **9**, 119–202.
11. Adler, P. M., and Brenner, H. (1988). Multiphase flow in porous media. *Annu. Rev. Fluid Mech.* **20**, 35–59.
12. De Santos, J. M., Melli, T. R., and Scriven, L. E. (1991). Mechanics of gas-liquid flow in packed-bed contactors, *Annu. Rev. Fluid Mech.* **23**, 233–260.
13. Tien, C., and Vafai, K. (1990). Convective and radiactive heat transfer in porous media. *Adv. Appl. Mech.* **27**, 225–281.
13a. Vafai, K., and Sözen, M. (1990). A comparative analysis of multiphase transport in porous media. *Annu. Rev. Heat Transfer* **3**, 145–162.
14. Kaviany, M. (1991). *Principles of Heat Transfer in Porous Media*. Springer-Verlag, Berlin.
15. Catton, I., and Chung, M. (1994). Two-phase flow in porous media with phase change: Post dryout heat transfer and steam injection. *Nucl. Eng. Des.* **151**, 185–202.
16. Wang, C. Y., and Cheng, P. (1996). A multiphase mixture model for multiphase, multicomponent transport in capillary porous media. Part I: Model development. *Int. J. Heat Mass Transfer* **39**, 3607–3618.
17. Bear, J. (1972). *Dynamics of Fluids in Porous Media*. Elsevier, New York.
18. Scheidegger, A. E. (1974). *The Physics of Flow through Porous Media*. University of Toronto Press, Toronto.
19. Saez, A. E., and Carbonell, R. G. (1985). Hydrodynamic parameters for gas–liquid cocurrent flow in packed beds. *AIChE J.* **31**, 52.
20. Hassanizadeh, S. M., and Gray, W. G. (1980). General conservation equations for multiphase systems: 3. Constitutive theory for porous media. *Adv. Water Resour.* **3**, 25–41.
21. Whitaker, S. (1986). Flow in porous media II: The governing equations for immiscible, two-phase flow. *Transp. Porous Media* **1**, 105–125.
22. Brenner, H., and Edwards, D. A. (1993). *Macrotransport Processes*. Butterworth Heinemann, Boston.
23. Plumb, O. A., and Whitaker, S. (1988). Dispersion in heterogeneous porous media 1. Local volume averaging and large-scale averaging. *Water Resour. Res.* **24**, 913–926.
24. Quintard, M., and Whitaker, S. (1988). Two-phase flow in heterogeneous porous media: The method of large-scale averaging. *Transp. Porous Media* **3**, 357–413.
25. Wang, C. Y., and Beckermann, C. (1993). Single- vs. dual-scale volume averaging for heterogeneous multiphase systems. *Int. J. Multiphase Flow* **19**, 397–407.
26. Celia, M. A., Rajaram, H., and Ferrand, L. A. (1993). A multi-scale computational model for multiphase flow in porous media. *Adv. Water Resour.* **16**, 81–92.
27. Ferrand, L. A., Milly, P. C. D., and Pinder, G. F. (1989). Experimental determination of three-fluid saturation profiles in porous media. *J. Contam. Hydrol.* **4**, 373–395.

28. Wang, S. Y., Ayral, Y. S., and Gryte, C. C. (1984). Computer assisted tomography for the observation of oil displacement in porous media. *Annu. Meet. Soc. Pet. Eng.*, Dallas, TX, Pap. SPE 11758.
29. Zeev, P., Magaritz, M., and Bendel, P. (1990). Nuclear magnetic resonance imaging of miscible fingering in porous media. *Transp. Porous Media* **12**, 107–123.
30. Montemango, C. D., and Gray, W. G. (1995). Photoluminescent volumetric imaging: A technique for the exploration of multiphase flow and transport in porous media. *Geophys. Res. Lett.* **22**, 425–428.
31. Tidwell, V. C., and Glass, R. J. (1994). X ray and visible light transmission for laboratory measurement of two-dimensional saturation fields in thin-slab systems. *Water Resour. Res.* **30**, 2873–2882.
32. Udell, K. S. (1985). Heat transfer in porous media considering phase change and capillarity—the heat pipe effect. *Int. J. Heat Mass Transfer* **28**, 485–495.
33. Lenhard, R. J., and Parker, J. C. (1987). Measurement and prediction of saturation-pressure relationships in three phase porous media systems. *J. Contam. Hydrol.* **1**, 407–424.
34. Parker, J. C., Lenhard, R. J., and Kuppusamy, T. (1987). A parametric model for constitutive properties governing multiphase flow in porous media. *Water Resour. Res.* **23**, 618–624.
35. Faust, C. R. (1985). Transport of immiscible fluids within and below the unsaturated zone: a numerical model. *Water Resour. Res.* **21**, 587–596.
36. Abriola, L. M., and Pinder, G. F. (1985). A multiphase approach to the modeling of porous media contamination by organic compounds 1. Equation development. *Water Resour. Res.* **21**, 11–18.
37. McWhorster, D. B., and Sunada, D. K. (1990). Exact integration solutions for two-phase flow. *Water Resour. Res.* **26**, 399–413.
38. Allen, M. B., III (1985). Numerical modeling of multiphase flow in porous media. *Adv. Water Resour.* **9**, 162–187.
39. Ramesh, P. S., and Torrance, K. E. (1990). Numerical algorithm for problems involving boiling and natural convection in porous materials. *Numer. Heat Transfer B* **17**, 1–24.
40. Panday, S., Forsyth, P. A., Falta, R. W., Wu, S. H., and Huyakorn, P. S. (1995). Considerations for robust compositional simulations of subsurface nonaqueous phase liquid contamination and remediation. *Water Resour. Res.* **31**, 1273–1289.
41. Milly, P. C. D. (1988). Advances in modeling of water in the unsaturated zone. In *Groundwater Flow and Quality Modeling* (E. Custodio *et al.*, eds.), pp. 489–514. D. Reidel, Boston.
42. Shekarriz, A., and Plumb, O. A. (1986). A theoretical study of film condensation using porous fins. *Am. Soc. Mech. Eng. Pap.* **86-HT-31**.
43. Majumdar, A., and Tien, C. L. (1990). Effects of surface tension on film condensation in a porous medium. *J. Heat Transfer* **112**, 751–757.
44. Wang, C. Y., Beckermann, C., and Fan, C. (1994). Numerical study of boiling and natural convection in capillary porous media using the two-phase mixture model. *Numer. Heat Transfer A* **26**, 375–398.
45. Wang, C. Y., Beckermann, C., and Fan, C. (1994). Transient natural convection and boiling in a porous layer heated from below. *Heat Transfer, Proc. Int. Heat Transfer Conf. 10th, 1994*, vol. 5, pp. 411–416.
46. Easterday, O. T., Wang, C. Y., and Cheng, P. (1995). A numerical and experimental study of two-phase flow and heat transfer in a porous formation with localized heating from below. In *ASME Heat Transfer and Flud Engineering Divisions*, HTD-Vol. **321**, pp. 723–732. ASME, New York.

46a. Wang, C. Y. (1997). A fixed-grid numerical algorithm for two-phase flow and heat transfer in porous media. *Numerical Heat Transfer B*, in press.
47. Cheng, P., and Wang, C. Y. (1996). A multiphase mixture model for multiphase, multicomponent transport in capillary porous media. Part II: Numerical simulation of the transport of organic compounds in the subsurface. *Int. J. Heat Mass Transfer* **39**, 3619–3632.
48. Wang, C. Y. (1996). Multi-dimensional modeling of steam injection into porous media. *Proc. 2nd Euro. Therm. Sci., 14th UIT Natl. Heat Transfer Conf.*, Rome, Italy.
49. Chavent, G. (1976). A new formulation of diphasic incompressible flow in porous media. *Lect. Notes Math.* **503**.
50. Yortsos, Y. C. (1987). The relationship between immiscible and miscible displacement in porous media. *AIChE J.* **33**, 1912–1915.
51. Wang, C. Y., and Beckermann, C. (1993). A two-phase mixture model of liquid-gas flow and heat transfer in porous media. Part I: Formulation. *Int. J. Heat Mass Transfer* **36**, 2747–2758.
52. Whitaker, S. (1991). Improved constraints for the principle of local thermal equilibrium. *Ind. Eng. Chem. Res.* **30**, 983–997.
53. Quintard, M., and Whitaker, S. (1993). One and two-equation models for transient diffusion processes in two-phase systems. *Adv. Heat Transfer* **23**, 369–464.
54. Powers, S. E., Abriola, L. M., and Weber, W. J., Jr. (1992). An experimental investigation of NAPL dissolution in saturated subsurface system: Steady state mass transfer rates. *Water Resour. Res.* **28**, 2691–2706.
55. Hunt, J. R., Sitar, N., and Udell, K. S. (1988). Nonaqueous phase liquid transport and cleanup. *Water Resour. Res.* **24**, 1247–1269.
56. Geller, J. T., and Hunt, J. R. (1993). Mass transfer from nonaqueous phase organic liquids in water-saturated porous media. *Water Resour. Res.* **29**, 833–845.
57. Powers, S. E., Abriola, L. M., and Weber, W. J., Jr. (1994). An experimental investigation of nonaqueous phase liquid dissolution in saturated subsurface system: Transient mass transfer rates. *Water Resour. Res.* **30**, 321–332.
58. Wilkins, M. D., Abriola, L. M., and Pennell, K. D. (1995). An experimental investigation of rate-limited nonaqueous phase liquid volatilization in unsaturated porous media: Steady state mass transfer. *Water Resour. Res.* **31**, 2159.
59. Quintard, M., and Whitaker, S. (1994). Convection, dispersion, and interfacial transport of contaminants: homogeneous porous media. *Adv. Water Resour.* **17**, 221–239.
60. Nield, D. A., and Bejan, A. (1991). *Convection in Porous Media*. Springer-Verlag, New York.
61. Koch, D. L., and Brady, J. (1986). Dispersion in fixed beds. *J. Fluid Mech.* **154**, 399–427.
62. Hsu, C. T., and Cheng, P. (1990). Thermal dispersion in a porous medium. *Int. J. Heat Mass Transfer* **33**, 1587–1597.
63. Tung, V. X., and Dhir, V. K. (1988). A hydrodynamic model for two-phase flow through porous media. *Int. J. Multiphase Flow* **14**, 46–65.
64. Grosser, K. A., Carbonell, R. G., and Sundaresan, S. (1988). The onset of pulsing in two-phase cocurrent downflow through a packed bed. *AIChE J.* **34**, 1850–1860.
65. Dankworth, D. C., Kevrekidis, I. G., and Sundaresan, S. (1990). Dynamics of pulsing flow in trickle beds. *AIChE J.* **36**, 605–621.
66. Satik, C., Parlar, M., and Yortsos, Y. C. (1991). A study of steady-state steam-water counterflow in porous media. *Int. J. Heat Mass Transfer* **34**, 1755–1772.
67. Lipinski, R. J. (1984). A coolability model for postaccident nuclear reactor debris. *Nucl. Technol.* **65**, 53–66.

68. Bau, H. H., and Torrance, K. E. (1982). Boiling in low-permeability porous media. *Int. J. Heat Mass Transfer* **25**, 45–55.
69. McGuinness, M. J. (1996). Steady-solution selection and existence in geothermal heat pipes. I. The convective case. *Int. J. Heat Mass Transfer* **39**, 259–274.
70. Chuah, Y. K., and Carey, V. P. (1985). Analysis of boiling heat transfer and two-phase flow in porous media with non-uniform porosity. *Int. J. Heat Mass Transfer* **28**, 147–154.
71. Wang, C. Y., Groll, M., and Rosler, S. (1992). Dryout heat fluxes in composite porous layers heated from below. *Proc. Int. Heat Pipe Conf., 8th* (T. Z. Ma ed.), Int. Academic Publishers, Beijing.
72. Stubos, A. K., Satik, C., and Yortsos, Y. C. (1993). Effects of capillary heterogeneity on vapor-liquid counterflow in porous media. *Int. J. Heat Mass Transfer* **36**, 967–976.
73. Tsai, T. P., and Catton, I. (1987). The effect of flow from below on dryout heat flux. *J. Heat Transfer* **109**, 491–497.
74. Sheu, J. P., Torrance, K. E., and Turcotte, D. L. (1979). On the structure of two-phase hydrothermal flows in permeabale media. *J. Geophys. Res. B* **84**, 7524–7532.
75. Schubert, G., and Straus, J. M. (1979). Steam-water counterflow in porous media. *J. Geophys. Res. B* **84**, 1621–1628.
76. Morrison, F. A. Jr. (1973). Transient multiphase multicomponent flow in porous media. *Int. J. Heat Mass Transfer* **16**, 2331–2342.
77. Doughty, C., and Pruess, K. (1990). A similarity solution for two-phase fluid and heat flow near high-level nuclear waste packages emplaced in porous media. *Int. J. Heat Mass Transfer* **33**, 1205–1222.
78. Nilson, R. H., and Romero, L. A. (1980). Self-similar condensing flows in porous media. *Int. J. Heat Mass Transfer* **23**, 1461–1470.
79. Romero, L., and Nilson, R. H. (1981). Shock-like structure of phase-change flow in porous media. *J. Fluid Mech.* **104**, 467–482.
80. Nilson, R. H., and Montoya, P. C. (1980). Experiments on transient condensing flow through a porous medium. *J. Heat Transfer* **102**, 489–494.
81. Tsuruta, T., Narazaki, K., and Masuoka, T. (1988). Transient condensing two-phase flow through an initially subcooled porous medium. *JSME Int. J. Ser. II* **31**, 81–87.
82. Sleep, B. E., and Sykes, J. F. (1993). Compositional simulation of groundwater contamination by organic compounds. 1. Model development and verification. *Water Resour. Res.* **29**, 1697–1708.
83. Ambrose, J. H., Chow, L. C., and Beam, J. E. (1991). Detailed model for transient liquid flow in heat pipe wicks. *J. Thermophys. Heat Transfer* **5**, 532–538.
84. Sondergeld, C. K., and Turcotte, D. L. (1977). An experimental study for two-phase convection in a porous medium with applications to geological problems. *J. Geophys. Res.* **82**, 2045–2053.
85. Bau, H. H., and Torrance, K. E. (1982). Thermal convection and boiling in a porous medium. *Lett. Heat Mass Transfer* **9**, 431–441.
86. Ramesh, P. S., and Torrance, K. E. (1990). Stability of boiling in porous media. *Int. J. Heat Mass Transfer* **33**, 1895–1908.
87. Ramesh, P. S., and Torrance, K. E. (1993). Boiling in a porous layer heated from below: effects of natural convection and a moving liquid/two-phase interface. *J. Fluid Mech.* **257**, 289–309.
88. Schubert, G., and Straus, J. M. (1980). Gravitational instability of water over steam in vapor-dominated geothermal systems. *J. Geophys. Res. B* **85**, 6505–6512.
89. Tewari, P. K. (1982). A study of boiling and convection in fluid-saturated porous media. M.S. Thesis, Cornell University, Ithaca, NY.

90. Sondergeld, C. K., and Turcotte, D. L. (1978). Flow visualization studies of two-phase thermal convection in a porous layer. *Pure Appl. Geophys.* **117**, 321–330.
91. Hardee, H. C., and Nilson, R. H. (1977). Natural convection in porous media with heat generation. *Nucl. Sci. Eng.* **63**, 119–132.
92. Tung, V. X., and Dhir, V. K. (1990). Finite element solution of multi-dimensional two-phase flow through porous media with arbitrary heating conditions. *Int. J. Multiphase Flow* **16**, 985–1002.
93. Chung, M., and Catton, I. (1991). Post-dryout heat transfer in a multi-dimensional porous bed. *Nucl. Eng. Des.* **128**, 289–304.
94. Stubos, A. K., and Buchlin, J.-M. (1993). Analysis and numerical simulation of the thermohydraulic behaviour of a heat dissipating debris bed during power transients. *Int. J. Heat Mass Transfer* **36**, 1391–1401.
95. Stubos, A. K., Tassopoulos, M., and Kanellopoulos, N. (1994). Aspects of transient modeling of a volumetrically heated porous bed: A combination of microscopic and macroscopic approach. *Heat Transfer, Proc. Int. Heat Transfer Conf., 10th, 1994*, Vol. 5, pp. 387–392.
96. Cioulachtjian, S., Tadrist, L., Occelli, R., Santini, R., and Pantaloni, J. (1992). Experimental analysis of heat transfer with phase change in porous media crossed by a fluid flow. *Exp. Therm. Fluid Sci.* **5**, 533–547.
97. Bodvarsson, G. S., Pruess, K., and Lippmann, M. J. (1986). Modeling of geothermal systems. *J. Pet. Technol.*, pp. 1007–1021.
98. Pruess, K. (1991). Grid orientation and capillary pressure effects in the simulation of water injection into depleted vapor zones. *Geothermics* **20**, 257–277.
99. Lai, C. H., Bodvarsson, G. S., and Truesdell, A. H. (1994). Modeling studies of heat transfer and phase distribution in two-phase geothermal reservoirs. *Geothermics* **23**, 3–20.
100. Cheng, P. (1981). Film condensation along an inclined surface in a porous medium. *Int. J. Heat Mass Transfer* **24**, 983–990.
101. Plumb, O. A. (1984). Capillary effects of film condensation in porous media. *AIAA Pap.* **84-1789**.
102. Chung, J. N., Plumb, O. A., and Lee, W. C. (1992). Condensation in a porous medium bounded by a cold vertical surface. *J. Heat Transfer* **114**, 1011–1018.
103. Nusselt, W. (1916). Die Oberflachen-Kondensation des Wasserdampfes. *VDI-Z* **60**, 541–575.
104. Schlichtling, H. (1968). *Boundary Layer Theory*, 6th ed. McGraw-Hill, New York.
105. Wang, C. Y., and Beckermann, C. (1993). A two-phase mixture model of liquid-gas flow and heat transfer in porous media. Part II: Application to pressure-driven boiling flow adjacent to a vertical heated plate. *Int. J. Heat Mass Transfer* **36**, 2759–2768.
106. Wang, C. Y., and Beckermann, C. (1995). Boundary-layer analysis of buoyancy-driven two-phase flow in capillary porous media. *J. Heat Transfer* **117**, 1082–1087.
107. White, S. M., and Tien, C. L. (1987). An experimental investigation of film condensation in porous structures. *Proc. Int. Heat Pipe Conf., 6th*, Grenoble, France.
108. Parmentier, E. M. (1979). Two-phase natural convection adjacent to a vertical heated surface in a permeable medium. *Int. J. Heat Mass Transfer* **22**, 849–855.
109. Cheng, P., and Verma, A. K. (1981). The effect of subcooled liquid on film boiling about a vertical heated surface in a porous medium. *Int. J. Heat Mass Transfer* **24**, 1151–1160.
110. Schrock, V. E., Fernandes, R. T., and Kesavan, K. (1970). Heat transfer from cylinders embedded in a liquid filled porous medium. *Heat Transfer, Proc. Int. Heat Transfer Conf., 4th, 1970*, Vol. 7, Pap. CT3.6.

111. Fukusako, S., Komoriya, T., and Seki, N. (1986). An experimental study of transition and film boiling heat transfer in liquid-saturated porous bed. *J. Heat Transfer* **108**, 117–124.
112. Tung, V. X., and Dhir, V. K. (1990). Experimental study of boiling heat transfer from a sphere embedded in a liquid-saturated porous medium. *J. Heat Transfer* **112**, 736–743.
113. Baker, P. E. (1973). Effect of pressure and rate on steam zone development in steamflooding. *SPE J.* **13**, 274–284.
114. Coats, K. H. (1976). Simulation of steamflooding with distillation and solution gas. *SPE J.* **16**, 235–247.
115. Coats, K. H. (1980). In-situ combustion model. *SPE J.* **20**, 533–554.
116. Basel, M. D. and Udell, K. S. (1989). Two-dimensional study of steam injection into porous media. In *Multiphase Transport in Porous Media—1989*, ASME HTD-217, pp. 39–46. ASME, New York.
117. Falta, R. W., Pruess, K., Javandel, I., and Witherspoon, P. A. (1992). Numerical modeling of steam injection for the removal of non-aqueous phase liquids from the subsurface; 1. Numerical formulation; 2. Code validation and application. *Water Resour. Res.* **28**, 433–465.
118. Menegus, D. K., and Udell, K. S. (1985). A study of steam injection into water saturated capillary porous media. In *Heat Transfer in Porous Media and Particulate Flows*, HTD-Vol. **46**, pp. 151–157. ASME, New York.
119. Stewart, L. D., Basel, M. D., and Udell, K. S. (1987). The effect of gravity on steam propagation in porous media. In *Heat Transfer in Porous Media and Particulate Flows*, HTD-Vol. **91**, pp. 31–42. ASME, New York.
120. Hanamura, K., and Kaviany, M. (1995). Propagation of condensation front in steam injection into dry porous media. *Int. J. Heat Mass Transfer* **38**, 1377–1386.
121. Basel, M. D., and Udell, K. S. (1991). Effect of heterogeneities on the shape of condensation fronts in porous media. In *Heat Transfer in Geophysical Media*, HTD-Vol. **172**, pp. 63–70. ASME, New York.
122. Chung, M., and Catton, I. (1993). Steam injection into a slow water flow through porous media. *J. Heat Transfer* **115**, 734–743.
123. Falta, R. W. (1990). Multiphase transport of organic chemical contaminants in the subsurface. Ph.D. Thesis, University of California at Berkeley.
124. Udell, K. S., and Fitch, J. S. (1985). Heat and mass transfer in capillary porous media considering evaporation, condensation and non-condensible gas effects. In *Heat Transfer in Porous Media and Particulate Flows*, ASME HTD-Vol. **46**, pp. 103–110. ASME, New York.
125. Yuan, Z. G., and Udell, K. S. (1993). Steam distillation of a single component hydrocarbon liquid in porous media. *Int. J. Heat Mass Transfer* **36**, 887–897.
126. Plumb, O. A. (1991). Heat Transfer during unsaturated flow in porous media. In *Convective Heat and Mass Transfer in Porous Media* (S. Kakac, B. Kikis, F. A. Kulacki, and F. Arinc, eds.), pp. 435–464. Kluwer Academic, Dordrecht, The Netherlands.
127. Plumb, O. A. (1983). Convective heat transfer from surfaces submerged in unsaturated porous media. In *ASME/JSME Thermal Engineering Joint Conference* (Y. Mori and W.-J. Yang, eds.), Vol. 2, pp. 327–332. ASME, New York.
128. Pollock, D. W. (1986). Simulation of fluid flow and energy transport processes associated with high-level radioactive waste disposal in unsaturated alluvium. *Water Resour. Res.* **22**, 765–775.
129. Chen, Y. T., and Boehm, R. F. (1995). An application of unsaturated flow and heat transfer in porous media—underground storage of high level radioactive waste. *Proc. Symp. Therm. Sci. Eng. Honor Chancellor Chang-Lin Tien*, pp. 59–65.

130. Weekman, V. W., Jr., and Myers, J. E. (1965). Heat transfer characteristics of concurrent gas-liquid flow in packed beds. *AIChE J.* **11**, 13–17.
131. Specchia, V., and Baldi, G. (1979). Heat transfer in trickle-bed reactors. *Chem. Eng. Commun.* **3**, 483–499.
132. Crine, M. (1982). Heat transfer phenomena in trickle-bed reactors. *Chem. Eng. Commun.* **19**, 99–114.
133. Krischer, O. (1963). *Die Wissenschaftlichen Groundlagen der Trockungstechnik*. Springer, Berlin.
134. Luikov, A. V. (1966). *Heat and Mass Transfer in Capillary-Porous Bodies*. Pergamon, Oxford.
135. Eckert, E. R. G., and Faghri, M. (1980). A general analysis of moisture migration caused by temperature differences in an unsaturated porous medium. *Int. J. Heat Mass Transfer* **23**, 1613–1623.
136. Plumb, O. A. (1991). Drying complex porous materials—modeling and experiments. In *Convective Heat and Mass Transfer in Porous Media* (S. Kakac, B. Kikis, F. A. Kulacki, and F. Arinc, eds.), pp. 963–984. Kluwer Academic, Dordrecht, The Netherlands.
137. Bories, S. A. (1991). Fundamentals of drying of capillary-porous bodies. In *Convective Heat and Mass Transfer in Porous Media* (S. Kakac, B. Kikis, F. A. Kulacki, and F. Arinc, eds.), pp. 391–434. Kluwer Academic, Dordrecht, The Netherlands.
138. Whitaker, S. (1980). Heat and mass transfer in granular porous media. In *Advances in Drying* (A. S. Mujumdar, ed.), Vol. 1, pp. 23–61. Hemisphere, Washington, DC.
139. Udell, K. S. (1985). An exact solution to high temperature drying of high permeability capillary porous media. *ASME 85-HT-66*. ASME, New York.
140. Rogers, J. A., and Kaviany, M. (1992). Funicular and evaporative-front regimes in convective drying of granular beds. *Int. J. Heat Mass Transfer* **35**, 469–480.
141. Perre, P., and Moyne, C. (1991). Processes related to drying: Part I. Theoretical model; Part II. Use of the same model to solve transfers both in saturated and unsaturated porous media. *Drying Technol.* **9**, 1135–1179.
142. Perre, P., Moser, M., and Martin, M. (1993). Advances in transport phenomena during convective drying with superheated steam and moist air. *Int. J. Heat Mass Transfer* **36**, 2725–2746.
143. Ouelhazi, N., Arnaud, G., and Fohr, J. P. (1992). A two-dimensional study of wood plank drying. The effect of gaseous pressure below boiling point. *Transp. Porous Media* **7**, 39–61.
144. Lee, W. C., Plumb, O. A., and Gong, L. (1992). An experimental study of heat and mass transfer during drying of packed beds. *J. Heat Transfer* **114**, 727–734.
145. Stralen, S. J. D. van (1966). The mechanism of nucleate boiling in pure liquids and in binary mixtures. *Int. J. Heat Mass Transfer* **9**, 995–1046.
146. Peterson, P. F., Hijikata, K., and Tien, C. L. (1990). Variable-conductance behavior in two-phase binary thermosyphons. *J. Thermophy. Heat Transfer* **4**, 325–331.
147. Normington, P. J. C., Mahalingam, M., and Lee, T. Y. (1992). Thermal management control without overshoot using combinations of boiling liquids. *IEEE Trans. Components, Hybrids, Manuf. Technol.* **15**, 806–814.
148. Pruzan, D. A., Torrance, K. E., and Avedisian, C. T. (1990). Two-phase flow and dryout in a screen wick saturated with a fluid mixture. *Int. J. Heat Mass Transfer* **33**, 673–681.
149. National Research Council (1994). *Alternatives for Ground Water Cleanup*. National Academy Press, Washington, DC.
150. Ho. C. K., and Udell, K. S. (1992). An experimental investigation of air venting of volatile liquid hydrocarbon mixtures from homogeneous and heterogeneous porous media. *J. Contam. Hydrol.* **11**, 291–316.

151. Forsyth, P. A., and Shao, B. Y. (1991). Numerical simulation of gas venting for NAPL site remediation. *Adv. Water Resour.* **14**, 354–367.
152. Lingineni, S., and Dhir, V. K. (1992). Modeling of soil venting processes to remediate unsaturated soils. *J. Environ. Eng. (N.Y.)* **118**, 135–152.
153. Kaluarachchi, J. J., and Islam, K. M. M. (1995). Thermal venting to recover less-volatile hydrocarbons from the unsaturated zone; 1. Theory; 2. Model applications. *J. Contam. Hydrol.* **17**, 293–331.
154. Schwille, F. (1988). *Dense Chlorinated Solvents in Porous and Fractured Media: Model Experiments*. Lewis Publishers, Ann Arbor, MI.
155. Pantanzidou, M., and Sitar, N. (1993). Emplacement of nonaqueous liquids in the vadose zone. *Water Resour. Res.* **29**, 705–722.
156. Geel, P. J. Van, and Sykes, J. F. (1994). Laboratory and model simulations of a LNAPL spill in a variably-saturated sand. 1. Laboratory experiment and image analysis techniques. *J. Contam. Hydrol.* **17**, 1–25.
157. Falta, R. W., Javandel, I., Pruess, K., and Witherspoon, P. A. (1989). Density-driven flow of gas in the unsaturated zone due to the evaporation of volatile organic compounds. *Water Resour. Res.* **25**, 2159–2169.
158. Mendoza, C. A., and Frind, E. O. (1990). Advective-dispersive transport of dense organic vapors in the unsaturated zone 2. Sensitivity analysis. *Water Resour. Res.* **26**, 388–398.
159. Wang, C. Y., Cheng, P., and Zhao, T. S. (1996). A novel approach to multiphase flow, heat and mass transfer in porous media. In press.
160. Basel, M. D. (1991). Two-dimensional propagation of steam through partially saturated porous media. Ph.D. Thesis, University of California, Berkeley.
161. Itamura, M. T., and Udell, K. S. (1993). Experimental clean-up of a dense non-aqueous phase liquid in the unsaturated zone of a porous medium using steam injection. In *Multiphase Transport in Porous Media*, ASME HTD-Vol. **265**, pp. 57–62. ASME, New York.
162. Adenekan, A. E., Patzek, T. W., and Pruess, K. (1993). Modeling of multiphase transport of multicomponent organic contaminants and heat in the subsurface: Numerical model formulation. *Water Resour. Res.* **29**, 3727–3740.
163. Forsyth, P. A. (1994). A positivity preserving method for simulation of steam injection for NAPL site remediation. *Adv. Water Resour.* **16**, 351–370.